Dissertation:

On the study of photoluminescence and photocatalytic properties of doped $BaZrO_3$

Presented by
M.S. Raúl Borja Urby

Thesis submitted in partial fulfillment of the requirements for the degree of

DOCTOR IN SCIENCES (Optics)
At Centro de Investigaciones en Óptica

Advisors:
Dr. Luis Armando Díaz Torres (CIO)
Dr. Pedro Salas Castillo (CFATA-UNAM)

León Guanajuato, México. May 2012

Estoy de acuerdo con la versión presentada de tesis, incluye los cambios propuestos por los sinodales.

Asesor de Tesis	Co-Asesor de Tesis
_____	_____
Dr Luis Armando Díaz Torres. Investigador titular (CIO)	Dr. Pedro Salas Castillo. Investigador Titular (CFATA-UNAM)

Comité de evaluación:

Dr. Luis Armando Díaz Torres (CIO) **Presidente**	_____
Dr. Isaías Hernández Pérez (UAM) **Secretario**	_____
Dr. Pedro Salas Castillo (CFATA-UNAM) **Vocal**	_____
Dr. Gabriel Ramos Ortiz (CIO) **Vocal**	_____
Dr. Haggeo Desirena Enrríquez (CIO) **Vocal**	_____

Mayo del 2012, León Gto., México.

Dedicatoria

A mi esposa: Nancy ♥

A mis padres Rafael y Gloria Elsa

A mis hermanos: Rafael, Carlos y Cesar

Indivisa Manent

Uno no es lo que es por lo que escribe, sino por lo que ha leído.
Jorge Luis Borges.
(1899-1986)

Agradecimientos

A Dios padre mi profundo y más humilde agradecimiento por tantas bendiciones en mi vida.

Si hasta ahora he logrado tanto en tan poco tiempo, es por la fortuna de tener esas bendiciones a mí alrededor, *familia, esposa, amigos, maestros y conocidos*, que me han brindado su apoyo sincero. Porque me han aceptado como soy y me han honrado con su amistad, he podido compartir con ustedes día a día lo que pienso y siento, lo que me hace feliz y lo que me indigna. Por ustedes, por su reconfortante presencia en mi vida, he logrado conquistar una etapa más, el doctorado. Afirmo que la más grande bendición ha sido conocerlos. Extiendo mi agradecimiento no solo a las personas que conocí en esta etapa que concluyo, sino a todas las que se han cruzado por mi camino, y he tenido la dicha de llamarlos, familia y amigos.

Mi especial agradecimiento es para mi guía constante durante el doctorado, mi asesor, Dr. *Luis Armando Díaz Torres*. Por darme el voto de confianza, por creer en mí y darme la libertad de trabajar, siempre bajo el resguardo y la seguridad de su experiencia. Un viejo proverbio chino indica que es mejor llorar durante el entrenamiento que hacerlo en el campo de batalla. Así mismo agradezco a mi co-asesor el Dr. *Pedro Salas Castillo*, gracias a ambos por cada una de las pláticas que sostuvimos sobre el trabajo, los resultados y la vida profesional, que me enseñaron nuevos conceptos, me aclararon lo que estaba pasando con mis experimentos y me brindaron la oportunidad de vislumbrar nuevos horizontes. Por su sincero consejo ¡Gracias!

Agradezco al *Centro de Investigaciones en Óptica* como entidad que representa a todas las buenas personas que en el laboran y lo hacen ser una institución educativa de excelencia. Su entusiasmo y amor por el centro se refleja en la calidad y en el confort que se perciben todos los días, logran que cada día de trabajo en el CIO sea especial.

Siendo la generación de conocimiento y su aplicación para el desarrollo tecnológico y la solución de problemas que aquejan a la sociedad, el motor que impulsa el progreso de un país y sus ciudadanos, agradezco al *Consejo Nacional de Ciencia y Tecnología* por concederme la beca para mis estudios de Doctorado en Ciencias, la cual siempre llegó puntual. Esperando poder retribuir con creces a mi País por dicho apoyo concedido.

Raúl Borja Urby.

Abstract

The current human lifestyle relays on the constant development of technology and scientific knowledge on a faster rate than it was on past decades, to support and solve future necessities of human societies. It exist therefore, a necessity to generate specialized human resources to work on and to develop the technological industries which will aid on the solution of current and future problems. It is through the thorough study of the properties of the materials used on industry, that more efficient used or new applications could be found for them. Such is the case of illumination and catalysis industries. Generation of efficient white-light sources and new photocatalyst materials active in the visible-light range, are now two hot trends on the materials science field. In particular, barium zirconate ($BaZrO_3$) is a ceramic material of the perovskite family which had been intensively studied in the past, now it is found in a wide variety of useful applications. The present work focused on the study and characterization of $BaZrO_3$ crystalline structure, composition, morphology, optical, luminescent and catalytic properties as a function of: 1) the ionic radii of the substituted rare earth elements (RE), 2) overall RE concentration and 3) total bismuth concentration. The first two were concerned on the generation of white-light and blue-light nanophosphors, respectively. In the case of white-light nanophosphor, RE single doping $BaZrO_3$ approach was used. Photoluminescence (PL) of each material sample was obtained after UV excitation at 267 nm site. During the hydrothermal synthesis silicon atoms were inadvertently added to the compounds from the glass autoclave. Incorporation of slight concentrations of silicon atoms into the RE single doped $BaZrO_3$ samples seems favorable to the PL properties. Dysprosium and europium doped samples had better energy distribution on the emission spectra. White and red color emissions were respectively obtained from each of these samples due to nonradiative energy transfer process from the host to the dopant. Emission spectra of dysprosium doped sample approach to a white emission according to the CIE 1931 color model. In the case of blue-light emission phosphors, it was obtained by upconversion (UC) process under NIR excitation. The color emission of ytterbium-thulium codoped $BaZrO_3$ samples strongly depended on cross relaxation processes between thulium ions. It was found that the color emission could be tuned to red or blue colors as the interaction between thulium ions in the compound increased. Catalytic activity of bismuth doped $BaZrO_3$ samples was tested by degradation of an organic dye under UV-light and visible-light irradiations. Catalytic activity under sunlight irradiation of highly bismuth doped sample was possible due to strong optical absorption up to 600 nm and narrow band gap of 2.45 eV of the highly doped sample. It was found that bismuth doped $BaZrO_3$ compounds preserved the $BaZrO_3$ cubic phase up to a 10 mol% bismuth concentration, which is critical for a well catalytic activity.

Introduction

Barium zirconate ($BaZrO_3$) is identified among a variety of metal–oxide perovskite as an outstanding material due to its ideal properties: chemical stability, single crystalline cubic phase in a wide range of temperatures (1600K – 4K), high fusion temperature around 2600 ˚C, wide band gap (~3.8 – 5.0 eV), wide optical window, low coefficient of thermal expansion and poor thermal conductivity [1,2]. Such properties place $BaZrO_3$ as a useful material in diverse applications like: crucible material used in the synthesis of superconductors, components in wireless communication systems, supersonic aircraft industry, host material for visible light generation, and lately as a green photocatalyst for water splitting [3-6]. Intensive research on this perovskite has been made to have a better understanding about the origin of these properties. For instance, the photoluminescence (PL) emission of $BaZrO_3$ at room temperature (RT) depends not only on the particle size but also on the shape and composition of the synthesized material [7]. Ordered $BaZrO_3$ structure is constituted by dodecahedral BaO_{12} and octahedral ZrO_6 sites. The origin of $BaZrO_3$ PL emission has been traced to structural disorder in the constituent polyhedrons (BaO_{12} and ZrO_6) related to oxygen vacancies (V_o), which are generated during the synthesis process. There are different methodologies to successfully synthesize barium zirconate and have a better control of crystalline phase, morphology, particle size and a better cost – benefice, which are among others: vapor phase synthesis, sol-gel, hydrothermal reaction, solid state reaction and microwave assisted hydrothermal reaction [8-11]. Variations on the crystalline structure can be achieved by proper doping of the perovskite, whether it is to change the native properties of it, or to make a new alloy [12,13]. Host materials with wide band gap (3.8–7.0 eV) are attractive for optical applications in the visible and ultraviolet (UV) spectral regions. The main reason of this attractive characteristic is that housed dopants are able to emit light within the host optical window. Recently there has been a great interest in generation of visible light sources for a variety of applications purposes. Frequency upconversion (UC) and downconversion processes are two effective options for visible light generation [14]. Being the former a process where near–infrared (NIR) photons from a light source are converted by the material into visible photons via multiphonon mechanisms, whereas in downconversion processes UV photons are converted to visible photons. Lanthanide rare earth elements are the

suitable candidates for visible light generation owing to their plentiful energy levels with narrow spectral line emissions [15]. Rare earth (RE) ions have important characteristics that distinguish them from other optically active ions which lead to excellent optical performance in many applications [16]. From their original use as phosphor in color television (early 1960's), to laser, active fiber optics, data storage devices, permanent magnets and emerging technologies such as: hybrid electric vehicles, miniaturized devices and electronics, the RE have become essential components of modern technology[16].

The lanthanide RE begin with the element cerium (Ce) which has an atomic number Z of 58, and end with the element lutetium (Lu, Z= 71). The electron configuration of the lanthanide RE follow from that of the element xenon (Xe, Z=54). While neutral lanthanum (La, Z= 57) has the electron configuration [Xe]5d6s^2, the electrons that are added to the neutral elements that follow are found in the 4f shell and only Ce, gadolinium (Gd, Z= 64) and Lu have a 5d electron. From the perspective of optical and electronic properties, the most important feature of the lanthanide REE is the lanthanide contraction [17]. This is a consequence of imperfect screening by the 4f electrons, which leads to an increase in effective nuclear charge as the atomic number increases in the lanthanide series. As a result, the 4f electrons become increasingly more tightly bound with increasing Z. In terms of their spatial extent, the 4f wave functions for element La lie outside the xenon shell, but by neodymium element (Nd, Z= 60) they have contracted so much that the maximum lies within the 5$s^2$5p^6 close shells of the xenon electron structure. In condensed matter the trivalent (3+) level of ionization is the most stable for lanthanide ions and most optical devices use trivalent ions. Ionization preferentially removes the 6s and 5d electrons, and the electronic configuration for these ions (RE ions) is that of the xenon structure plus a certain number (1-14) of 4f electrons. The observed infrared (IR) and visible optical spectra of trivalent rare earth ions is a consequence of transitions between 4f states. The effect of lanthanide contraction has important implications, because the 5s and 5p electrons shield the 4f electrons from the effects of the environment. The consequences for the static interactions are energy levels that are relatively insensitive to host, have small host-induced splitting and are only weakly mixed with higher energy states. The dynamic consequences are little or no vibronic structure (phonon-assisted transitions) and weak nonradiative relaxation of excited states, which occurs through phonon emission. The net result are optical transitions between 4f states that manifest themselves as sharp lines, and emission that can be highly efficient.

After doping $BaZrO_3$ with trivalent RE ions the crystalline structure and optical properties of the host changes, depending on the RE ion and doping concentrations [11]. PL measurements are commonly used to evaluate the structural properties of the site where the dopant is substituted inside the host crystalline structure [17,18]. PL intensity emissions of $BaZrO_3$ have been directly related to the order–disorder (od) degree of the crystalline structure. Zirconium clusters (ZrO_6/ZrO_5) are formed after dopant introduction generates V_o allowing intermediate energy levels inside the band gap which narrows it and increases the disorder degree of the compound [19]. Being visible light generation of relative interest in the field of nanomaterials, and given the ideal properties of perovskite $BaZrO_3$, a study on the dependency of $BaZrO_3$ intrinsic emission on the increasing ionic radii of the substituted RE ion (Yb^{3+}, Er^{3+}, Dy^{3+}, Eu^{3+} and Ce^{3+}) is addressed as part of this work by RE single doping and downconversion mechanism. As for white light generation, it is of particular interest to find a material that renders blue light, as this has proved to be the most elusive emission needed to generate white light by addition of the three primary colors: red, green and blue. With such motivation to develop a new blue phosphor, many investigations have been done on Tm^{3+} activated oxides, because Tm^{3+} can provide blue luminescence and can be doped at high concentration [20-22]. In the present work, this problem is approached by co-doping $BaZrO_3$ with Yb^{3+}–Tm^{3+}, to generate visible light via upconversion mechanism, and using Yb^{3+} ions as sensitizer of near infrared excitation.

A material which speed up a chemical reaction and induce change without itself being changed or consumed in the process is called a catalyst. A catalyst is able to provide selectivity or specificity to particular products which are more desirable than others [23]. Catalysis is the research field that studies the properties of the catalyst materials, and occupies a pivotal position in the physical sciences and the chemical industries. It is essential for chemical and materials manufacturing, fuel cells technology, energy conversion systems, combustion devices, and pollution control systems, among many others. In the last 40 years, catalysis under light irradiation, called photocatalysis, has become an important research field, since A. Fujishima and K. Honda achieved ultraviolet light-induced water cleavage [24]. This opened up the possibility of solar energy conversion by semiconductor materials [25]. In recent years, semiconductor photocatalytic process has shown a great potential as a low-cost, environmental friendly and sustainable treatment technology to align with the “zero” waste scheme in the water/wastewater

industry. The ability of this advanced oxidation technology has been widely demonstrated to remove persistent organic compounds and microorganisms in water. At present, the main technical barriers that impede its commercialization remained on the post-recovery of the catalyst particles after water treatment [26].

The basic principle of the semiconductor photocatalytic reaction involves light irradiation of energy greater than the band gap, which excites an electron in the valance band into the conduction band to result in the formation of an excited electron (e^-) – hole (h^+) pair. These e^- and h^+ reduce and oxidize respectively the chemical species in contact with the surface of the photocatalyst, unless they recombine to give no net chemical reaction but heat. Basically, the photocatalytic activity of semiconductor materials is controlled by three parameters: 1) light absorption property, 2) rate of reduction and oxidation by the photogenerated e^- and h^+ pairs and 3) recombination rate of the e^- and h^+ pairs. Particle size and surface texture are directly related to the first parameter. In the case where a powder suspension (heterogeneous catalysis) is used, almost all the photons are absorbed by the particles. In the photocatalytic reaction systems only the surface of the catalyst can absorb incident photons and contribute to the reaction. The redox potential on the surface of the photocatalyst depends directly on its specific surface area which interacts with the chemical species, thus, the larger the specific surface area the higher the photocatalytic activity [27].

Recent studies on UV–active photocatalysis used for the first time $BaZrO_3$ for water splitting, concluded that production of O_2 and H_2 gasses were due to ideal cubic crystalline phase with bond angle of 180˚ of the ZrO_6 octahedral sites, largely dispersed conduction band dominated by zirconium 4*d* orbitals, and highly negative potential photoinduced electrons. This work proved the novel photocatalytic property of pure $BaZrO_3$ under UV irradiation [6]. The angle between metal–oxygen–metal (M–O–M) bonds in perovskite semiconductor is a relevant structural parameter to be taken into account. In perovskite systems like $ATaO_3$ (A = Li, Na and K), $Sr_2Nb_2O_7$ and $Sr_2Ta_2O_7$ [28-30] it was found that as the M–O–M bond angle approximates to 180˚ the easier the excitation energy is delocalized. The increasing necessity of stable and durable visible light active photocatalyst (*green photocatalyst*) has been the motivation of many investigations in order to develop new materials with a more efficient use of natural sunlight [31-33]. In 2007 Tang *et al*., succeeded on synthesize by a soft chemical method a well crystallized

monoclinic $BaBiO_3$ perovskite with a 2.05 eV band gap. Such a narrow band gap allows this material to strongly absorb visible light around 500 nm. Efficient decomposition of organic dye by $BaBiO_3$ under visible light ($\lambda < 650$ nm) irradiation was related to high contribution of bismuth 6*s* orbitals into the valance and conduction bands, favoring the mobility of photocarriers through the material to the surface [34]. In 2010 photocatalytic property of β-Bi_2O_3 under visible light irradiation was studied by Wang *et al*. Despites the strong visible light ($\lambda < 500$ nm) absorption of pure β-Bi_2O_3 and band gap of 2.1 eV, β-Bi_2O_3 photocatalytic activity is rather limited by its structural instability during the catalytic reaction. Phase stabilization of β-Bi_2O_3 at room temperature was achieved by doping it with titanium ions. The results showed Ti^{4+} doped β-Bi_2O_3 stabilized during the photocatalytic degradation of dye molecules under visible light irradiation, and phase transition was prevented due to Ti^{4+} ions introduction. Wang *et al.,* suggest that rare earths or transition metals could be used to phase stabilization of other materials in order to improve their photocatalytic properties [35]. In 2010 Yupeng Yuan *et al.,* incorporated Sn^{4+} in $BaZrO_3$ perovskite and proved that after Sn^{4+} substitution into ZrO_6 octahedral sites, the band gap of $BaZrO_3$ narrowed down as a consequence of the increased electronegativity of Sn^{4+} over Zr^{4+} ions. The strong contributions of tin 5*s* orbitals to $BaZrO_3$ conduction band modified the electronic structure of $BaZrO_3$, and shifted the band gap from an indirect to a direct band gap semiconductor, which was the reason of the notable impact of Sn^{4+} in $BaZrO_3$ UV-active photocatalytic properties [36]. Despites the efforts made to develop effective green photocatalysts, the activities for organic decomposition at wavelength longer than 500 nm are not yet sufficient. Which make development of visible light active photocatalytic materials still a problem to be solved for the practical applications [34]. In the search for alternative green photocatalysts we propose in this work to dope $BaZrO_3$ with Bi^{3+} ions in order to develop a potentially and viable new property for this material: visible light active photocatalyst. By means of hydrothermal reaction, it is expected that a material composed of $BaZrO_3$ and Bi_2O_3 could be achieved as a solid solution, and take advantage of the intrinsic properties of both cubic perovskite $BaZrO_3$ and visible light active Bi^{3+} ions. To reduce the optical band gap of the compound while retaining the ideal properties of $BaZrO_3$ after bismuth introduction is the principal objective. In order to accomplish this, precautions should be taken as it is well known that metal oxide perovskite properties depend strongly on the synthesis parameters, which have a direct impact on the final structural, morphological and optical properties. A good crystallized,

single phase, under 100 nm size, monodisperse and homogeneous morphology compound is ideal for a semiconductor material in order to be an efficient and chemically stable photocatalyst. Recently, it has been possible for our research group to synthesized through hydrothermal methodology pure, crystalline, single phase $BaZrO_3$ of submicron regular particles, it was learn how reaction time, surfactant, solvent water to ethanol ratio and coprecipitation agent affect the structural, morphological and optical properties of $BaZrO_3$ [37].

In the present thesis report a study of the intrinsic PL emission of $BaZrO_3$ as a function of the ionic radii of substituted RE ions is performed to elucidate if such substitution allows the manipulation and enhancement of such intrinsic emission. This was addressed in two different directions: **1)** rare earth single doping (Ce^{3+}, Eu^{3+}, Dy^{3+}, Er^{3+} and Yb^{3+}) under UV light excitation, and **2)** by co-doping with Yb^{3+} and Tm^{3+} under NIR light excitation. Also in this thesis Bi^{3+} dope $BaZrO_3$ was synthesized with different bismuth concentrations via the hydrothermal process. A structural, photoluminescence and photocatalytic study of $BaZrO_3$: Bi^{3+} was performed. Final results of the conducted studies showed: **1)** enhancement of the intrinsic emission of $BaZrO_3$ as a result of emissions superposition, and a better energy distribution to approach white light generation, **2)** overall dopant concentration in codoped $BaZrO_3$ controlled the blue or red emission obtained under NIR excitation, being the cross relaxation process the cause of emission color change, and **3)** a new application of $BaZrO_3$ is exposed when it was used to degrade organic dye under UV light inside the lab and under natural sunlight outdoors.

The thesis report is organized in four sections corresponding to: chapter 1 *On the synthesis methodology and characterization techniques,* chapter 2 *Characteization of $BaZrO_3$ when doped and co-doped with rare earth,* chapter 3 *$BaZrO_3$ as a photocatalyst* and chapter 4 *summary and future work*.

References

1. *On the development of high density barium metazirconate (BaZrO3) ceramics.* Abdul-Majeed, Azad, Selvarajan, Subramaniam and Teng Wang, Dung. 2002, Journal of Alloys and Compounds, Vol. 334, pp. 118-130.
2. *A New Blue, Green and Red Upconversion Emission Nanophosphor: BaZrOEr,Yb.* Diaz-Torres, L.A., et al. 2008, J. Nanosci. Nanotechnol., Vol. 8, pp. 6425-6430.
3. *BaZrO3: the solution for the crucible corrosion problem during the single crystal growth of high Tc superconductors.* Erb, A., Walker, E. and Flükiger, R. 3-4, 1995, Physica C: superconductivity, Vol. 245, pp. 245-251.
4. *ac conductivity studies on the electron irradiated BaZrO3 ceramic.* Jali, V. M., et al. 2007, J. NIM B, Vol. 257, pp. 505-509.
5. *Photoluminescence properties of SrZrO3Eu3+ and BaZrO3Eu3+ phosphors with perovskite structure.* Huang, Junli, et al. 2009, J. Alloy Compd. DOI: 10.1016/j.jallcom.2009.07.153.
6. *Synthesis and photocatalytic characterization of a new photocatalyst BaZrO3.* Yuan, Yupeng, et al. 2008, Int. Hydrogen Energy, Vol. 33, pp. 5491-5946.
7. *Synthesis of Fine Micro-sized BaZrO3 Powders Based on a Decaoctahedron Shape.* Moreira, Mario L., et al. 2, 2009, Crystal Growth & Design, Vol. 9, pp. 833-839.
8. *On nanoparticle aggregation during vapor phases sybthesis.* Singhal, A., et al. 4, 1999, NanoStruct. Mater. , Vol. 11, pp. 545-552.
9. *Synthesis and luminescence of YlnGeO phosphors activated by dysprosium ions.* Zhang, Hongwu, et al. 2008, J. Alloys Compd., Vol. 459, pp. 103-106.
10. *Hydrothermal synthesis and in situ surface modification of boehmite nanoparticles in supercritical water.* Mousavand, T., et al. 2007, J. Sup. Flu., Vol. 40, pp. 397-401.
11. *Preparation and luminescence properties of BaZrO3 Eu phosphor powders.* Liu, Xiaohua and Wang, Xiaodong. 2007, Opt. Mater., Vol. 30, pp. 626-629.
12. *Preparation and dielectric properties of Dy, Er doped BaZrTiO3 ceramics.* Su-E, Hao, Liang, Sun and Jin-Xiang, Huang. 2008, Mater. Chem. and Phys, Vol. 109, pp. 45-49.
13. *Photoluminescence property of Ba(ZrTi)O3 powders prepared by solid state reaction and polymeric precursor method.* Rout, S. K., et al. 2009, Physica B, Vol. 404, pp. 3341-3347.
14. *Visible light emission under UV and IR excitation of rare earth doped ZrO2 nanophosphor.* De la Rosa, E., et al. 2005, Opt. Mat., Vol. 27, pp. 1320-1325.
15. *Crystal field splitting of lanthanide 4f 5d-levels in inorganic compounds.* Dorenbos, P. 2002, J. Allo. Compd., Vol. 341, pp. 156-159.
16. *Rare earths crucial elements of advanced technologies.* Henderson, N. 2, s.l. : Aldrich chemical Co., 2011, Material Matters, Vol. 6.
17. *Shape control and spectroscopy of crystalline BaZrO3 perovskite particles.* Zhou, Hongjun, Mao, Yuanbing and Wong, Stanislaus S. 2007, J. Mater. Chem. DOI: 10.1039/b616522b.
18. *Synthesis and photoluminescence properties of Eu doped AZrO3 _A Ca Sr Ba perovskite.* Zhang, Hongwu, et al. 2007, J. Alloys Compd. DOI: 10.1016/j.allcom.2007.04.259.
19. *Intense violet-blue photoluminescence in BaZrO3 powders A theoretical and experimental investigation of structural order-disorder.* Cavalcante, L.S., et al. 2008, Optics Comunications, Vol. 281, pp. 3715-3720.
20. *Blue luminescence of nanocrystalline CaZrO3Tm phosphors synthesized by a modified Pechini sol–gel method.* Zhang, Hongwu, et al. 2008, Vol. 128, pp. 1348-1352.
21. *Blue emission of ZrO2Tm nanocrystals with different crystal structure under UV excitation.* Zhang, Hongwu, et al. 2008, J. Noncry. Sol, Vol. 354, pp. 15559-1563.
22. *Multicolor upconversion and color tunability in Tm3 Ho3 Yb3 doped opaque aluminum tellurite ceramics.* Sun, L. X., et al. 2009, J. Appl. Phys, Vol. 105, p. 106109.
23. Armor, John. *The North American Catalysis Society (NACS).* [Online] [Cited: 1 18, 2012.] http://www.nacatsoc.org/what.asp.
24. *Electrochemical photolysis of water at a semiconductore electrode.* Fujishima, A. and Honda, K. 1972, Nature, Vol. 238, pp. 37-38.
25. Kaneko, M. and Okura, I. Introduction. *Photocatalysis Science and Technology.* s.l. : Springer, 2002, 1, p. 356.
26. *Recent developments in photocatalytic water treatment technology: A review.* Chong, Meng Nan, et al. 2010, Water Research, Vol. 44, pp. 2997-3027.

27. Kaneko, M. and Okura, I. Design, preparation and characterization of highly active metal oxide photocatalysts. *Photocatalysis Science and Technology.* s.l. : Springer, 2002, 3, p. 356.
28. *Luminescence of alkali tantalates and niobates.* Wiegel, M., et al. 1994, J. Phys. Chem. Solids, Vol. 55, pp. 773-778.
29. *Water splitting into H2 and O2 on new Sr2M2O7 (M = Nb and Ta) photocatalyst.* Kudo, A., Kato, H. and Nakagawa, S. 2000, J. Phys. Chem. B, Vol. 104, pp. 571-575.
30. *High surface area BaZrO3 photocatalyst prepared by base hot water treatment.* Pastromo, Niki, et al. 14, 2011, J. ECERS, Vol. 31, pp. 2699-2705.
31. *Role of valency ordering on the visible light photocatalytic avtivity of BaBi3+Bi5+O3.* Lakshminarasimhan, Narayanan, Park, Yiseul and Choi, Wonyong. 2008, Chem. Physics Lett., Vol. 452, pp. 264-268.
32. *N-doped TiO2 nanoparticle based visible light photocatalyst by modified peroxide sol-gel method.* Jagadale, Tushar C., et al. 2008, J. Phys. Chem. C, Vol. 112, pp. 14595-14602.
33. *Photocatalytic properties of nanosized Bi2WO6 catalysts synthesis via a hydrothermal process.* Fu, Hongbo, et al. 2006, App. Catalysis, Vol. 66, pp. 100-110.
34. *Efficient Photocatalysis on BaBiO3 Driven by Visible Light.* Tang, Junwang, Zou, Zhigang and Ye, Jinhua. 2007, J. Phys. Chem. C, Vol. 111, pp. 12779-12785.
35. *Improved structural stability of titanium doped Bi2O3 during visible hight activated photocatalityc processes.* Wang, Yan, Wen, Yanyuan and Ding, Hanming. 2010, J. Mater. Sci., Vol. 45, pp. 1385-1392.
36. *Polymerizable complex synthesis of BaZr-SnO3 photocatalysts:.* Yuan, Yupeng, et al. 2010, J. Matter. Chem, Vol. 20, pp. 6772-6779.
37. *Hydrothermal syntesis and photoluminescence characterization of nanocrystalline BaZrO3.* Diaz-Torres, L. A., et al. 2010, Nanotechnology 2010, Vol. 1, pp. 360-363.

Contents

List of Figures

List of Tables

Chapter 1

On the synthesis methodology and characterization techniques

On the present chapter a description of the hydrothermal synthesis methodology followed to generate the studied materials is presented [1-3]. Also included in this chapter is a brief description of the typical characterization techniques: X-ray diffraction (XRD) analyses, optical absorption, optical band gap, photoluminescence (PL) spectra and electron microscopy (SEM and TEM), used to study the structural, optical and morphological properties of the studied compounds. Characterization of pure crystalline $BaZrO_3$ [4] will be used in order to get familiar with $BaZrO_3$ intrinsic properties as well as with the interpretation of the characterization results.

1.1. Hydrothermal synthesis of barium zirconate ($BaZrO_3$)

The hydrothermal synthesis methodology followed to synthesize pure and doped $BaZrO_3$ compounds at room temperature (RT) is depicted as a flow diagram in **Fig. 1** Analytical grade raw materials from Sigma-Aldrich® are used as received to elaborate all the compounds. Starting materials for pure $BaZrO_3$ (the host) are barium nitrate, $Ba(NO_3)_2$, and zirconyl chloride octahydrate, $ZrOCl_2$-$8{\cdot}H_2O$ both with a purity of 99%. Previous to initiate the synthesis process, all reagent materials are carefully weighed to calculated values of mass (g) in order to achieve stoichiometric products. In a typical procedure, the starting materials are dissolved in 100 ml distilled water solution in a lab Pyrex glass applying strong stirring for 30 min. When the material to synthesize is to be doped with rare earth (RE) or bismuth ions, the dopant precursor are dissolved previous to the host precursors in the distilled water solution. Once the starting materials are dissolved, the dispersant agent Cetyl-trimethyl-ammonium-bromide (CTAB) with a purity of 98% is introduced to the solution to reduce particle adhesion. At this point, the solvent solution is complemented with 100 ml of ethanol (96˚) to dissolve CTAB properly, and continue to stir for 30 min more. Sodium hydroxide (NaOH) with a purity of 99.9% is used as precipitant agent at 0.5 M concentration. Subsequent constant stirring for 1 h is applied to dissolve NaOH followed by 20 min in sonic wash at 30 ˚C to separate agglomerated masses to obtain a homogeneous solution. For the hydrothermal reaction to take place, the solution is transfered into a glass autoclave and placed in a furnace at 100 ˚C in air atmosphere and under autogenous pressure for 24 h (reaction time). After this, the autoclave is allowed to naturally cool down to RT. The product of the synthesis is found precipitated at the bottom of the autoclave, it is recovered and washed with ethanol four times to remove CTAB and no reacted residues. After each wash cycle, the solution is centrifuged at 3400 RPM. The washed product is dried overnight at 100 ˚C in an oven. Once it is dry, the solid product is grounded into a fine white powder

($BaZrO_3$) in an Agate mortar. Half of the powder is retained at this point for future characterization, and the other half is annealed in a furnace at 1000 ˚C for 3 h in air atmosphere to remove organic materials and occluded water to improve the crystalline structure of the material. After the annealing treatment, the autoclave is allowed to naturally cool down to RT. The annealing route is shown in **Fig. 1 b)**. Finally, the annealed compound is ground to fine powder once more for future characterization.

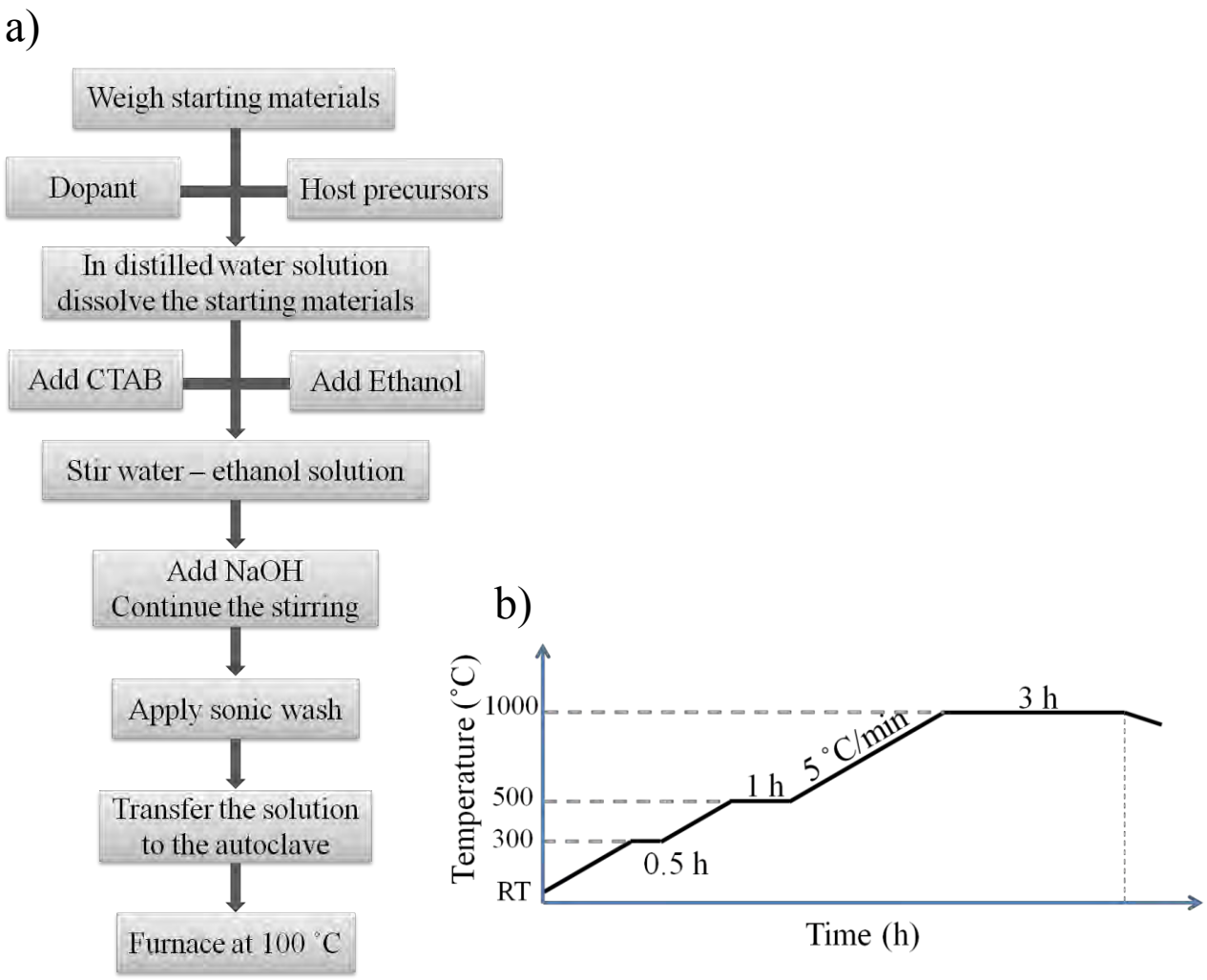

Fig. 1 a) Hydrothermal synthesis methodology followed to synthesized $BaZrO_3$ compounds in the present study, b) annealing route used in the annealing treatment of $BaZrO_3$ samples.

Different characterization techniques such as XRD, SEM and TEM spectroscopy, required for the sample under analysis to be in a fine powder presentation, whereas for optical absorption and PL characterization, pellet presentation is better for quantitative characterization. In regard of the pelletizing process, it was observed the pellet structural rigidity depended on factors such as the composition of the material and if the sample was doped (RE, bismuth or none). During the pelletizing process it was observed that such variables directly modify the hardness and dryness of the final powder, making the pelletizing process easier for the softer and driest powders. Pellets of most of the samples could be done by means of a hydraulic press and a stainless steel circular dice of 0.79 cm^2 pressure area. Adjustment to the applied force and time under constant pressure were varied until the adequate parameters to achieve a fine pellet were found in a probe and error trial. Once these parameters were known, then all the samples of the set were pelletized under the same conditions. Nevertheless, no further studies were done on the relationship of the pelletizing parameters and the material composition. Typical parameters for pellets of 1 cm in diameter and 1 mg of powder were: 5 Ton, 20 min.

In the consecutive sections the techniques used in this work to characterize the compounds structurally, morphologically and optically are described.

1.2 Characterization techniques.

1.2.1 X-ray diffraction (XRD) patterns.

The XRD patterns of a given material consist of the intensity of the light diffracted by the lattice of the material as a function of the angle 2θ, resulting in a plot of narrow peaks with different intensities, see **Fig. 2**. It is through the crystalline structure characterization of the material that the compound as well as its phase can be identified. In order to do it well, full match of the diffraction peaks with the respective standard card from the *Joint Committee on Powder Diffraction Standards* (JCPDS) is needed. In particular, perovskite $BaZrO_3$ cubic phase is identified in the JCPDS standard card: 06-0399, the main diffraction peak is found at 30.116˚ which belongs to the chrystallographic plane (110). The XRD patterns of the characterized $BaZrO_3$ samples were measured within the range [20^0, 110^0] with a 2θ step of 0.01946^0 and a counting time of 53 s per point, in a θ-θ Bruker D-8 Advance diffractometer having the Bragg-Brentano geometry, Cu Kα radiation, a Ni 0.5% Cu-Kβ filter in the secondary beam and a one-dimensional position sensitive silicon strip detector (Bruker, Lynxeye).

It is not uncommon that during the development of the synthesis methodology, phase segregation of byproducts appear in the compounds, although in our case phase segregation of byproducts were seldom found in the final products, except for the cases were the dopant were heavily loaded, the most common compounds found can be identified by means of the JCPDS standard cards: 37-148 and 45-1471 as monoclinic zirconium dioxide (ZrO_2) and orthorhombic

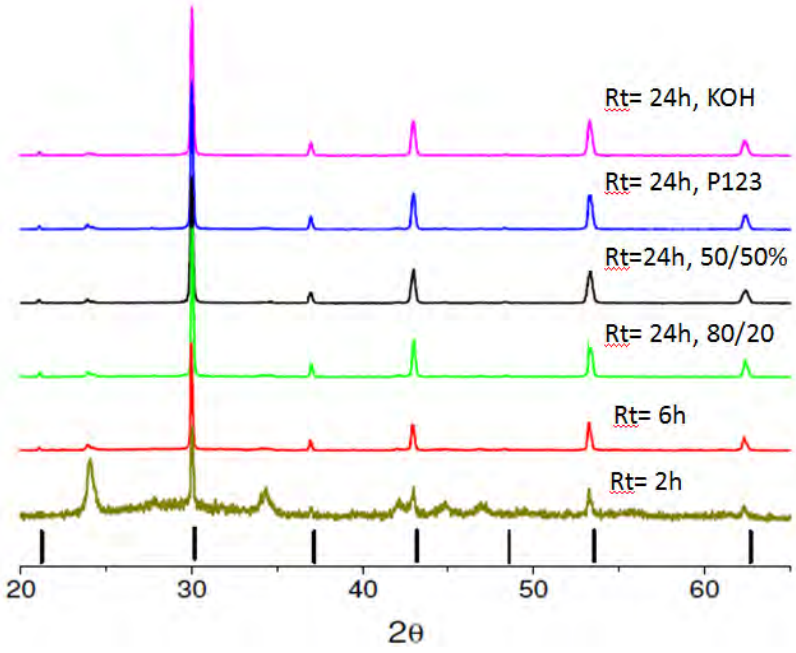

Fig. 2 Cubic phase $BaZrO_3$ materials identified via their XRD patterns. Samples of $BaZrO_3$ differ in reaction time (Rt = 2, 6, 24 h), water – ethanol solvent ratio (SR) and dispersant agent (P123, KOH) (1). JPDC standard: 06-0399 is represented at the bottom to aid in the identification of the compounds [4].

barium carbonate ($BaCO_3$) respectively.

Crystalline structure evolution of pure $BaZrO_3$ as a function of reaction time (2, 6 and 24 h) at 100 ˚C is shown in the XRD patterns on **Fig. 2** [4]. In this figure, the products of the hydrothermal processes were identified as cubic phase of $BaZrO_3$, after all of the diffraction peaks were indexed with the JCDPS standard card 06-0399, which is represented as solid dash lines at the bottom of the figure. Intense and narrow diffraction peaks on the XRD patterns evidence materials with crystalline structure. It was found that well crystallized cubic $BaZrO_3$ can be synthesized with reaction times (RT) equal or larger than 6 h. Moreover, substitution of the dispersant agent (CTAB or Pluronic 123), neither change of the precipitant agent (NaOH or KOH) nor variations on the solvent ratio (SR) seem to have an effect on the crystallization of the final compound [4]. On the other hand, when the crystalline structure of a compound cannot be identify by means of its XRD pattern due to the absence of intense and well defined diffraction peaks, it is said that the crystalline structure is no yet defined and the compound have an amorphous structure. Also, for compounds with more than one phase on its XRD pattern, it is said that it presents phase segregation, as can be seen in the XRD pattern of the compound with a RT of 2 h shown on **Fig. 2**, where the monoclinic ZrO_2 and the cubic $BaZrO_3$ phases can be identified among the amorphous structure of the compound.

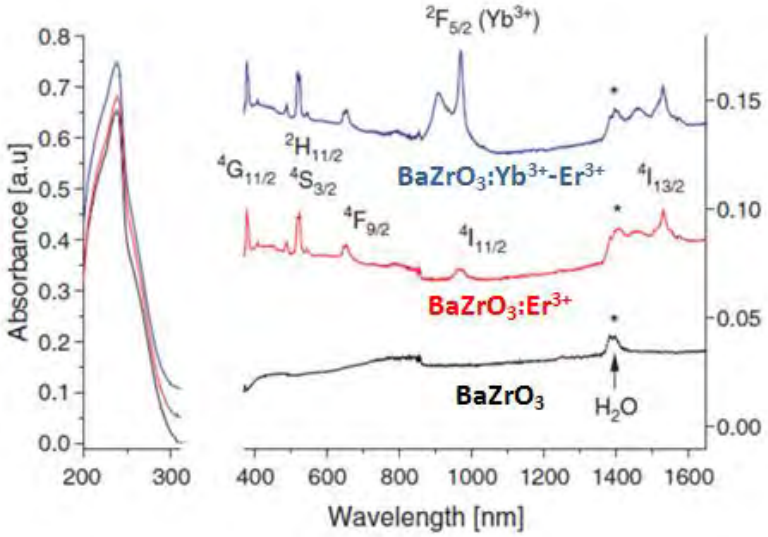

Fig. 3 Absorption spectra of undoped $BaZrO_3$, Er^{3+} doped $BaZrO_3$ and Yb^{3+}-Er^{3+} codoped $BaZrO_3$ samples [5].

1.2.2 Optical absorption.

The optical absorption spectra of all samples were recorded in the range [200nm, 2000 nm] from the ultra-violet (UV) to the visible and near infrared (NIR) regions, with a *Perkin-Elmer UV-VIS-NIR Lambda 900* spectrophotometer in diffuse reflectance mode using a 1.5 in integrating sphere (Labsphere Co.). In the absorption process, a photon excites an electron from a lower to a higher energy state which is called an absorption edge. From the resulted absorption spectra two relevant characteristics are commonly observed, **1)** the absorption edge of the pure material (the host) and **2)** possible absorption bands belonging to dopant ions, impurity traces and occluded water which reveals their existence inside the host structure. From the absorption edge is important to notice if it is displaced from its location after doping the host with different ions, since this could be related to variations on the energy gap between bands, valance and conduction. Increment or decrement of the energy gap (E_g) of a given compound is a relevant feature since it is an indicator of how the material will react to light irradiation, whether it is UV, visible or infrared light. In regard of pure and crystalline $BaZrO_3$ it is known from several absorption spectra, as the one shown in **Fig. 3** [5], that it is a transparent material since for any practical matter no light is absorbed by it within the range from 1650 down to 300 nm, this is also known as a transparency window. The characteristic absorption edge of $BaZrO_3$ is located at wavelength shorter than 300 nm (see **Fig. 3**) and the main peak in the UV region anywhere around 240 nm corresponds to the material band gap which in the case of reference [5] turns out to be 5.18 eV.

Also shown in **Fig. 3** are the absorption spectra of Yb^{3+}-Er^{3+} codoped $BaZrO_3$ and Er^{3+} doped $BaZrO_3$ samples, where it is possible to see some absorption bands belonging to Yb^{3+} (1000 nm) and Er^{3+} (1430 nm, 950nm, 645 nm, 540nm, 520nm, and 380 nm) transitions, along with the absorption band at 1382 nm which is related to residual water. These bands confirms the existence of Yb^{3+} and Er^{3+} ions along with occluded water housed in the crystalline structure of the host ($BaZrO_3$), respectively.

1.2.3 Optical band gap.

The optical band gap of a semiconductor material is determined by the energy difference between the valance band (VB) and the conduction band (CB), commonly in eV units. There are two types of optical transition than can occur from the VB to the CB of crystalline semiconductors: direct and indirect transitions. Both involve the interaction of a photon with an electron in the highest orbital of the VB, which is raised across the fundamental gap to the lowest unoccupied orbital in the CB. Indirect transitions also involve simultaneous interaction with lattice vibrations, which makes indirect transition semiconductors highly dependent on temperature [6]. In general, optical band gap depends on the crystalline structure and on the stoichiometry of the material.

In materials of direct transition and simple parabolic bands, the absorption coefficient α can be related to the optical band gap energy (E_g) through the expression:

$$\alpha n_0 h\nu \approx C(h\nu - E_g)^r \qquad \textbf{(Eq.1)}$$

where r is a constant which can take values of 1/2 or 3/2 for direct allowed or direct forbidden transitions respectively, n_o is the refractive index which is assumed to be constant over the energy variation, hν is the photon energy and C a constant. Since the absorbance γ is given by α*d, where d is the sample thickness, the above expression becomes:

$$\left(\frac{\gamma n_0 h\nu}{Cd}\right)^{1/r} = h\nu - E_g \qquad \textbf{(Eq.2)}$$

According to Wood and Tauc studies [7], estimation of the optical band gap energy (E_g) of a crystalline material can be done by a graphical method on a plot of $(\alpha h\nu)^2$ as a function of hν (photon energy), where the optical band gap energy (E_g) is obtained by extrapolation of the linear portion (absorption edge) till interception with the hν axis for $(\alpha h\nu)^{1/r} = 0$. An example is shown in **Fig. 4** [8], where the optical absorbance of a $BaZrO_3$ sample has been modified into a Wood

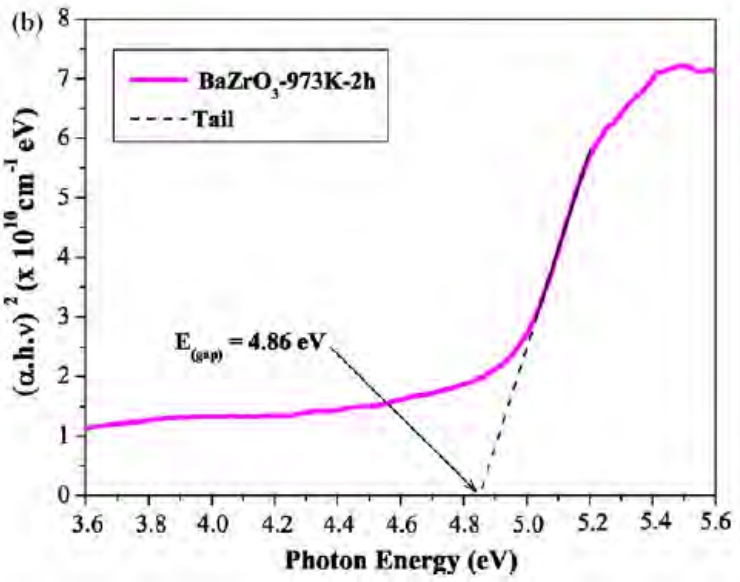

Fig. 4 Wood and Tauc plot use to estimate the optical band gap energy of crystalline semiconductors [8].

and Tauc plot, to prove that in this case pure and crystalline $BaZrO_3$ had strong absorption of light in the high energy range around 4.86 eV (256 nm). Such technique is frequently used [9] to estimate the optical band gap energy of a given semiconductor by extrapolation of the linear portion of the curve to the photon energy axis, the difference between the valance and conduction bands is found were the extension of the linear part interjects the photon energy axis.

1.2.4 Ordered-disordered structure.

Pure and crystalline $BaZrO_3$ is conformed of 2 different polyhedrons based on barium and zirconium atoms. The polyhedrons are formed of barium twelve-coordinated and zirconium six-coordinated atoms known as cuboctahedral (BaO_{12}) and octahedral (ZrO_6) sites respectively, which result of metal-oxygen (M-O) ionic bonding, see **Fig. 5 a)** [10] . When all the atoms within a polyhedron are bond to their immediate surrounding neighbors, it is said the crystalline structure is completely ordered as all of the electrons are occupied; otherwise, the crystalline structure is disordered, and unbound electrons generate oxygen vacancies (V_o), local disorder in the polyhedron site. Taking for instance the ZrO_6 octahedral site, the simplest way to visualize a disordered structure would be by displacement of one zirconium atom inducing a M-O bond breaking, resulting in a five-coordinated zirconium cluster (ZrO_5) forming a square-base pyramid, see **Fig. 5 b)** [8]. Thus, both the absorption edge and the optical band gap energy are

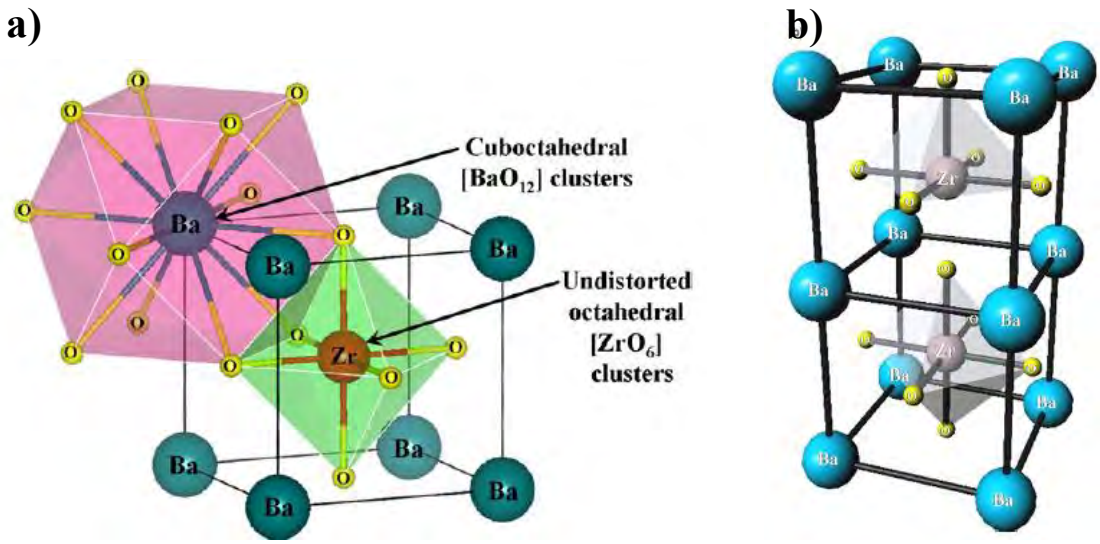

Fig. 5 Constituent polyhedrons of $BaZrO_3$, a) barium-twelve coordinated and zirconium-six coordinated ordered polyhedrons [10], b) zirconium five-coordinated disordered polyhedron [8].

controlled by the structural order–disorder degree in the $BaZrO_3$ lattice. The increase of optical band gap energy is attributed to the reduction of disorder (defects, V_o) in the $BaZrO_3$ lattice [11].

1.2.5 Intrinsic photoluminescence.

The PL characterization of all samples were measured at room temperature and performed on an *Acton Research modular 2300* spectrofluorometer, with a 75 W Xenon lamp as excitation source. The fluorescent emission from each sample was focused onto the SP-500i spectrograph (Acton Research) and detected by a photomultiplier tube R955 (Hamamatsu) connected to an Acton Research SpectraHUB and a PC that collected all data.

After the displacement of zirconium atoms in the crystalline structure of $BaZrO_3$, disordered zirconium clusters (ZrO_5) induce the formation of intermediary energy levels inside the optical band bap. The number of the induced defects (V_o) is proportional to the distorted polyhedrons which modify the optical absorption edge of the material, decreasing its optical band gap energy due to the proportional generation of intermediary energy levels [12]. Hence when the constituent polyhedrons are not ordered, the material is not fully crystalline. In $BaZrO_3$ semiconductor the lower orbitals of the CB are dominated by the 4*d* orbitals of zirconium atoms, while the higher orbitals of the VB are dominated by the 2*p* orbitals of oxygen atoms, which are responsible of the optical band gap energy reduction. Generated localized energy levels are

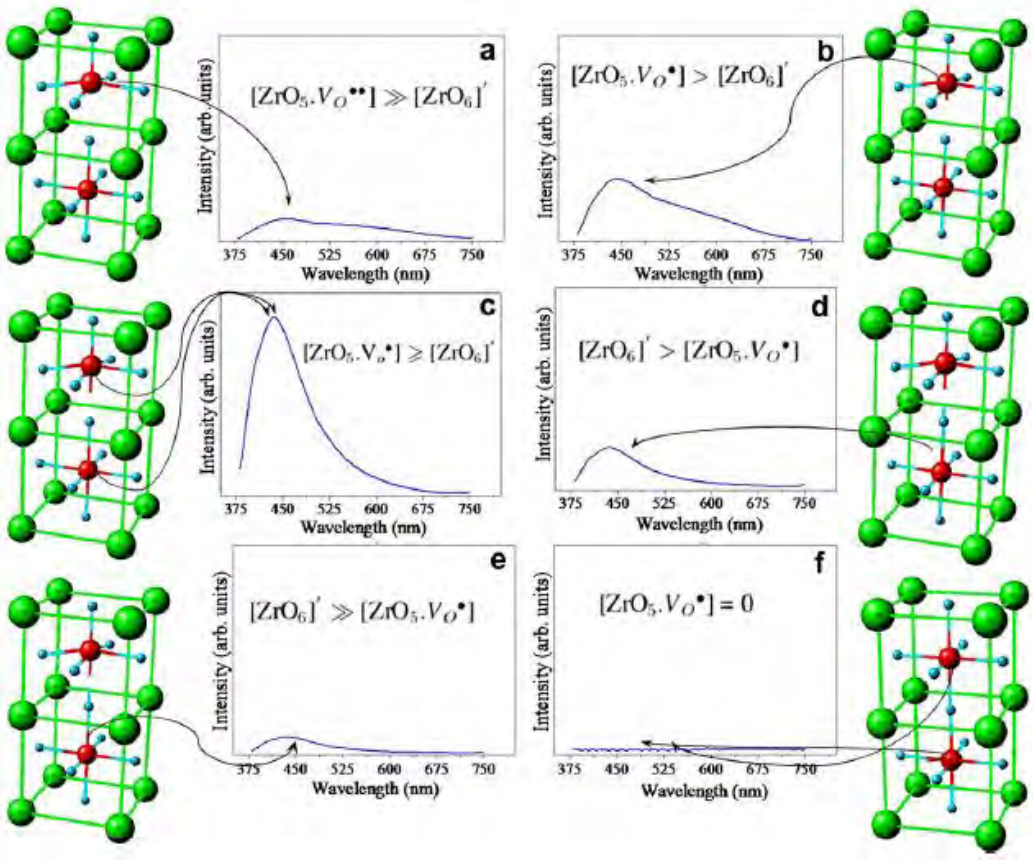

Fig. 6 PL emission spectra of six samples of $BaZrO_3$ annealed at different temperatures. Correlation between the ordered and disordered $BaZrO_3$ models with clusters of ZrO_5·Vo and ZrO_6 [11].

energetically distributed inside the optical band gap so that several photons from the irradiation source are able to excite electrons and holes trapped in the optical band gap. After proper excitation and rose of the electrons in the intermediary levels, the recombination process in which an electron below the CB lost its energy radiatively, and reoccupies an unoccupied energy level above the VB is the multiphoton process which originates the broad PL emission of $BaZrO_3$.

The PL emission spectrum of $BaZrO_3$ at RT is shown in **Fig. 6** as a function of annealing temperature for 2 h under oxygen atmosphere. In this figure from reference [11], six different samples of $BaZrO_3$ treated at 400 ˚C, 425 ˚C, 450 ˚C, 475 ˚C, 500 ˚C and 700 ˚C, show how the intrinsic PL emission of $BaZrO_3$ depend on the order–disorder degree of the crystalline structure. It can be seen that when ZrO_5 clusters and V_o in disordered $BaZrO_3$ sample (**Fig. 6 a)**) exceed ZrO_6 ordered octahedral sites, a rather weak PL emission is obtained from the 400 ˚C annealed $BaZrO_3$ sample. As the annealed temperature increases, the oxygen vacancies and ZrO_5 clusters decreases, this is the case of $BaZrO_3$ samples annealed at 425 ˚C and 450 ˚C (**Fig. 6 b)** and **c)**). From the later sample, it is presumed that when disordered ZrO_5 and ordered ZrO_6 clusters reach

balance, the broad PL emission have maximum intensity (**Fig. 6 c)**). After this point, the reduction of the broad PL emission (**Fig. 6 d)** and **e)**) is related to the increased order, enhancement in the crystalline structure due to the formation of more ZrO_6 sites, and reduction of the intermediated localized states. Finally, no PL emission is possible from the fully ordered $BaZrO_3$ sample after the annealing treatment at 700 ˚C, since increase of the annealing temperature promotes structural organization of the lattice with the formation of zirconium octahedral sites: $[ZrO_5 \cdot Vö] + ½O_2 \rightarrow ZrO_6$ (see **Fig. 6 f)**). Hence an ordered–disordered $BaZrO_3$ structure is needed to have PL emission.

1.2.6 Electron microscopy: morphology characterization.

The morphology of $BaZrO_3$ samples was investigated by scanning electron microscopy (SEM) with a JEOL XL30 microscope [4]. It has been already established that the morphological properties of $BaZrO_3$ depend strongly on the hydrothermal reaction time (RT), this can be observed on the SEM micrograph images in the **Fig. 7**. From $BaZrO_3$ samples with 2 h reaction time, amorphous particles of irregular shape and huge size dispersion were obtained (sample BZ18). By increasing the RT to 6 h, the particles morphology changes to mainly needles and in less proportion to sphere like particles (sample BZ12). The particles obtained from sample

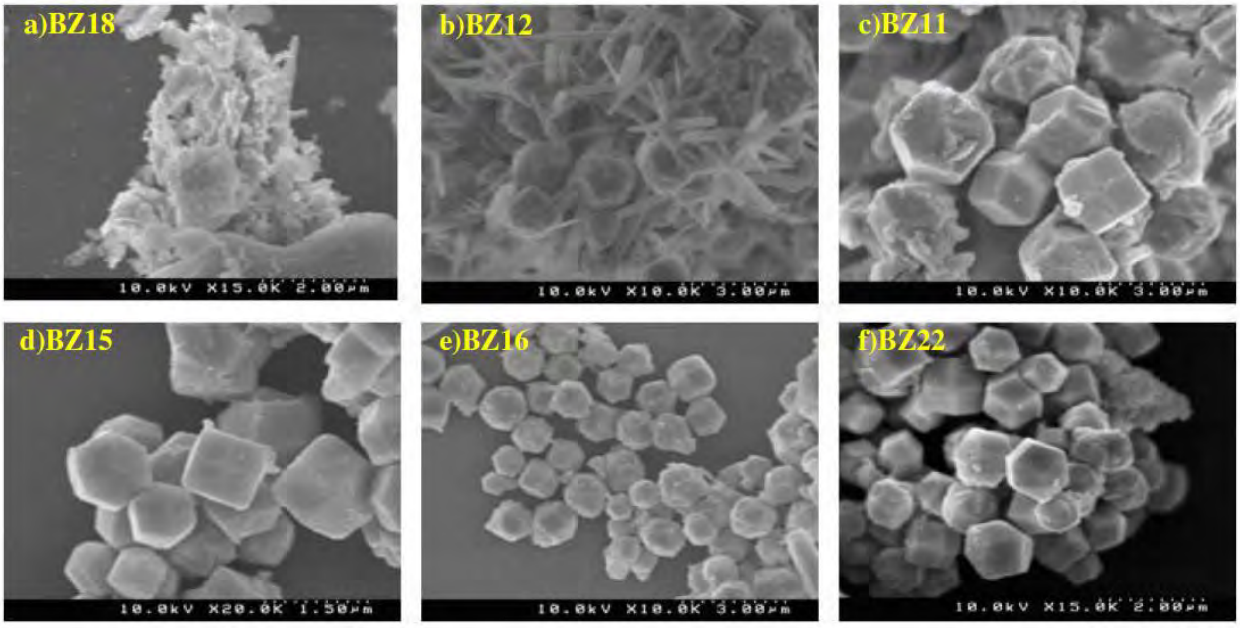

Fig. 7 Scanning electron microscopy images of a variety of $BaZrO_3$ morphologies obtained after different synthesis parameters: a) RT = 2 h, water-ethanol SR = 4:1, b) RT = 6 h, water-ethanol SR = 4:1, c) RT = 24 h, water-ethanol SR = 4:1, d) RT = 24 h, water-ethanol SR = 4:4, e) RT = 24 h, water-ethanol SR = 4:1, P123, f) RT = 24 h, water-ethanol SR = 4:4, KOH [4]

BZ11 after 24 h RT were regular faceted truncated dodecahedron; however, small irregular particles are also obtained. The best synthesis conditions in order to obtain clean particles of regular morphology corresponded to the sample with a RT of 24 h and 1:1 water to solvent ratio, regardless of the dispersant agent (CTAB or P123) and precipitant agent (NaOH or KOH), as depicted in the SEM image of sample BZ15, smaller and regular well faceted particles are observed, whereas the small irregular particles has been greatly reduced. Some changes can be observed on SEM images of samples BZ16 and BZ22, to which the dispersant agent and the precipitant agent has been changed, from CTAB to P123 and from NaOH to KOH respectively. The effect of substituting P123 results in the formation of smaller and rounder particles (700 nm), meanwhile substitution of KOH resulted on particles of around 600 nm as well as an increment of the small irregular particles.

References

1. *Blue and red emission in wide band gap BaZrO3 Yb Tm.* Borja-Urby, R., et al. 2010, Mater. Sci. Eng. B, Vol. 174, pp. 169-173.
2. *Strong broad green UV-excited photoluminescence in rare earth (RE = Ce, Eu, Dy, Er, Yb) doped barium zirconate.* Borja-Urby, R., et al. 2011, Mater. Sci. Eng. B, Vol. 176, pp. 1388-1392.
3. *Structural study, photoluminescence, and photocatalytic activity of semiconducting BaZrO3 Bi nanocrystals.* Borja-Urby, R., et al. 2011, Mater. Sci. Eng. B, Vol. 176, pp. 1382-1387.
4. *Hydrothermal syntesis and photoluminescence characterization of nanocrystalline BaZrO3.* Diaz-Torres, L. A., et al. 2010, Nanotechnology 2010, Vol. 1, pp. 360-363.
5. *A New Blue, Green and Red Upconversion Emission Nanophosphor: BaZrOEr,Yb.* Diaz-Torres, L.A., et al. 2008, J. Nanosci. Nanotechnol., Vol. 8, pp. 6425-6430.
6. *Measurement and Calculation of Optical Band Gap of Chromium Aluminum Oxiede Films.* Eunah, Kim, Zhong-Tao, Jiang and Kwangsoo, NO. 2000, J. Appl. Phys., Vol. 39, pp. 4820-4825.
7. *Optical properties and electronic structure of amorphous germanium.* Tauc, J., Grigorovici, R. and Vancu, A. 2, 1966, Phys. Stat. Sol., Vol. 15, pp. 627-637.
8. *Intense blue and green photoluminescence emissions at room temperature in barium zirconate powders.* Cavalcante, L. S., et al. 2009, J. Alloys Compd., Vol. 471, pp. 253-258.
9. *Refractive index and optical absorption properties of the complexes of a cyclobutane containing thiazolyl hydrazone ligand.* Yakuphanoglu, F., Cukurovali, A. and Yilmaz, I. 2005, Opt. Mat., Vol. 27, pp. 1363-1368.
10. *Structural refinement optical and microwave dielectric properties of BaZrO3.* Parida, S., et al. 2011, Ceram. Int. doi: 10.1016/j.ceramint.2011.10.054.
11. *Intense violet-blue photoluminescence in BaZrO3 powders A theoretical and experimental investigation of structural order-disorder.* Cavalcante, L.S., et al. 2008, Optics Comunications, Vol. 281, pp. 3715-3720.
12. *Optical absorption of Sr doped LaScO3 single crystals.* Liu, J., et al. 2007, Solid State Ionics, Vol. 178, pp. 521-526.

Chapter 2

Characterization of $BaZrO_3$ when doped and co-doped with RE ions

2.1 Color tuning emission from single doped $BaZrO_3$.

On the present chapter, the intrinsic photoluminescence emission of $BaZrO_3$ is studied as a function of the ionic radius of different rare earth which were used to doped barium zirconate. Ideal properties of $BaZrO_3$ exposed in *Chapter 1*, are now studied after doping it with Ce^{3+}, Eu^{3+}, Dy^{3+}, Er^{3+} and Yb^{3+} ions. For this reason, a unique set of samples of pure $BaZrO_3$ and 0.5 mol% RE doped $BaZrO_3$ was synthesized via the hydrothermal process at a 100 ˚C and annealed at a 1000 ˚C. The selected rare earths were chosen due to their different ionic radius, and dissemination through all of the lanthanide elements. Structural and photoluminescence characterization was performed to the as synthesized and to the annealed samples. The intrinsic photoluminescence of $BaZrO_3$ is manipulated and different colors of light: blue, red and white are obtained via down-conversion processes.

2.1.1 Structural and morphological characterizations.

Crystalline structure of the as synthesized samples (100 ˚C), and the annealed at a 1000 ˚C samples were analyzed by X-ray diffraction (XRD) spectroscopy. Out of the XRD patterns in **Fig 8**, it is possible to see well resolve and intense reflection peaks for all of the as synthesized samples, meaning the compounds already have well crystallized structures [1], moreover, the cubic perovskite phase of $BaZrO_3$ is preserved after RE ions were introduced into the compound up to a concentration of 0.5 mol%. Main reflection peaks on the XRD patterns of each sample were indexed to the standard JCPDS 06-0399 cubic phase of $BaZrO_3$. Despites the well crystallite structure of the as synthesized samples, annealing treatment was done to remove additional $BaCO_3$ phase and non reactant precursors. Increased intensity of the main reflection peaks after the annealing treatment is noticeable and it suggest enhancement of the crystallite structure of the compounds after the annealing treatment (**Fig 8**). Primitive cell parameter or lattice constant (a) of pure $BaZrO_3$ annealed at a 1000 ˚C had a value equal to a = 4.196 Å, it was calculated from the main reflection peak of $BaZrO_3$ cubic phase (BZO_c) in the XRD pattern in the direction of (110) plane, by means of **Eq. 3**, and it is in agreement with reported values found on literature [2].

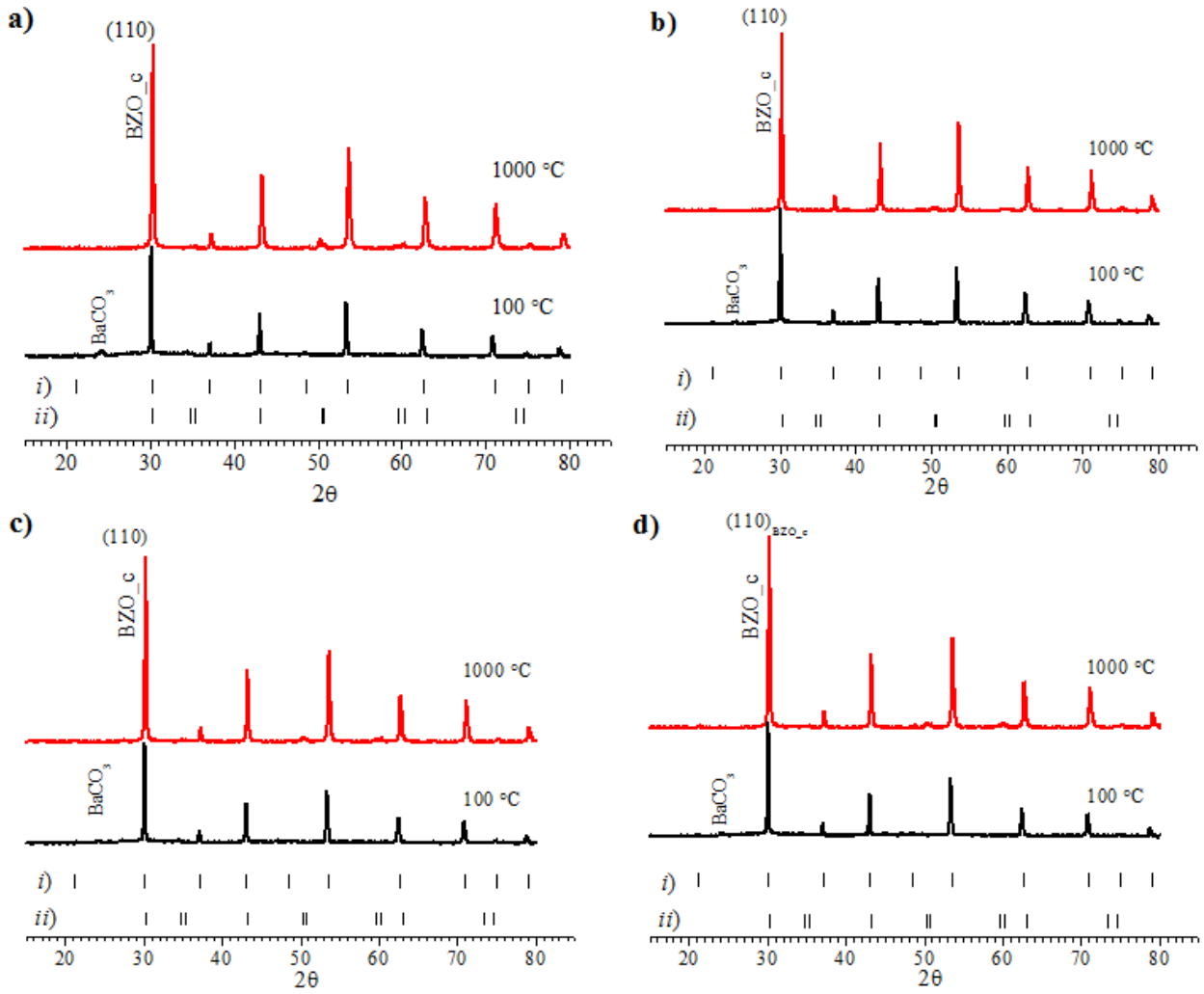

Fig. 8 X-ray diffraction patterns of as synthesized (100 ˚C) and annealed (1000 ˚C) RE dope $BaZrO_3$ samples: a) $BaZrO_3$:Ce^{3+}, b) $BaZrO_3$: Eu^{3+}, c) $BaZrO_3$:Dy^{3+} and d) $BaZrO_3$:Er^{3+}. Vertical lines at the bottom belong to JCPDS standard: *i*) 03-0699 cubic $BaZrO_3$ and *ii*) 37-148 monoclinic ZrO_2. Segregation of witherite $BaCO_3$ phase at 24.12˚ is also identified (JCPDS 45-1471).

$$a = d_i\sqrt{h^2 + k^2 + l^2} \qquad \textbf{(Eq. 3)}$$

Were $d_i = {}^{\lambda}/_{2sin\theta}$ is the interplanar distance, λ is the wavelength of the X-ray diffractometer, θ is the location of the diffraction peak, and (h, k l) are the Miller index of the plane under observation. Enlargement of the lattice constant (*a*) is commonly observed on results of $BaZrO_3$:RE research, on either case single dope or co-doped with two RE, due to bigger ionic radii of the RE ions which substitutes into the octahedral site of the smaller Zr^{4+} ions (see **Fig.5 a**)), every time the overall content of RE was increased [3,4].

Enlargement of *a* parameter is directly related with the perceived changes on the crystallite size (*d*) of the annealed samples. This can be seen in **Table 1** only for $BaZrO_3$: Er^{3+}, $BaZrO_3$: Dy^{3+} and $BaZrO_3$: Eu^{3+} samples. Their crystallite size (*d*) grew from 37.4 to 39.19 nm, due to the increasing ionic radius of 100, 103 and 107 pm, respectively, which after substitution of the RE ion enlarged the cell parameter by increasing the interplanar distance of the primitive cell. However, a discrepancy was observed for $BaZrO_3$: Yb^{3+} and $BaZrO_3$: C^{3+} samples, which had crystallite sizes of 51.42 nm and 32.92 nm respectively. A possible reason of the crystallite size variations of these samples is that ytterbium and cerium ions substituted each one as Yb^{2+} and Ce^{4+}, such valences values result in ionic radius of 128 pm and 101 pm respectively, which in turn affect the interplanar distance (d_i) and the lattice constant (*a*) of the compound giving bigger or smaller crystallite sizes correspondingly. The crystallite size of each sample was calculated by means of the Scherrer formula as given in **Eq. 4**.

$$d = \frac{k\lambda}{\beta cos\theta} \qquad \textbf{(Eq. 4)}$$

were *k* is a constant, λ is the wavelength of the X-ray diffractometer, β is the full width at half maximum (FWHM) and θ is the location of the main diffraction peak.

Despite the bigger ionic radii of RE ions than that of the Zr^{4+} (72 pm) ion, the compounds preserve the cubic phase of $BaZrO_3$ after the RE substitution with a 0.5 mol% concentration up to a 1000 ˚C. The morphology of $BaZrO_3$: Er^{3+}, $BaZrO_3$: Dy^{3+} and $BaZrO_3$: Eu^{3+} samples were analyzed via transmission electron microscopy (TEM). As it is shown in **Fig. 9**, TEM images of these compounds showed similar morphology, which consisted on aggregation of smaller grains into bigger crystallite compounds with quasi cubic morphology, and particles sizes smaller than a 100 nm. Despite expecting to note a difference in the particles size of these compounds as a consequence of their different ionic radii, enlargement of the particle size as the RE ionic radius increases could not be determine through the TEM images at hand, since no clear difference in size is noted on them.

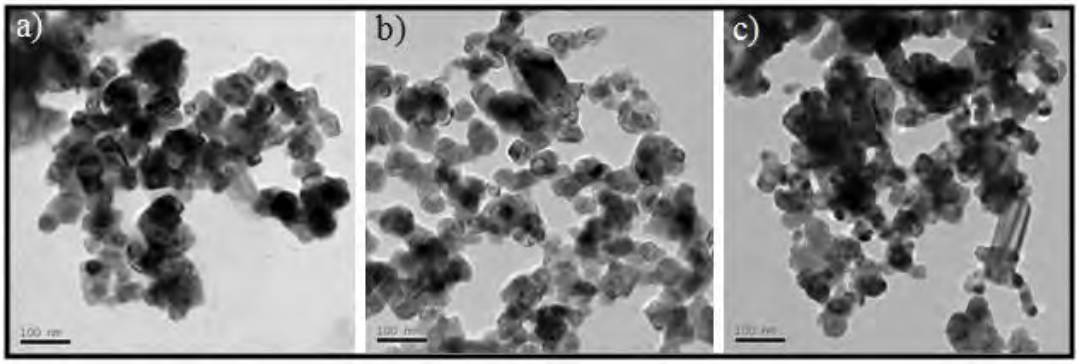

Fig. 9 TEM images of samples: a) $BaZrO_3:Er^{3+}$ (ionic radius 100 pm), b) $BaZrO_3:Dy^{3+}$ (ionic radius 103 pm) and c) $BaZrO_3:Eu^{3+}$ (ionic radius 107 pm).

2.1.2 Optical properties.

Absorption of light at room temperature by the as synthesized samples is shown in **Fig. 10 a)**. There it was observed the characteristic UV edge of $BaZrO_3$ along with the band to band transition energy located at 220 nm (45,450 cm^{-1}) in pure and doped $BaZrO_3$ of this set of samples. However, after 0.5 mol% RE substitution into the $BaZrO_3$ crystalline structure, the UV edge shifts to 300 nm in the doped samples. In the visible region of the spectrum all of the samples had the typical transparency window of $BaZrO_3$. Except for $BaZrO_3:Er^{3+}$ sample no absorption bands corresponding to the other RE ions absorption were found. This suggests the actual concentration of RE ions within the $BaZrO_3$ lattice must be smaller than 0.5 mol% and under the detection limit of the spectrophotometer. Observed absorption bands at 545 and 652 nm in $BaZrO_3:Er^{3+}$ sample, correspond to transitions from the ground state ($^4I_{15/2}$) to the energy levels $^4S_{3/2}$ and $^4F_{9/2}$ due to one photon absorption process (inset in **Fig. 10 a)**). Also observed on the absorption spectra of the as synthesized samples is the presence of water occluded in the crystalline structure. That is evidenced by the absorption band centered at 1420 nm. After the annealing treatment at a 1000 ˚C the band at 1420 nm vanishes, indicating that water had been removed off the crystalline structure of the annealed samples (see **Fig. 10 b)**). Also, the extended UV edge observed on the as synthesized samples is not on the annealed samples, preserving only the characteristic UV edge.

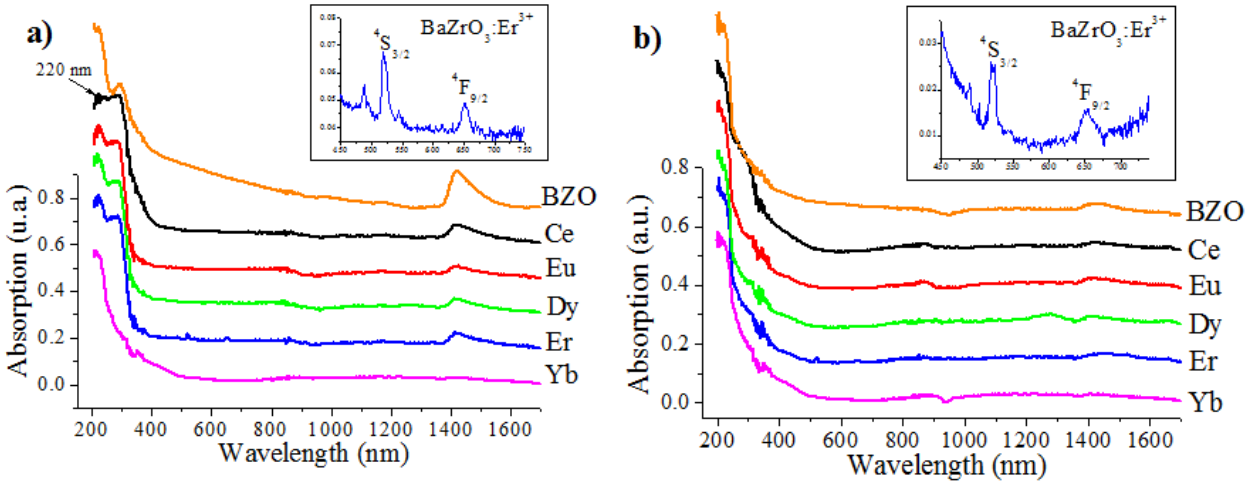

Fig. 10 UV-visible spectra of $BaZrO_3$: RE samples a) as synthesized at a 100 ˚C and b) annealed at a 1000 ˚C. In both figures the inset shows a closer view of the $^4S_{3/2}$ and $^4F_{9/2}$ erbium transitions in $BaZrO_3$: Er^{3+} sample.

The observed changes on the absorption spectra after the annealing treatment are associated to reorganization of the ions in the crystalline structure, loss of water and impurity phases [5], this is in agreement with crystalline structure enhancement evidenced by the XRD patterns shown in **Fig 8**. The absorption shoulder at 300 nm observed only in the annealed $BaZrO_3$:Ce^{3+} sample corresponds to the 4*f*→5*d* allowed transition [6,7]. The absorption bands due to Er^{3+} transitions were still observed after the annealing treatment of $BaZrO_3$:Er^{3+} sample.

Table 1 RE dopant, ionic radii for six coordinated trivalent RE, estimated band gap of as synthesized and annealed samples, and average crystallite size calculated by Scherrer formula. The first line corresponds to pure $BaZrO_3$ sample where Zr^{4+} ionic radius is given for comparison purpose.

Dopant	Ionic radius (pm)	Band gap (eV) 100 ˚C	Band gap (eV) 1000˚C	Crystallite size *d* (nm)
---	72 (Zr^{4+})	4.52	4.97	51.42
Yb	99	4.62	4.79	51.42
Er	100	3.97	4.88	37.4
Dy	103	3.93	4.93	37.41
Eu	107	3.83	4.91	39.19
Ce	114	3.82	4.65	32.92

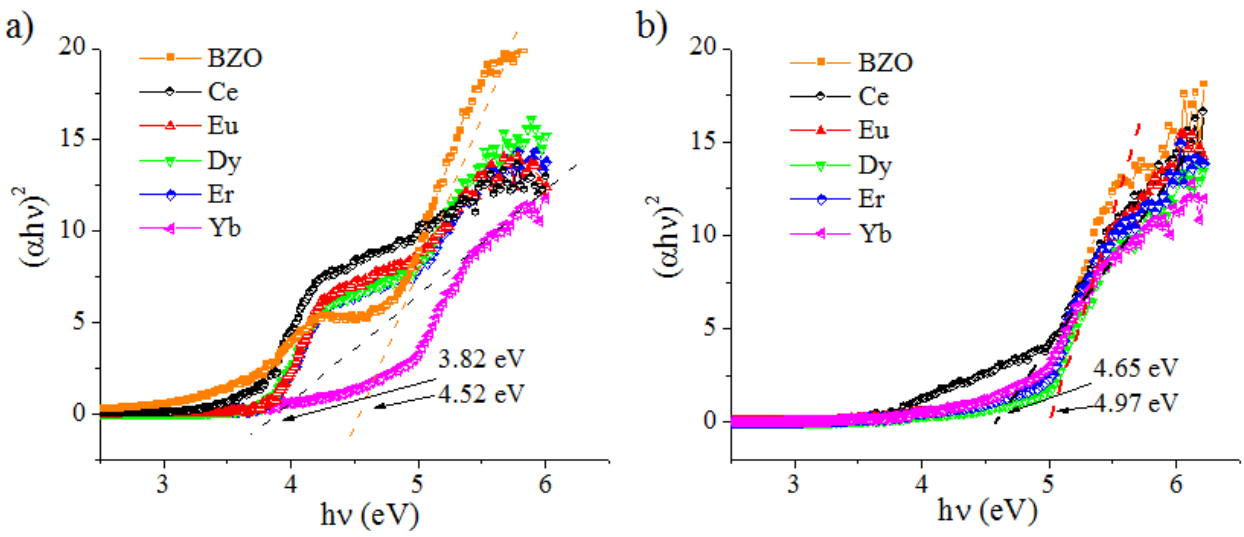

Fig. 11 Band gap estimation in Wood and Tauc plots for the diffuse reflectance in Kubelka-Munk (k/s) units, for $BaZrO_3$:RE samples: a) as synthesized and b) annealed.

The band gap energy (Eg) of each sample was estimated by transforming the information of the absorption spectra into Munk-Kubelka units, based on the relation $(\alpha h\nu)^2 = C(h\nu - Eg)$, where hν is the photon energy of incident light in eV units, C is a constant and α is the absorption coefficient. Band gap estimations of all samples are shown in **Fig. 11** in Wood and Tauc plots, where extrapolation of a straight line from the band edge of each sample to $(\alpha h\nu)^2 = 0$ gave the estimated Eg values. According to this, the band gap of the as synthesized samples lay in the range of 3.82 to 4.62 eV. As can be seen in **Table 1** the band gap narrows down to 3.82 eV as the ionic radius of substituted RE ion increases, from Er^{3+} (100 pm) to Ce^{3+} (114 pm) ions. It seems that introduction of bigger ions into the ZrO_6 octahedral site induce an enlargement of the lattice parameter *a*, which in turns provoke Zr–O bound to break in the long range, and generate oxygen vacancies (V_o) and localized states in the band gap of each compound, narrowing the band gap [4]. After annealing treatment (see **Fig. 11 b)**) the band gap of pure $BaZrO_3$ sample increased up to 4.97 eV. It is known that the band gap of $BaZrO_3$ is controlled by the structural order–disorder degree in the $BaZrO_3$ lattice, where decrement of the band gap has been associated to increments in the lattice defects, which increases the localized states in the band gap region of disordered $BaZrO_3$ samples [8]. Band gap estimation of annealed samples showed that after the annealing treatment the band gap of each sample widens due to reduction of induced defects (V_o) [2]. Thus, variations of the band gap energies of $BaZrO_3$ are affected by RE substitution due to ionic radii differences. This was clearer for the $BaZrO_3$:Ce^{3+} compound due to the bigger ionic radii difference to that of zirconium, induced the largest disorder and thus narrowed the band gap energy of this compound, see **Table 1**.

2.1.3 Color tuning of intrinsic $BaZrO_3$ emission.

Photoluminescence (PL) properties of RE doped $BaZrO_3$ after annealing treatment are shown in the excitation (**Fig. 12 a)**) and in the emission spectra (**Fig. 12 b)**). The excitation spectrum was acquired by fixing the detection at 509 nm, due to the broad band emission (400 – 600 nm) of pure $BaZrO_3$ under UV excitation observed in these samples. The excitation spectra of each sample is dominated by a broad band centered at 270 nm, which has been related to charge transfer (CT) process due to a RE–oxygen interaction [9]. A small shoulder at 239 nm was observed in the $BaZrO_3$: Dy^{3+} sample, it is associated to a charge transfer state (CTS) due to dysprosium–oxygen interactions [10]. From the excitation spectra (**Fig. 12 a)**), it was noticed for $BaZrO_3$: Eu^{3+} and $BaZrO_3$:Dy^{3+} samples a more intense excitation, which was related to wider band gaps and higher structural order of these samples (4.91 and 4.93 eV, respectively) than that of $BaZrO_3$:Ce^{3+} sample (4.65 eV) with less intense excitation. As an ordered–disordered perovskite, $BaZrO_3$ intrinsic photoluminescence properties rises after band to band transitions of excited electrons, such excited electrons get trapped in localized states which had been related to zirconium clusters due to oxygen vacancies (V_o) in the $BaZrO_3$ lattice, after electron–hole recombination taking place by several paths as a multiphoton process the broad band emission is obtained [11,12].

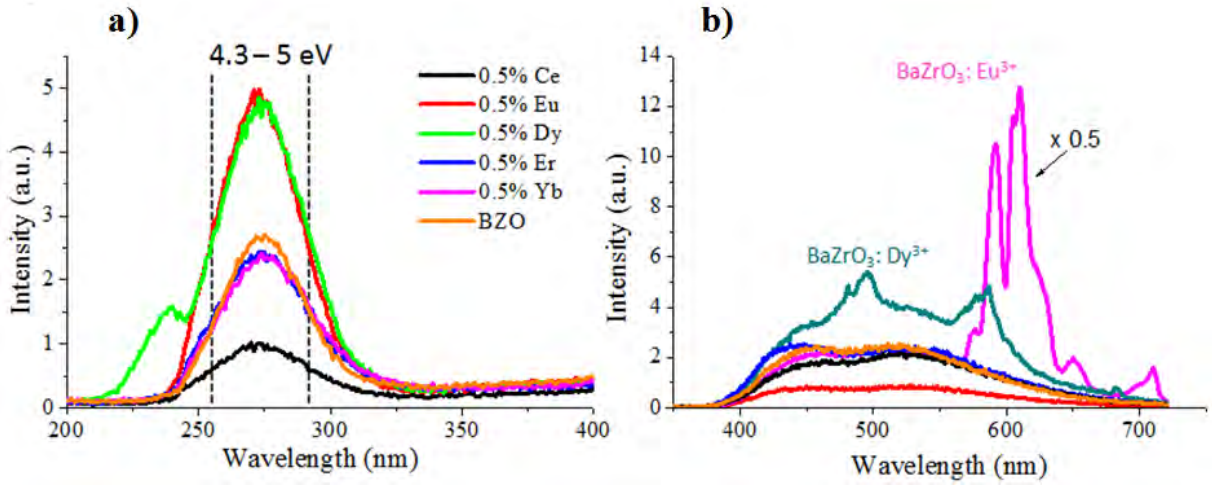

Fig. 12 Photoluminescence properties of pure and RE doped $BaZrO_3$ annealed samples at room temperature: a) excitation spectra (λ_{em} = 509 nm) and b) emission spectra (λ_{ex} = 267 nm).

PL emissions of RE doped $BaZrO_3$ samples are shown in **Fig. 12 b)**. There, the intrinsic PL emission of pure $BaZrO_3$ can be recognized as the baseline on each doped sample, from 380 nm (26,315 cm^{-1}) to 725 nm (13,793 cm^{-1}). Two physical schemes between the host and the RE ions can be observed, the first and the most notorious is that inside this range of energies ($\Delta\lambda^{-1}$ ~

13,000 cm^{-1}), the trapped electric charges inside the band gap are transferred nonradiatively to the Eu^{3+}, Dy^{3+} and Er^{3+} energetic levels: $^5D_0$, $^4F_{9/2}$ and $^4S_{3/2}$, respectively. Nonradiative energy transfer (ET) mechanisms from the host to these RE ions (see **Fig. 13**) allows for the composite emission to take place in these samples. The absence of nonradiative energy transfer mechanisms from the host to the dopant is the second scheme noticed. Due to the wide gap of energy between Ce^{3+} and Yb^{3+} energetic levels and the intrinsic emission of $BaZrO_3$, little or no contribution from these RE ions transitions were observed under direct excitation of $BaZrO_3$ at 267 nm. In the case of $BaZrO_3$:Eu^{3+} sample, in addition to the host intrinsic emission it exhibits intense emission peaks corresponding to Eu^{3+} transitions: $^5D_0 \rightarrow {}^7F_j$ (j = 0, 1, 2, 3, 4), located at 577 nm (j = 0), 590 nm (j = 1), 605 and 610 nm (j = 2), 650 nm (j = 3) and 710 nm (j = 4). Of the nature of these transitions it is known that $^5D_0 \rightarrow {}^7F_1$ is a magnetic dipole transition and that $^5D_0 \rightarrow {}^7F_j$ (j = 2,4) are electric dipole transitions. Being the latter dependent to the local electric field, it is hypersensitive to the symmetry around the europium ion. As can be seen in **Fig. 12 b)**, the more intense emission peak is located at 610 nm which correspond to the $^5D_0 \rightarrow {}^7F_2$ electric dipole transition. Introduction of Eu^{3+} ions into the Zr^{4+} sites disturbs the local field of the primitive cell after symmetry loss which is evidenced by the more intense peak emission of $^5D_0 \rightarrow {}^7F_2$ transition. This indicates most of Eu^{3+} ions are substituted in no-centro symmetric positions [9,13]. Regarding to $BaZrO_3$:Dy^{3+} sample the emission spectrum shows peaks corresponding to Dy^{3+} transitions: $^4F_{9/2} \rightarrow {}^6H_{15/2}$ (496 nm), $^4F_{9/2} \rightarrow {}^6H_{13/2}$ (588 nm) and $^4F_{9/2} \rightarrow {}^6H_{11/2}$ (682 nm). The more intense emission was that of the peak located at 496 nm, which correspond to the magnetically allowed $^4F_{9/2} \rightarrow {}^6H_{15/2}$ transition (see **Fig. 12 b)**). In addition, the strong intensity of the emission peak at 588 nm evidences the low symmetry of the sites where Dy^{3+} ions are being substituted due to the hypersensitive nature of the $^4F_{9/2} \rightarrow {}^6H_{13/2}$ transition [14]. Finally, it was observed on the emission spectra of $BaZrO_3$:Er^{3+} sample that the emission of this compound is almost that of the pure $BaZrO_3$ emission. Little contribution from Er^{3+} ions was evident from the $^4S_{3/2} \rightarrow {}^4I_{15/2}$ Er^{3+} transition at 550 nm. Such a poor contribution is an indication that the emission of Er^{3+} ions is almost completely quenched or there is not an effective energy transfer mechanism from the host to Er^{3+} ions.

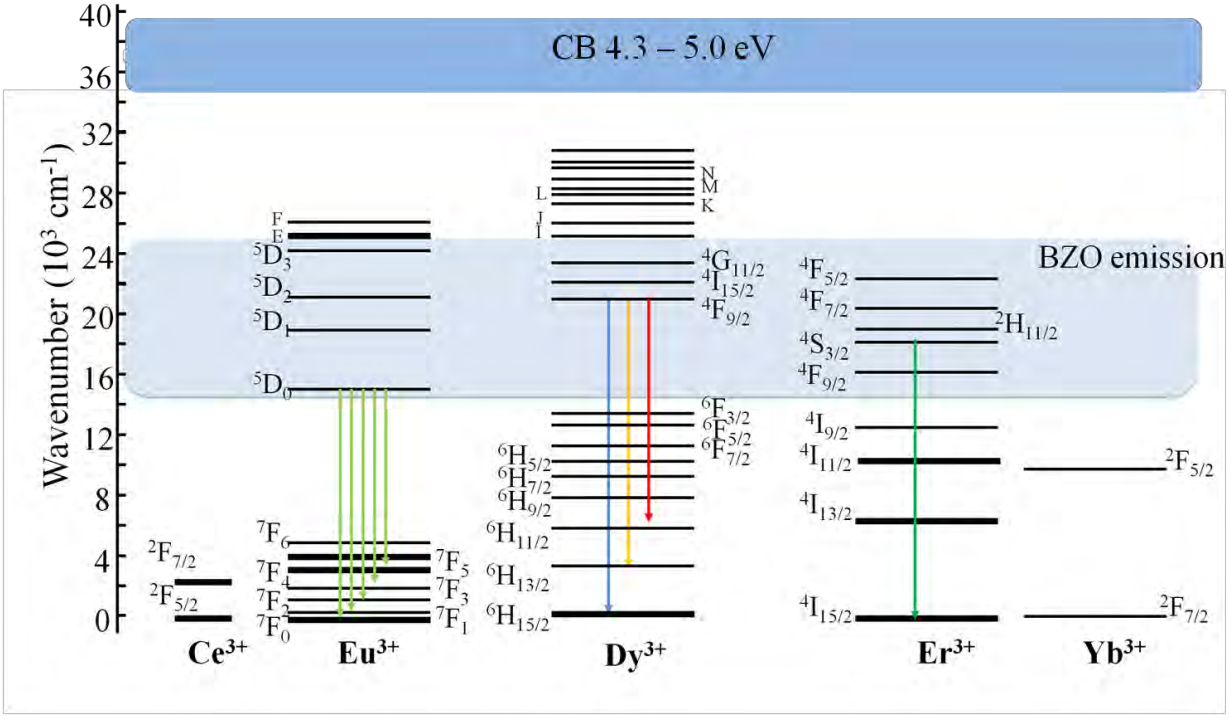

Fig. 13 Energy level diagram of RE ions showing the characteristic transitions observed in the emission spectra. Also the excitation energy signal at 267 nm, and the broad band emission of $BaZrO_3$.

2.1.4 Color coordinates.

The color of the PL emission of RE dope $BaZrO_3$ samples were defined through the emission spectra and tristimulus values of each sample via the standard color model CIE 1931 [15]. As expected under 267 nm excitation, annealed pure $BaZrO_3$ sample had the known blue–green emission, in particular, our material presented an emission with strong blue contribution which placed its emission on the color coordinates (0.259, 0.333) of the chromatic diagram (see **Fig. 14**). After RE introduction into the $BaZrO_3$ crystalline structure there was a change on the color of the $BaZrO_3$ intrinsic emission. The color coordinates and photographs of the emissions of each sample under 267 nm excitation are shown in **Fig. 15**. It is evident that samples with little or none nonradiative energy transfer mechanism had similar color emissions to that of pure $BaZrO_3$ sample with strong blue contribution and color coordinates values of: (0.275, 339), (0.267, 0.325) and (0.279, 0.357) for $BaZrO_3:Ce^{3+}$, $BaZrO_3:Er^{3+}$ and $BaZrO_3:Yb^{3+}$ respectively. However, the difference between the color emissions on each sample is notable.

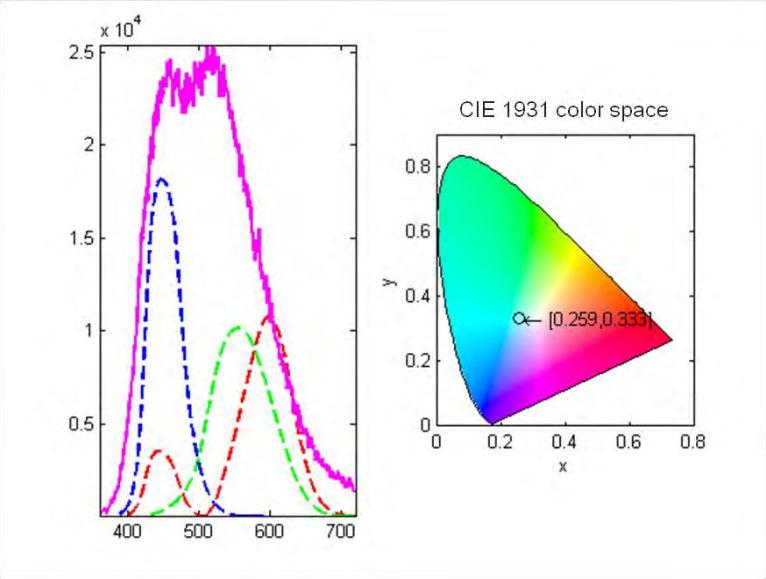

Fig. 14 Pure $BaZrO_3$ emission spectra under 267 nm excitation (solid line), and standard observer CIE 1931 triestimulus curves (dash lines). On the right, chromatic diagram showing color coordinates (0.259, 0.333) of $BaZrO_3$ sample.

Under the same excitation signal (267 nm), $BaZrO_3:Eu^{3+}$ and $BaZrO_3:Dy^{3+}$ samples had different color emissions due to nonradiative energy transfer from the host to Eu^{3+} and Dy^{3+} ions. Reddish color emission of $BaZrO_3:Eu^{3+}$ sample with color coordinates (0.454, 0.358) were obtained due to strong contribution of transitions $^5D_0 \rightarrow {}^7F_j$ (j = 2,4) from the Eu^{3+} ions. Even a more saturated red color emission, with little blue–green contribution from the host, was achieved after exciting directly the Eu^{3+} ions on the 255 nm site (39,216 cm^{-1}), which increased the Eu^{3+} ions contribution to the emitted signal. As for the $BaZrO_3:Dy^{3+}$ sample, when excited with 267 nm it had a greener emission with color coordinates (0.294, 0.365), due to the strong contributions of $^4F_{9/2} \rightarrow {}^6H_{13/2}$ transition of Dy^{3+} ions. On the other hand, when Dy^{3+} ions were directly excited at 238 nm site (42,017 cm^{-1}), the emission color turn more white with color coordinate (0.391, 0.4) due to the lost of the blue contribution from the host. New color emission of $BaZrO_3:Dy^{3+}$ sample corresponds mainly to a broad strong emission from the transitions $^4F_{9/2} \rightarrow {}^6H_j$ j = 15/2, 13/2 and 11/2 of dysprosium ions. It seems that PL emissions can be tuned by selection of: proper RE ion, excitation signal or maybe by changing the RE content when energy transfer is present.

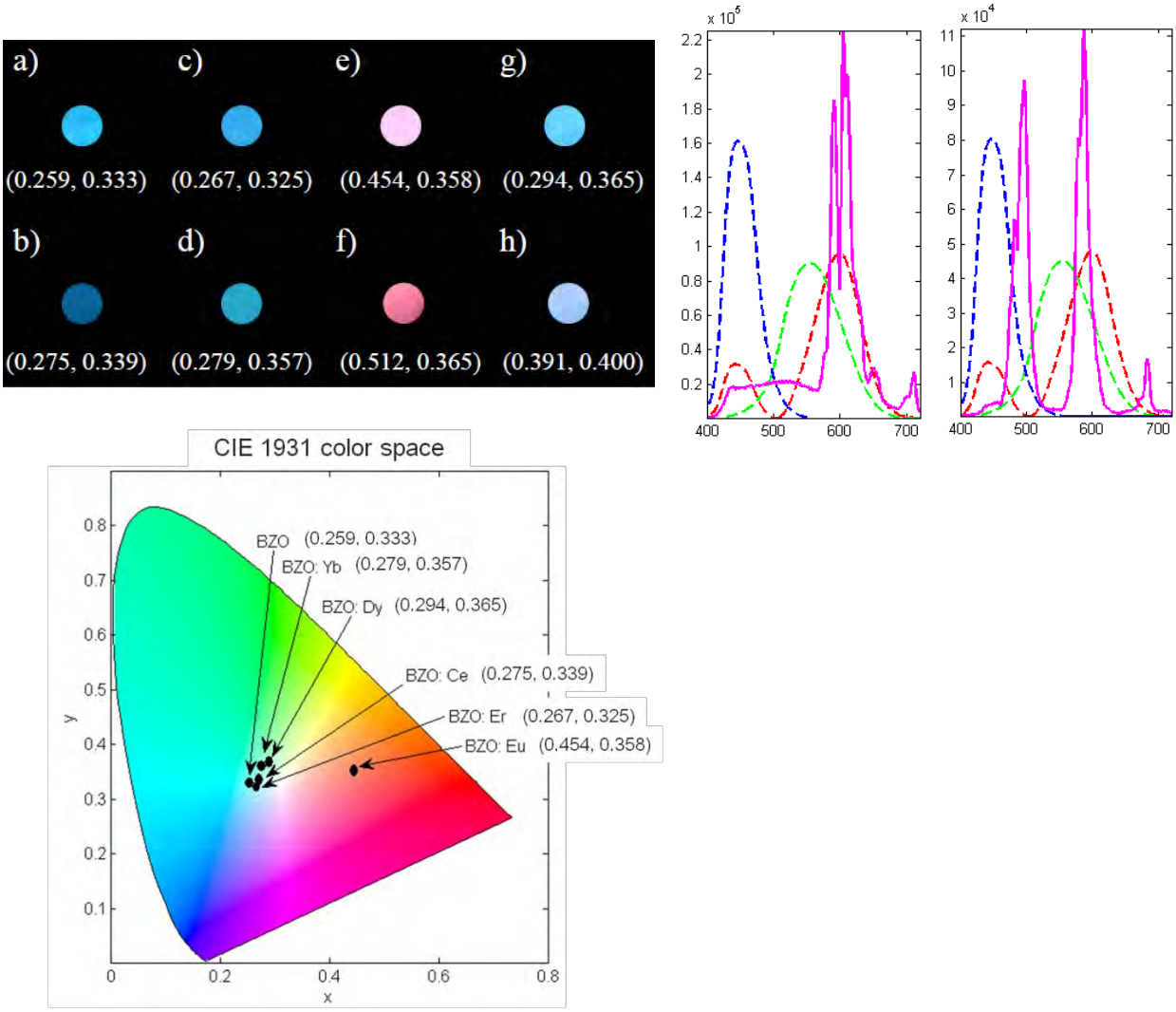

Fig. 15 Photographs of the PL emissions and the CIE 1931 color coordinates obtained under 267 nm excitation of samples: a) pure $BaZrO_3$, b) $BaZrO_3:Ce^{3+}$, c) $BaZrO_3:Er^{3+}$, d) $BaZrO_3:Yb^{3+}$, e) $BaZrO_3:Eu^{3+}$, f) $BaZrO_3:Eu^{3+}$ (λ_{exc} = 255 nm), g) $BaZrO_3:Dy^{3+}$ and h) $BaZrO_3:Dy^{3+}$ (λ_{exc} = 238 nm). On the right, $BaZrO_3:Eu^{3+}$ and BaZrO3:Dy^{3+} emission spectra (solid line) under 255 and 238 nm excitation respectively, and the Standard observer CIE 1931 triestimulus curves (dash lines). In the bottom CIE 1931 chromatic diagram with the corresponding color coordinates of RE doped $BaZrO_3$ under 267 nm excitation.

Conclusions to section 2.1

Structural, morphological, optical and photoluminescence known properties of pure $BaZrO_3$ were obtained after synthesis via the hydrothermal process. In the present work, intrinsic properties of pure $BaZrO_3$ were characterized as a function of rare earth ionic radius for rare earth single-doped $BaZrO_3$ compounds. Six different trivalent rare earths ions were used as dopant elements (Ce^{3+}, Eu^{3+}, Dy^{3+}, Er^{3+} and Yb^{3+}) with a 0.5 mol% concentration. It was found that the products obtained from the hydrothermal process at a 100 ˚C, had the cubic Perovskite

phase of pure $BaZrO_3$, and slight segregation of $BaCO_3$ and ZrO_2 byproducts, which resulted after introduction of the RE ion into the $BaZrO_3$ lattice. All compounds were annealed at a 1000 ˚C and their properties were improved after this, due to removal of byproducts and non reactant precursors. All of the $BaCO_3$ phase was eliminated and monoclinic ZrO_2 phase was reduced on each sample. Enhancement of crystalline structure of the samples was confirmed through the XRD patterns, as the reflections from the main diffraction peak became more intense. Particle size estimations of the compounds: $BaZrO_3$: Er^{3+}, $BaZrO_3$: Dy^{3+} and $BaZrO_3$: Eu^{3+}, suggested a relation of the crystal size (*d*) with the ionic radii of the substituted RE ion, as the crystallite size (*d*) of these compounds grew with the size of the ionic radius. Morphologically, all samples fitted in the nanometer scale, since all of the compounds formed particles under 100 nm size and well faceted into quasi cubic morphology. Transparency window of pure $BaZrO_3$ is also preserved after doping with RE ions and annealing the doped $BaZrO_3$ samples. Structural order of pure $BaZrO_3$ with wide band gap (4.97 eV) is also affected by the introduction of trivalent RE ions into the Zr^{4+} octahedral sites (ZrO_6). Induced Zr–O broken bonds after rare earth substitution affected the band gap energy of the compounds by narrowing the gap. The least affected compounds were those doped with Eu^{3+} and Dy^{3+} ions which induced less structural damage. Broadband PL emission of pure $BaZrO_3$ with a blue–green color under 267 nm excitation interacted with RE ions when doped. Intrinsic $BaZrO_3$ emission on $BaZrO_3$:RE samples (Eu^{3+}, Dy^{3+} and Er^{3+}) is absorbed via nonradiative energy transfer process, from host to dopant, resulting in an emission spectra composed of the intrinsic $BaZrO_3$ emission and superposition of characteristic emissions of Eu^{3+}, Dy^{3+} or Er^{3+} ions due to electron–hole recombination. Emission spectra of $BaZrO_3$:Eu^{3+} and $BaZrO_3$:Dy^{3+} samples proved that the Eu^{3+} and Dy^{3+} ions to be substituted in sites with low symmetry, which was provoked by charge difference on the site. Color tuning of the emission of RE doped samples depended on the direct interaction of the intrinsic emission of $BaZrO_3$ and the energy matching of the energy levels of the substituted rare earth with the light emitted by the $BaZrO_3$. Notable differences of color emissions were rendered under 267 nm excitation of $BaZrO_3$:RE annealed samples, samples $BaZrO_3$:Ce^{3+}, $BaZrO_3$:Er^{3+} and $BaZrO_3$:Yb^{3+} had strong blue contributions from the intrinsic PL emission of $BaZrO_3$ in their emission spectra, due to a weak or lack of nonradiative energy transfer processes between the host and the dopant. Red color emission was obtained with the $BaZrO_3$:Eu^{3+} sample, and the red color emission saturation depended on the excitation signal, a difference was found between excited the host or excite the dopant directly, where the former generated a red color emission with blue–green contribution from the host, and the later generated a more saturated red without the host contribution. The intrinsic color emission of $BaZrO_3$ was enhanced when doped with Dy^{3+} ions at 0.5 mol% concentration. A most balance PL emission spectrum is rendered with $BaZrO_3$:Dy^{3+} sample due to strong contributions of Dy^{3+} green components, and CIE 1931 color coordinates in the vicinity of pure white color were achieved.

2.2 Upconversion emission in $BaZrO_3$: Yb^{3+} Tm^{3+}.

A new set of undoped and co-doped $BaZrO_3$ samples were synthesized by the hydrothermal method. This new set of samples was characterized via optical and spectroscopic techniques so a comparison of the photoluminescence properties of such samples could be done. The characterization and analysis of the Yb^{3+}-Tm^{3+} co-doped samples is presented in the present section.

2.2.1 Structural and morphological characterizations.

Structural properties of the undoped $BaZrO_3$ and Yb^{3+}–Tm^{3+} co-doped $BaZrO_3$ annealed samples are shown in **Fig. 16**. The main characteristic diffraction peaks of these samples are in correspondence with the JCPDS 06-0399 standard for pure perovskite cubic phase of $BaZrO_3$. The crystalline structure was refined via the Rietveld method using Fullprof code [16] under the space group *Pm3m*, the computed lattice constant (*a*) of each sample showed little deviations from the reported value a = 4.193 Å in the JCPDS 06-399 standard, as can be seen on **Table 2**, along with the computed average crystallite sizes, which lay within the range from 50 to 70 nm. The standard deviation is given in parentheses and shows the variation on the last figure which indicate the minimum possible error based on their normal distribution [17]. Variations of the lattice constant and the crystallite size can be observed among the samples, and it is related to the total RE content. In the case of pure $BaZrO_3$ sample, it had a 77(4) nm crystallite size, whereas for the single doped $BaZrO_3$:0.04% Tm^{3+} sample, the crystallite size shrunk to 67(4) nm. It can be seen that after co-doping $BaZrO_3$ with 2 mol% Yb^{3+}, 0.001 mol% Tm^{3+} and 1 mol% Tm^{3+}, the average crystallite size continued to shrink to 59(3) and 50(4) nm respectively. Enhancement of the crystallite structure can be inferred from the XRD patterns of co-doped samples, as the intensity of the peaks increases from those of undoped and single doped samples, **Fig. 16**. This suggests that after RE doping the synthesized $BaZrO_3$ powders results with better densification properties and enhanced crystalline structure.

Table 2 Synthesized compound, lattice constants and average crystalline size obtained by Rietveld refinement. The standard deviations given in parentheses show the last figure variation or the number and indicate the minimum possible errors based on their normal distribution. And band gap estimation.

Compound	Lattice constant "*a*" (Å)	Average crystallite size (nm)	Band gap (eV)
BaZrO3	4.19546(2)	77(4)	4.0
BZO: 0.04 % Tm^{3+}	4.19387(2)	67(4)	4.43
BZO: 2% Yb^{3+} 0.01% Tm^{3+}	4.19634(2)	67(2)	4.35
BZO: 2% Yb^{3+} 0.001% Tm^{3+}	4.19380(3)	59(3)	3.8
BZO: 2% Yb^{3+} 1% Tm^{3+}	4.19710(2)	50(4)	4.27

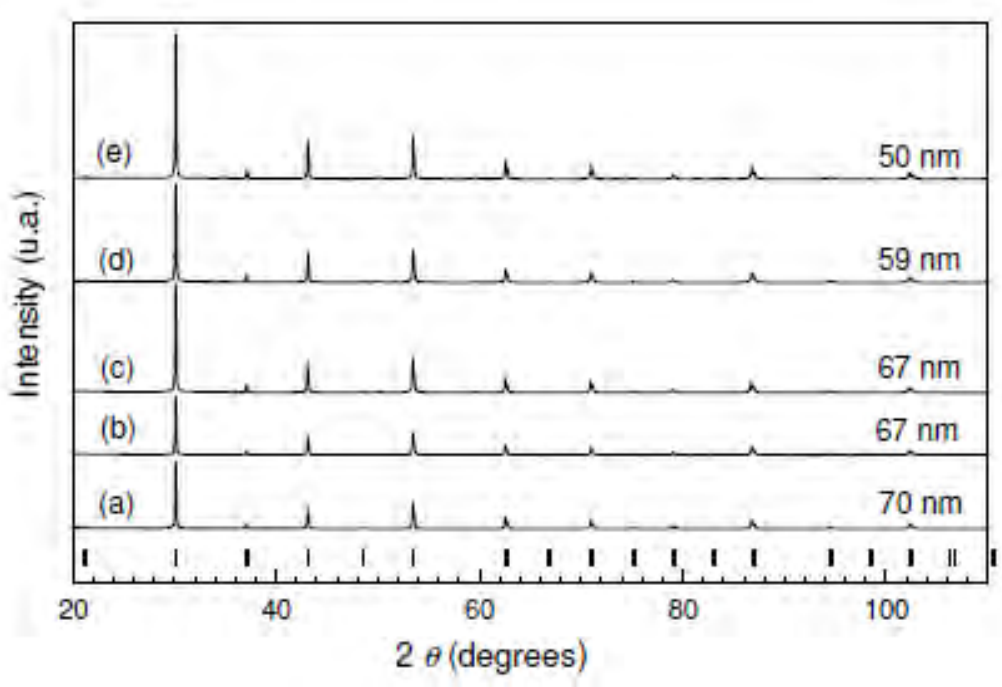

Fig. 16 X-ray diffraction patterns of $BaZrO_3$ powders a) undoped, and doped with: b) Tm^{3+} (0.04 mol%), c) Yb^{3+} (2 mol%), Tm^{3+} (0.01 mol%), d) Yb^{3+} (2 mol%), Tm^{3+} (0.001 mol%) and e) Yb^{3+} (2 mol%), Tm^{3+} (1.0 mol%). Labels on the right on each line correspond to Rietveld estimated crystallite size. Marks at the bottom correspond to JCPDS No. 06-0399 standard.

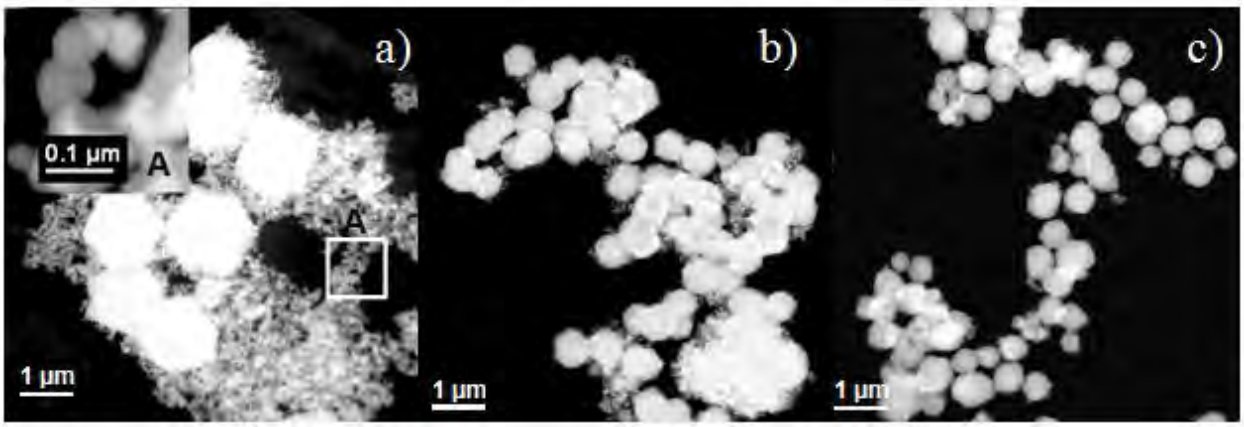

Fig. 17 HAADF image of samples: a) $BaZrO_3$: (2 mol%) Yb^{3+}, (1.0 mol%) Tm^{3+}, b) $BaZrO_3$: (2 mol%) Yb^{3+}, (0.01 mol%) Tm^{3+} and c) $BaZrO_3$: (2 mol%) Yb^{3+}, (0.001 mol%) Tm^{3+}.

Morphological characterization of samples with 1.0, 0.01 and 0.001 mol% of Tm^{3+}, and a fixed concentration of 2.0 mol% Yb^{3+}, were performed via HAADF images, and it is exhibited on **Fig. 17**. There, coexistence of big (secondary) and small (primary) particles is evidenced [18,19]. Observed morphology of the $BaZrO_3$: 2 mol% Yb^{3+} 1 mol% Tm^{3+} compound in **Fig. 17 a)**, shows secondary particles bigger than 1μm and primary nanoparticles around 70 nm in size. On the same HAADF image in the inset "A" is a higher magnification (0.1μm) of the marked primary particles, where it is possible to observe that primary particles size is smaller than 100 nm. When the content of Tm^{3+} in the compound decreases to 0.01 mol%, less primary nanoparticles were observed, and the secondary particles shrunk to particles smaller than 1μm in size, as can be seen in **Fig. 17 b)**. Similarly, for the sample with less content of Tm^{3+} ions (0.001 mol% sample), the secondary particles observed had sizes smaller than those of 0.1 mol% Tm^{3+} sample, and no appreciable presence of primary nanoparticles was observed on the corresponding HAADF image, **Fig. 17 c)**. These results show a clear tendency were the increment on the overall RE content leads to the shrinkage of the secondary particles and the reduction in quantity of the primary particles. These results agree with the XRD analyzes results in the sense that after co-doping, the intensity of the reflection peaks increases indicating the presence of a better $BaZrO_3$ crystalline structure, and in this case, the decreasing presence of the fine primary particles (Zr) in the compounds, and in turn more dense secondary particles [18,19].

Chemical analysis performed to test the content of constituent elements of the compounds via EDX is shown in **Fig. 18**. EDX results from the sample with the higher Tm^{3+} content (1 mol%) shown in **Fig. 18 a)**, revealed strong presence of atoms of barium and zirconium with similar peak intensities, this suggests that the big particles observed on this compound in **Fig. 17 a)** are constituted by the $BaZrO_3$ cubic phase. On the other hand, the EDX spectrum shown in **Fig. 18 b)** corresponds to the fine nanoparticles found in this same compound and exhibited on **Fig. 17 a)**, which have a huge proportion of zirconium in opposition to a very low content of barium. That would suggest the small particles correspond to a monoclinic zirconia phase rich in Tm^{3+} and Yb^{3+} ions. Finally, the EDX spectrum of to the sample with the lower concentration of Tm^{3+} (0.001 mol%) displayed characteristic peaks of barium and zirconium with similar intensities, suggesting again the large secondary particles on this compound have a $BaZrO_3$ phase, see **Fig. 18 c)**. Also in this case the presence of Yb^{3+} and Tm^{3+} ions was not evident because of their low concentrations are found on the detection limits of the instrument. The copper (Cu) peaks around 8 KeV, which coincides with a characteristic peak of Tm^{3+}, corresponds to the cupper grid where the sample was deposited, hence the intense peak emission.

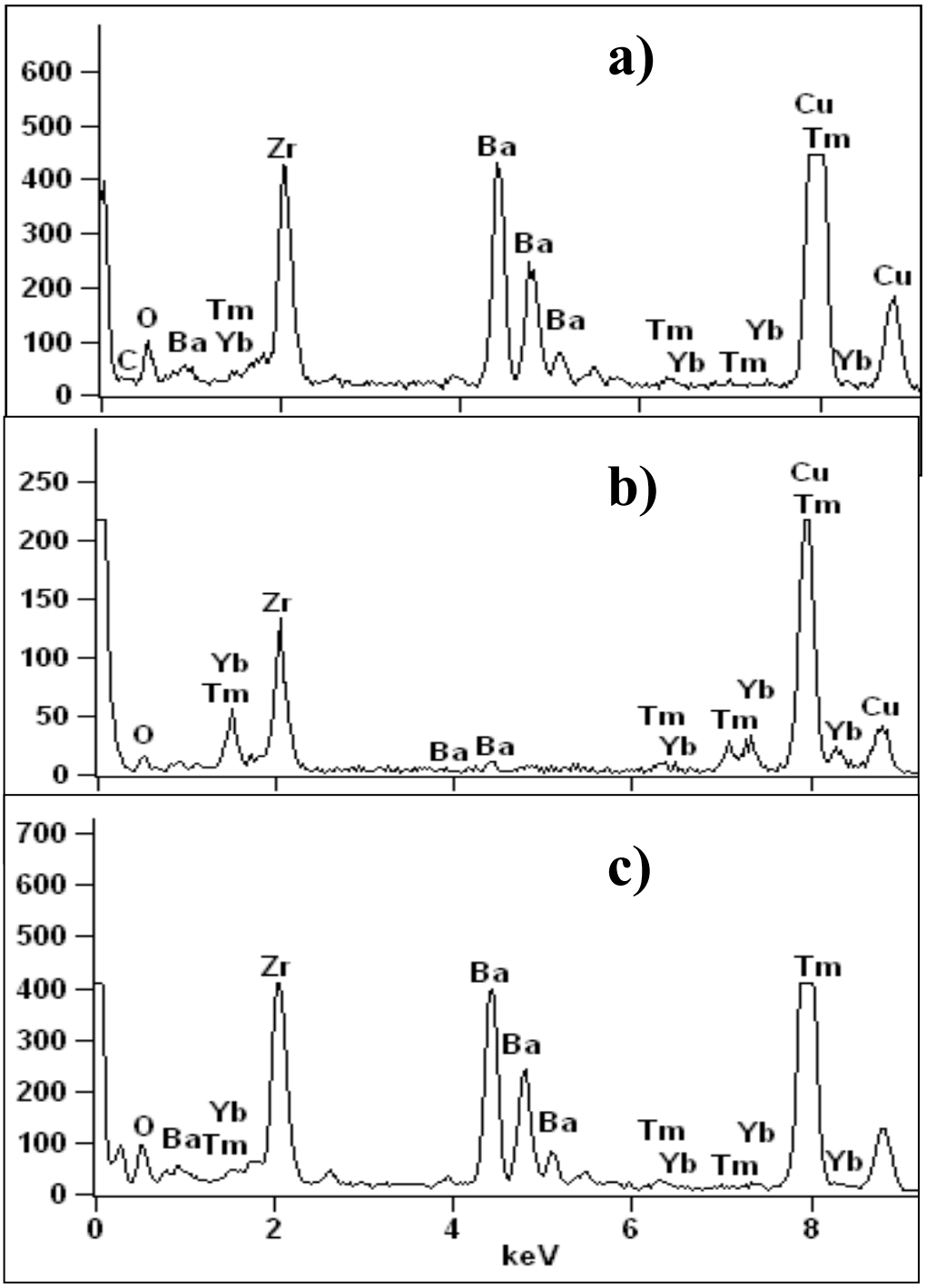

Fig. 18 EDX spectra of: a) a big particle of $BaZrO_3$: 2 mol% Yb^{3+} 1 mol% Tm^{3+} sample shown in figure 17 a), b) the primary nanoparticles inside the white square in figure 17 a), and c) a big particle of $BaZrO_3$: 2 mol% Yb^{3+}.0.001 mol% Tm^{3+} sample.

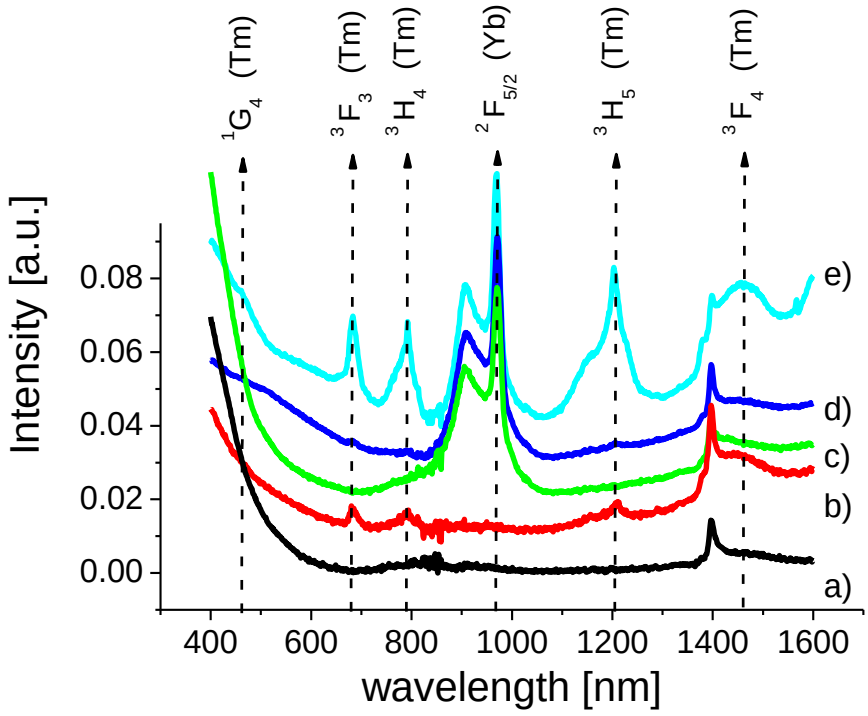

Fig. 19 Absorption spectra of $BaZrO_3$ powders a) undoped, and doped with b) Tm^{3+} (0.04 mol%), c) Yb^{3+} (2 mol%) Tm^{3+} (0.01 mol%), d) Yb^{3+} (2 mol%) Tm^{3+} (0.001 mol%), and e) Yb^{3+} (2 mol%) Tm^{3+} (1.0 mol%). The absorption spectra of doped samples was added a constant factor for demonstration purpose only.

2.2.2 Optical properties.

Absorption bands of co-doped samples corresponding to transitions from ground states $^2F_{7/2}$ and $^3H_6$ to higher energy levels of Yb^{3+} and Tm^{3+} ions respectively were identified on the absorption spectra in **Fig. 19**. Also the absorption spectrum of pure $BaZrO_3$ sample is shown in the same figure **a)**. There it is possible to distinguish that all observed absorption bands of Tm^{3+} ion are found in the region were pure $BaZrO_3$ absorption is weak (400–1600 nm). Moreover, for contents lower than 0.04 mol% of Tm^{3+} ions, the absorption bands cannot be resolved by the instrument, and only for the 0.04 and 1.0 mol% Tm^{3+} samples confirmation of Tm^{3+} ions in the compounds was possible. The broad band centered at 950 nm corresponds to the well known $^2F_{7/2} \rightarrow {}^2F_{5/2}$ ytterbium transition, which in this case is almost constant for all the samples doped with a fixed concentration of 2 mol%. There is also a strong peak around 1400 nm that might be assigned to occluded water within the powders.

Reflectance and wavelength data from the absorption spectra were converted to Kubelka – Munk (k/s) units and energy in electron volts (eV), respectively [20,21]. These data were combined in a Tauc plot [22] and the linear region was extrapolated in order to determine the band gap of the samples in the energy axis, as shown in **Fig. 20**. The estimated band gap values

of this new set of compounds were 4.0 eV for the pure $BaZrO_3$ sample, and 4.43 eV (0.004 mol% Tm^{3+}), 3.8 eV (2.0 mol% Yb^{3+} 0.001 mol% Tm^{3+}), 4.35 eV (2.0 mol% Yb^{3+} 0.01 mol% Tm^{3+}) and 4.27 eV (2.0 mol% Yb^{3+} 1 mol% Tm^{3+}). These values are within the range of band gap values of pure $BaZrO_3$ found in the literature [11,19]. The variations on band gap energy of these compounds are related to different degrees of disorder in their crystalline structure [23]. For the compound with the least concentration of thulium (2.0 mol% Yb^{3+} 0.001 mol% Tm^{3+}) the induced defects are mainly due to the ytterbium ion, which narrows down the gap to 3.8 eV. Increasing the concentration of thulium by one order of magnitude (2.0 mol% Yb^{3+} 0.01 mol% Tm^{3+}) helped to recover some degree of order in the crystalline structure and the gap increased to 4.35 eV. In the case of the compound with the higher concentration of thulium (2.0 mol% Yb^{3+} 1.0 mol% Tm^{3+}) it can be inferred by its band gap value (4.27 eV) that the damage caused to the crystalline structure is in the same range than that induced with the 0.01 mol% concentration of thulium. The band gap energy of these samples also might be correlated with the reduction of the crystallites sizes as RE content increases, and the aggregation of such smaller crystallites in large sized (< 100 nm) faceted particles observed in **Fig. 17**. The estimated band gap values are high enough for the visible and NIR absorptions due to Yb^{3+} and Tm^{3+} ions to take place. Also the estimated band gaps are wide enough to allow emissions even from the Tm^{3+} ($^1D_2$) excited state if such state could be populated in some fashion.

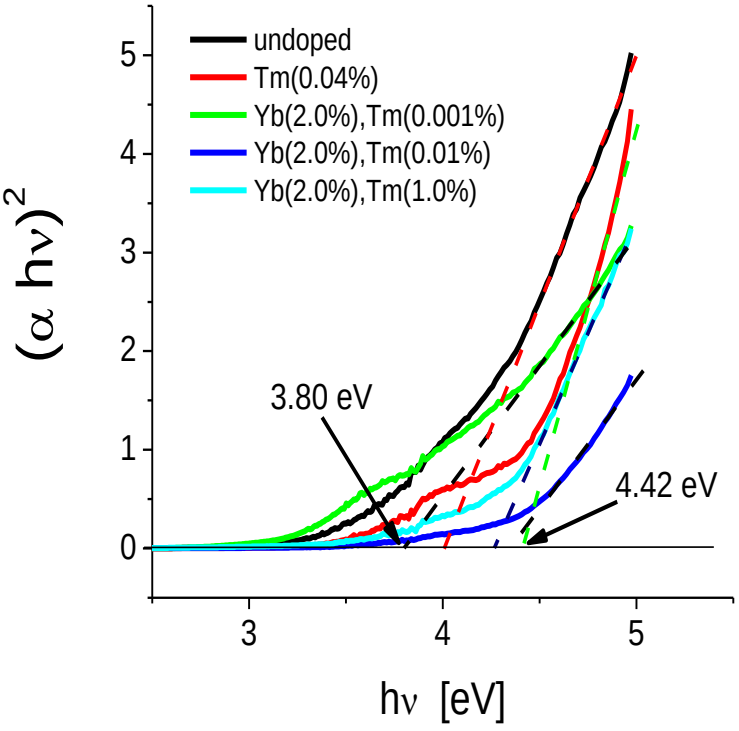

Fig. 20 Tauc plot for the diffuse reflectance in Kubelka-Munk [30-32] (k/s) units. Also, the estimation of the band gaps of $BaZrO_3$: 2.0 mol% Yb^{3+} 0.001 mol% Tm^{3+} (3.80 eV) and $BaZrO_3$: 0.004 mol% Tm^{3+} (4.42 eV) samples.

2.2.3 $BaZrO_3$: Yb^{3+} Tm^{3+} upconversion emission

Blue (484 nm), red (665 and 732 nm) and NIR (800 nm) upconversion emissions were observed in codoped $BaZrO_3$: Yb^{3+} Tm^{3+} samples, under 967 nm diode laser excitation, as shown in **Fig. 21**, under the same pump power conditions. It is interesting to note that as Tm^{3+} content increases the $BaZrO_3$: Yb^{3+} Tm^{3+} phosphor changes its emission from red (665 nm) to blue (484 nm) and again to red (732 nm) in the visible range; whereas in the NIR range (see **Fig. 21 b)**) it goes from almost no NIR emission (800 nm), for the lowest Tm^{3+} concentration (0.001 mol%), to almost only NIR emission, for the higher Tm^{3+} content (1 mol%). These broad band emissions have been assigned to the corresponding Tm^{3+} transitions, depicted in **Fig. 21** and in **Fig. 22**. Thus, it might be possible to tune the color emission from blue to red by carefully choosing the Yb^{3+} and Tm^{3+} content, being the Tm^{3+} concentration the most critical parameter. This is a relevant result since one of the drawbacks of several green emitters for LED pumped white light generation resides in the inability to produce simultaneously blue and red emissions. As observed in **Fig. 21** for Tm^{3+} contents higher than 0.01 mol%, the visible emissions self quenched and the NIR emission band increases. A better practice for visible light generation will be to tailor $BaZrO_3$ phosphor between 0.001 and 0.01 mol% Tm^{3+} content. Another interesting feature observed in the emission of the $BaZrO_3$: 2 mol% Yb^{3+} 0.001 mol% Tm^{3+} sample is the presence of two green bands centered at 525 and 550 nm. These bands could be assigned either to Er^{3+} or Ho^{3+} trace ions (not substituted on purpose) or to the Tm^{3+} transitions $^1I_6 \rightarrow {}^3F_4$ and $^2D_1 \rightarrow {}^3F_4$, respectively. The former case is the most probable in spite that it was not possible to estimate the mol% concentration of Er^{3+} (or Ho^{3+}) from PL or EDX measurements with the equipment on hand. Further work is needed in order to clarify the origin of such green emissions and to estimate the concentration of other rare earth trace impurities.

For the convenience of interpretation and discussion of the excitation and emission mechanisms, an energy level scheme of Yb^{3+} and Tm^{3+} ions with the possible energy transfer processes important for the upconversion emissions is shown in **Fig. 22**. There, illustrated by different line arrows, the ytterbium pump process at 967 nm (solid-straight arrow #1), the energy transfer (ET) process from Yb^{3+} to Tm^{3+} (dashed arrows #2), the energy backtransfer (BT) from Tm^{3+} to Yb^{3+} (dash-dot arrow #3) and the crossrelaxation (CR) process within the thulium energy levels (dash-dot-dot arrows #4). Also, the multiphononic (MP) relaxation pathways are marked by wavy arrows. The bar at the top of the energy levels diagram indicates the region were the conduction band could start from the different estimations of the band gaps, being the smallest around 3.8 eV (~30,568 cm^{-1}) for the $BaZrO_3$:2.0 mol% Yb^{3+} 0.001 mol% Tm^{3+} sample.

Due to the high concentration of Yb^{3+} ions a strong absorption of the pumping energy is expected through the resonant transition $^2F_{7/2} \rightarrow {}^2F_{5/2}$ of Yb^{3+} after which, energy transfer from

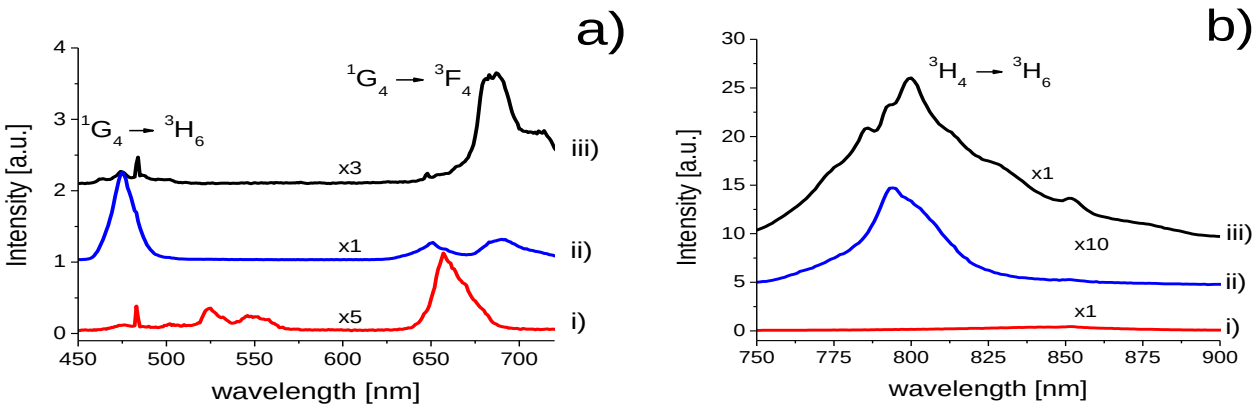

Fig. 21 a) Visible and b) NIR emissions under 967 nm diode excitation of i) $BaZrO_3$: Yb (2.0%), Tm (0.001%), ii) $BaZrO_3$: Yb (2.0%), Tm (0.01%), iii) $BaZrO_3$: Yb (2.0%), Tm (1.0%).

excited Yb^{3+} ions to Tm^{3+} ions occurs. It is clear that the 967 nm diode laser is not resonant at all with the ground absorption of Tm^{3+}, hence, in order to have population on the $^1G_4$ level, it is necessary to have three consecutive multiphonon assisted cascading ET processes from excited Yb^{3+} ions to Tm^{3+} ions, as depicted in **Fig. 22**. After these ET processes take place Tm^{3+} ions end up with populations in the $^3H_5$, $^3F_2$ and $^1G_4$ levels. In general, population in the $^1G_4$ level relaxes radiatively to the ground state $^3H_6$ (484 nm) and lower lying levels $^3H_5$ (732 nm) and $^3F_4$ (665 nm). The emission spectra **(i)** in **Fig. 21 a)** suggest that for low Tm^{3+} concentration the main channel of depopulation of the $^1G_4$ state is through the radiative transition $^1G_4 \rightarrow {}^3F_4$. As the Tm^{3+} concentration increases a more intense PL emission is expected, however, the CR process starts to be important and as a consequence population in the $^1G_4$ reduces, favoring that of $^3H_4$, $^3H_5$ and $^3F_4$ levels. Such process in turn start a bottleneck for the red emissions transitions since the ending levels $^3H_5$ and $^3F_4$ are already occupied, and the NIR emission at 800 nm is promoted due to $^3H_4 \rightarrow {}^3H_6$ radiative transition. The overall result is a relative reduction of the red emissions, and an increased emission of both blue and NIR emissios, as showed in curves **(ii)** in **Fig. 21 a)** and **b)**. Finally if the Tm^{3+} concentration is increased to 1mol%, again an enhancement of the PL emission is expected due to the concentration increment, but for this concentration the CR process become very strong and it almost depopulate the $^1G_4$ level and populates the $^3H_4$, $^3H_5$ and $^3F_4$ levels, resulting in a strong quenching of the blue and red emissions, and in a dramatic increase of the NIR emission ($^3H_4 \rightarrow {}^3H_6$), which is the case of the $BaZrO_3$: 2.0 mol% Yb^{3+} 1 mol% Tm^{3+} sample, whose emissions are depicted in curves **(iii)** on **Fig. 21 a)** and **b)**. It can be concluded that the CR process is the dominant process to be controlled through the manipulation of Tm^{3+} concentration in order to tune the overall color of the codoped $BaZrO_3$: Yb^{3+} Tm^{3+} phosphors.

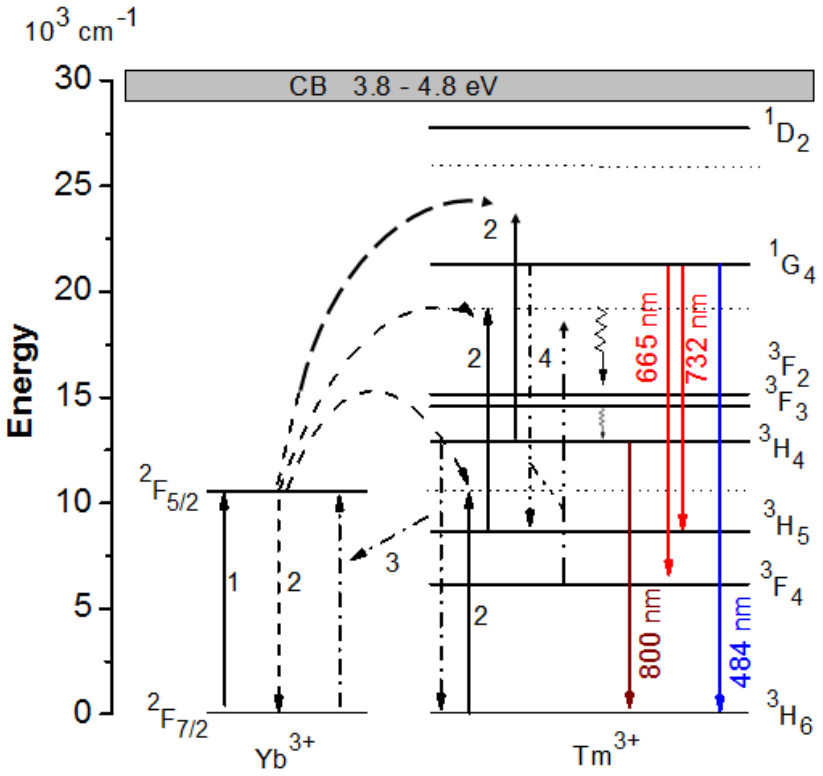

Fig. 22 Energy level diagram of $BaZrO_3$: Yb^{3+}, Tm^{3+} compound.

Conclusions to section 2.2

Characterization of the $BaZrO_3$ perovskite codoped with Yb^{3+} and Tm^{3+} ions seeking blue light generation probe to be a viable phosphor to be considered for color tuning. After codoping the host ($BaZrO_3$) with ytterbium and thulium ions, the crystalline structure of the compound is found to be improved, since the corresponding XRD patterns yields better defined and more intense diffraction peaks for the codoped compounds, than those of the single doped compound exposed in this work. Cubic morphology of the compounds is obtained as a result of a typical hydrothermal synthesis and annealing treatment at a 1000 ˚C for all samples. Upon variations of Tm^{3+} concentration in the compound, changes on the morphology of the compound can be appreciated. In general, as the Tm^{3+} concentration increases into the $BaZrO_3$ lattice, the well faceted cubic crystallites ranging in sizes from 50 to 70 nm, agglomerates into larger secondary particles coexisting both types of particles in the compounds. As thulium content increases from 0.001% to 1%, only the fine nanoparticles of 50 nm remain. Introduction of Tm^{3+} ions into the compound aided the formation of more dense particles, preserving the $BaZrO_3$ phase, improving also the order of the compound widening the band gap. The band gap values of pure and Yb^{3+}-Tm^{3+} codoped $BaZrO_3$ compounds was found to be around 4 eV, inside which the

localized states due to RE introduction are localized and visible and NIR emissions are possible. Also there is a change in the PL emissions of the compounds after Tm^{3+} concentration. As thulium concentration increases the PL emission color change from red to blue and again to red, whereas for the NIR emission, it increases from practically none emission to almost only NIR emission, when Tm^{3+} content reaches 1 mol%. It is clear that color emission from these compounds can be controlled by regulating the thulium content. Due to the inability of thulium ions to absorb the excitation from the diode laser, ytterbium ions are needed as sensitizers. In order to have such color emissions, the level $^1G_4$ of thulium most get excited through energy transfer from the excited ytterbium ions and consecutive multiphonon processes. After this, excited thulium ions relax to lower energy levels form where the visible and NIR emissions originate. When slightly doped with Tm^{3+} ions, the compound had only a weak red emission. When the concentration of thulium was increased, it was observed that the NIR emission become more intense due to the strong interaction between the Tm^{3+} ions via crossrelaxation mechanisms, which turn to be the critical parameter in this system to be controled in order to have blue or red emission. To this ends, it was found more appropriated to use Tm^{3+} concentrations between 0.001 and 0.01 mol%.

References

1. *A New Blue, Green and Red Upconversion Emission Nanophosphor: BaZrOEr,Yb.* Diaz-Torres, L.A., et al. 2008, J. Nanosci. Nanotechnol., Vol. 8, pp. 6425-6430.
2. *Annealing effect on the luminescence properties of BaZrO3 Yb3+ microrystals.* Oliva, J., et al. 2008, J. Appl. Phys., Vol. 104, p. 023505.
3. *Blue and red emission in wide band gap BaZrO3 Yb Tm.* Borja-Urby, R., et al. 2010, Mater. Sci. Eng. B, Vol. 174, pp. 169-173.
4. *Preparation and luminescence properties of BaZrO3 Eu phosphor powders.* Liu, Xiaohua and Wang, Xiaodong. 2007, Opt. Mater., Vol. 30, pp. 626-629.
5. *On the development of high density barium metazirconate (BaZrO3) ceramics.* Abdul-Majeed, Azad, Selvarajan, Subramaniam and Teng Wang, Dung. 2002, Journal of Alloys and Compounds, Vol. 334, pp. 118-130.
6. *Solid state white light emitting systems based on CeF3 RE3+ nanoparticles and their composites with polymers.* Farheen N., Sayed, et al. 2010.
7. *Blue upconversion luminescence generation in Ce3+Gd2SiO5 crystals by infrared femtosecond laser irradiation.* Dong, Yongjun, et al. 2006, Opt. Express, Vol. 14, pp. 1899-1904.
8. *Intense blue and green photoluminescence emissions at room temperature in barium zirconate powders.* Cavalcante, L. S., et al. 2009, J. Alloys Compd., Vol. 471, pp. 253-258.
9. *Synthesis and luminescence of YlnGeO phosphors activated by dysprosium ions.* Zhang, Hongwu, et al. 2008, J. Alloys Compd., Vol. 459, pp. 103-106.
10. —. Pin-Lun, Dai, et al. 2009, Opt. Mater., Vol. 32, pp. 392-397.
11. *Synthesis and photocatalytic characterization of a new photocatalyst BaZrO3.* Yuan, Yupeng, et al. 2008, Int. Hydrogen Energy, Vol. 33, pp. 5491-5946.
12. *Synthesis of Fine Micro-sized BaZrO3 Powders Based on a Decaoctahedron Shape.* Moreira, Mario L., et al. 2, 2009, Crystal Growth & Design, Vol. 9, pp. 833-839.
13. *Luminescence properties of Eu3+ and Dy3+ doped beta BaB2O4 nanocrystals.* Zou, Wen Guo, et al. 2006, Opt. Mater, Vol. 28, pp. 988-991.
14. *Efficient photoluminescence of Dy3+ at low concentrations in nanocrystalline ZrO2.* Diaz-Torres, L. A., et al. 2008, J. Solid State Chem., Vol. 181, pp. 75-80.

15. *Color tunability of the upconvertion emission in Er Yb doped the wide band gap nanophosphors ZrO2 and Y2O3.* Meza, O., et al. 2010, Mater. Sci. Eng. B, Vol. 174, pp. 177-181.
16. *Recent advances in magnetic structure determination by neutron powder diffraction.* Rodriguez-Carvajal, Juan. 1993, Physica B: Physics of Condensed Matter, Vol. 192, pp. 55-69.
17. Prince, E. 1981, J. Appl. Crystallogr, Vol. 14, pp. 157-159.
18. *Formation mechanism of hydrous zirconia particles produced by hydrolysis of ZrOCl2 solutions II.* Matsui, K. and Ohgai, M. 6, 2000, J. Am. Ceram. Soc. , Vol. 83, pp. 1386-1392.
19. *On nanoparticle aggregation during vapor phases synthesis.* Singhal, A., et al. 4, 1999, NanoStruct. Mater. , Vol. 11, pp. 545-552.
20. Kubelka, P. and Munk, F. 1931, Z. Tech Phys, Vol. 12, p. 593.
21. *New contributions to the optics of intensely light scattering materials.* Kubelka, P. 5, 1948, J. Opt. Am., Vol. 38, pp. 448-457.
22. *Optical properties and electronic structure of amorphous germanium.* Tauc, J., Grigorovici, R. and Vancu, A. 2, 1966, Phys. Stat. Sol., Vol. 15, pp. 627-637.
23. Cavalcante, L. S., et al. 2008, J. Appl. Phys, Vol. 103, p. (art no. 063527).

Chapter 3

$BaZrO_3$ as a photocatalyst

On the present chapter, it is proven that $BaZrO_3$ can be a potentially good candidate to be use as a photocatalyst. By conventional degradation of an organic dye, photocatalytic tests were performed using $BaZrO_3$ under UV light and visible light irradiation. All of the samples were synthesized via the hydrothermal method. Photocatalytic activity of bismuth dope $BaZrO_3$ was studied upon different dosage being these: 0.01, 0.1, 0.5, 1, 5 and 10 mol% Bi. On the other hand, selected rare earths used to dope $BaZrO_3$ were: Ce^{3+}, Eu^{3+}, Dy^{3+} and Er^{3+}, all with a concentration of 0.5 mol%. The photocatalytic activity of bismuth doped $BaZrO_3$ and rare earth dope $BaZrO_3$ was studied and characterized.

3.1. Bismuth doped $BaZrO_3$.

3.1.1 Structural and morphological characterizations.

Crystalline structure characterization of bismuth doped $BaZrO_3$ samples after annealing at a 1000 ˚C was performed by X–ray diffraction (XRD) and shown in **Fig. 23**. After the introduction of bismuth ions into the $BaZrO_3$ crystalline structure, all samples with different bismuth concentrations preserve the cubic perovskite structure of $BaZrO_3$ [1], for a concentration as high as 10 mol% Bi. From the XRD patterns a well crystallized structure of the samples can be inferred as each pattern has narrow and intense reflection peaks. All of the intense reflection peaks in the patterns do match with the (JCPDS) card: 06-399 of $BaZrO_3$ cubic phase. Also, weak reflection peaks are observed in the patterns around the positions: 28.175˚ and 31.468˚, which correspond to monoclinic phase segregation of ZrO_2 [2], according to standard card JCPDS 37-148, and are shown on inset in **Fig. 23**. There, it can be seen how the intensity of such peaks increases as the concentration of bismuth increases, being this an indication that bismuth substitutes into the zirconium sites in the $BaZrO_3$ crystalline structure. Through the Rietveld refinement the phase composition of the samples was estimated [3]. Crystalline $BaZrO_3$ was refined under the space group *Pm3m*, whereas ZrO_2 was refined under the space group *P21/c.*

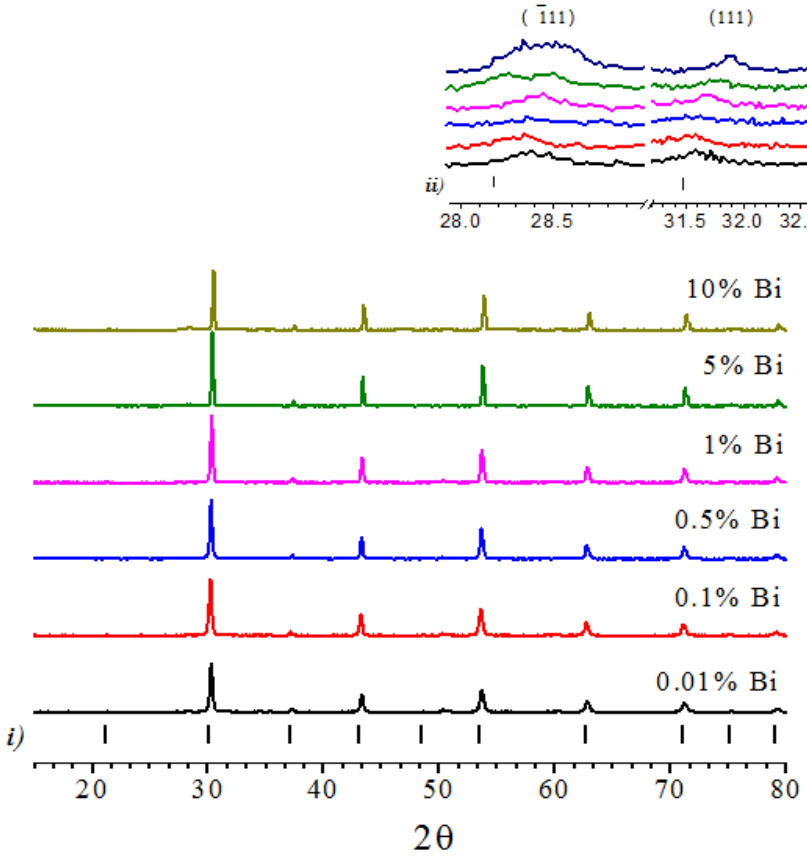

Fig. 23 Bismuth doped $BaZrO_3$ samples with cubic phase. *i)* JCPDS standard card 06-399 for cubic phase of $BaZrO_3$ and *ii)* JCPDS standard card 37-148 for monoclinic phase of ZrO_2. Inset, main diffraction peaks of segregated ZrO_2 monoclinic phase on bismuth doped $BaZrO_3$ samples.

Table 3 Rietveld refinement results.

Sample	Phase	(%)	Cell parameter (A)	Crystal size (nm)
0.01% Bi	**$BaZrO_3$**	**88.83**	**a = 4.19475 (9)**	**72(5)**
	ZrO_2	11.17		31(1)
0.1% Bi	**$BaZrO_3$**	**90.84**	**a = 4.19518 (7)**	**59(6)**
	ZrO_2	9.16		29(1)
0.5% Bi	**$BaZrO_3$**	**90.75**	**a = 4.19599 (4)**	**75(2)**
	ZrO_2	9.25		27(1)
1% Bi	**$BaZrO_3$**	**87.93**	**a = 4.19676 (5)**	**78(1)**
	ZrO_2	12.07		45(2)
5% Bi	**$BaZrO_3$**	**85.31**	**a = 4.19618 (3)**	**144(7)**
	ZrO_2	14.69		21(1)
10% Bi	**$BaZrO_3$**	**69.08**	**a = 4.19608 (3)**	**138(2)**
	ZrO_2	30.92		26(1)

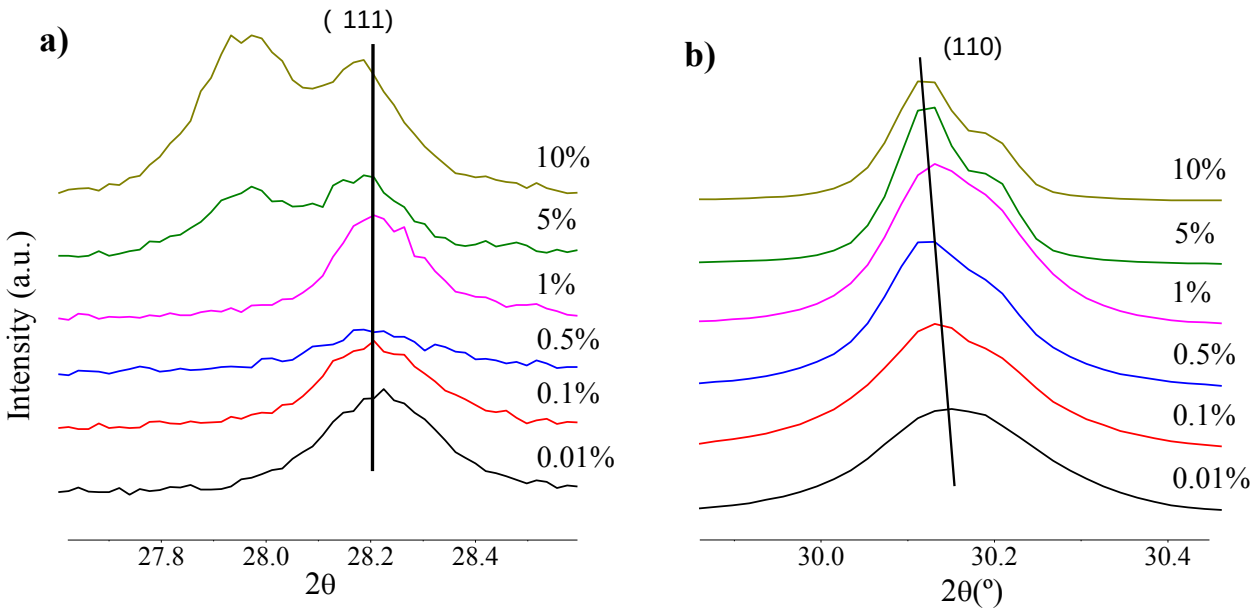

Fig. 24 Zoom into the well resolved XRD peaks of bismuth doped $BaZrO_3$ samples: a) ZrO_2 monoclinic phase (-1,1,1) plane, and b) $BaZrO_3$ cubic phase (1,1,0) plane.

Refinement results shown in **Table 3** demonstrate that with the increasing bismuth concentration, segregation of ZrO_2 monoclinic phase increases in the compound, up to 30.9% for a maximum dopant concentration of 10 mol% Bi^{3+}. A closer inspection on the main reflection peaks of both phases will reveal how bismuth substitution affects the crystalline structure of the compound. In **Fig 24** it can be seen how the position of the main reflection peak belonging to the (-111) plane of ZrO_2 monoclinic phase, remains unchanged while increasing the bismuth content in the samples. On the other hand, the main reflection peak belonging to (110) plane of $BaZrO_3$ shifted towards smaller angles every time that bismuth content was increased. According to Bragg's law, an enlargement of the distance between crystalline planes of the host should result in a shift of the diffraction peaks to smaller angles. In **Table 3**, it is shown how the primitive cell parameter (*a*) of $BaZrO_3$ cubic structure grows with bismuth concentration. It can be say then that due to the bigger ionic radii of bismuth ions (Bi^{3+}) over zirconium ions (Zr^{4+}), 103 pm and 72 pm respectively, the cell parameter of $BaZrO_3$ grows due to bismuth substitution into the octahedral site. The growth of the primitive cell reflects macroscopically on the increasing size of $BaZrO_3$ crystallites, from 72 to 144 nm as shown in **Table 3**, whereas ZrO_2 crystallite sizes are around 29 nm. This evidence supports the statement that bismuth is substituting into the zirconium sites as there is no interaction of bismuth ions with the ZrO_2 monoclinic phase. Rietveld refinement patterns of 0.1, 1 and 10 mol% Bi can be seen in **Fig. 25**. Additionally, EDXS analysis performed to the 1 mol% Bi sample proves the existence of bismuth ions in the compound. As can be seen in **Fig. 26** barium and zirconium are the main chemical components

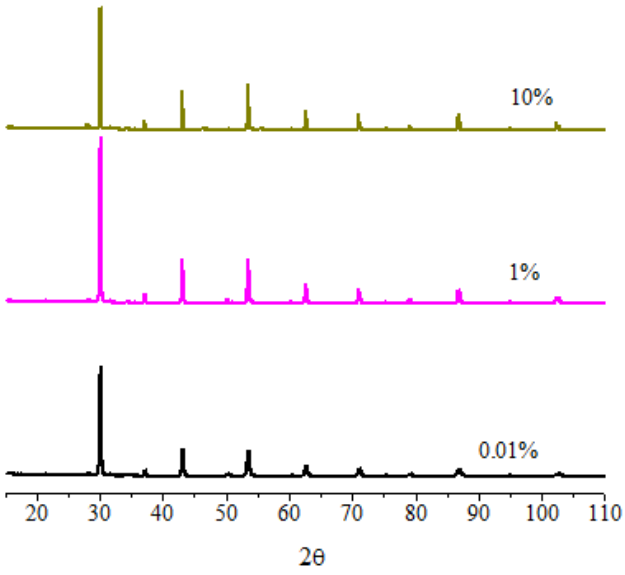

Fig. 25 Rietveld refinement of the powder XRD analysis of 0.01, 1 and 10 mol% Bi doped $BaZrO_3$ samples.

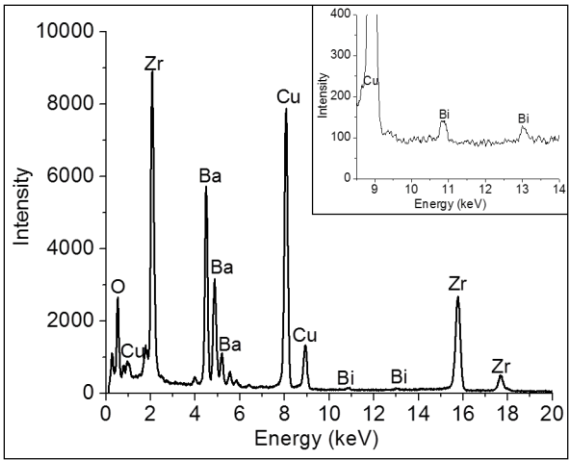

Fig. 26 Chemical analysis by EDXS of the 1 mol% Bi dope $BaZrO_3$ sample. Contribution of Cu ions belongs to the substrate used to support the sample. Bismuth ions contributions are shown in the inset.

whereas bismuth ions appear proportional to its initial doped concentration (inset).

Morphology of samples doped with 0.01, 1 and 10 mol% Bi, were analyzed via transmission electron microscopy (TEM). As observed in the TEM images (see **Fig. 27**), morphology of the compounds is made of smaller elementary particles under 100 nm in size, which agglomerate onto bigger secondary particles of irregular shape and sizes around 2μm [4]. It is evident that crystallite size increases along with bismuth increments in agreement to the Rietveld refinement results shown in **Table 3**.

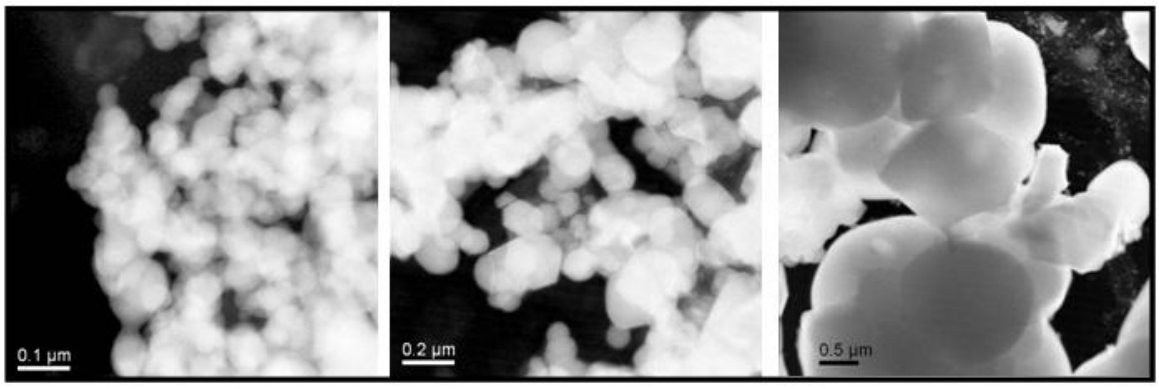

Fig. 27 Morphology of 0.01, 1 and 10 mol% Bi doped $BaZrO_3$ samples (from left to right).

3.1.2 Optical properties.

Light absorption of pure $BaZrO_3$ sample and bismuth doped samples were obtained via UV-VIS diffuse reflectance spectroscopy and shown in **Fig. 28**. As expected, the typical transparent absorption spectra of pure $BaZrO_3$ were found in the sample without bismuth. Samples doped with low bismuth concentrations (0.01 and 0.1 mol% Bi) have similar absorption spectra than that of pure $BaZrO_3$, having as well just the same UV edge absorption of pure $BaZrO_3$ [5]. On the other hand, mayor effects due to bismuth introduction were evident for dosage concentrations equal or higher than 0.5 mol%, where the UV absorption edge of $BaZrO_3$ in such samples red shifted to less energetic wavelengths as the bismuth concentration increases in the compound. It is to be noticed how these first observations relate with previously presented XRD results, in the sense that ionic radii difference between Zr^{4+} and Bi^{3+} induced structural changes in the cubic crystalline lattice of $BaZrO_3$, increasing the size of the primitive cell, and the crystallite size become larger as the bismuth concentration was increased. In the absorption spectra, it is noticeable how the UV edge moves into the visible region as the bismuth content increases, being this an indication that these compounds formed a solid solution [6]. For instance, in addition to the UV absorption edge red shift, bismuth doped samples with 0.5 and 1 mol% Bi concentrations have a wide absorption band centered into the visible region at 600 nm. The best visible light absorptions belong to highly doped samples, 5 and 10 mol% Bi, where the absorption edge extends up to 500 nm and farther than the broad absorption band centered at 600 nm. Out of this evidence, it is clear that after considerable amount of bismuth is substituted into the crystalline structure of $BaZrO_3$, structural defects due to charge difference and ionic radii differences enhance the absorption of light in the visible region of the electromagnetic spectrum.

The band gap energy (E_g) of Bi^{3+} doped $BaZrO_3$ samples was estimated from their absorption spectra after the expression: $(\alpha h\nu)^2 = C(h\nu - E_g)$. The band gap estimations lay in the range between 2.45 and 4.93 eV, as can be seen in the Wood and Tauc plots in **Fig. 29**. According to a research conducted by Cavalcante *et al*. it was reported that the optical band gap of $BaZrO_3$ narrows down as its structural order decreases, and oxygen vacancies (V_o) increases due to Zr-O broken bonds [7]. Thus it is assumed from our band gap energy estimations, of pure $BaZrO_3$ sample with a band gap energy as high as 4.93 eV, had a high degree of structural order, which is in good agreement with the values reported in literature [5,6,8]. In the case of samples with very low bismuth concentration (0.01 and 0.1 mol% Bi) the estimated band gap energies around 4.9 eV lead us to think that such a low content of bismuth ions helps to stabilize the crystalline structure, despite the electric charge differences between bismuth and zirconium ions. However, when the bismuth concentration increases, induced defects increases as well throughout the $BaZrO_3$ crystalline structure, resulting in oxygen vacancies, which narrows the band gap energy down to 2.45 eV for 10 mol% Bi concentration.

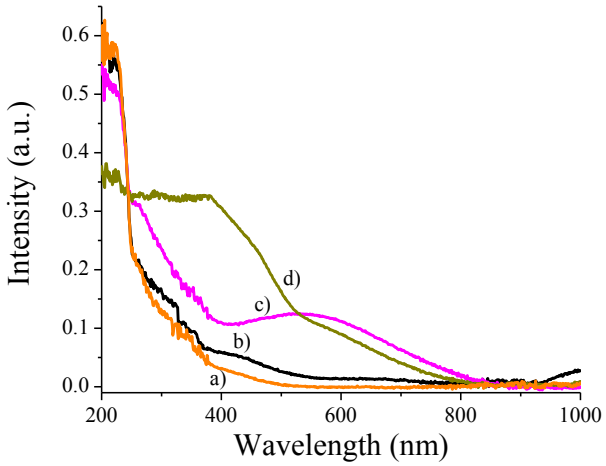

Fig. 28 UV-VIS absorption spectra of $BaZrO_3$: a) undoped, and doped with b) 0.01% Bi, c) 1% Bi and d) 10% Bi samples.

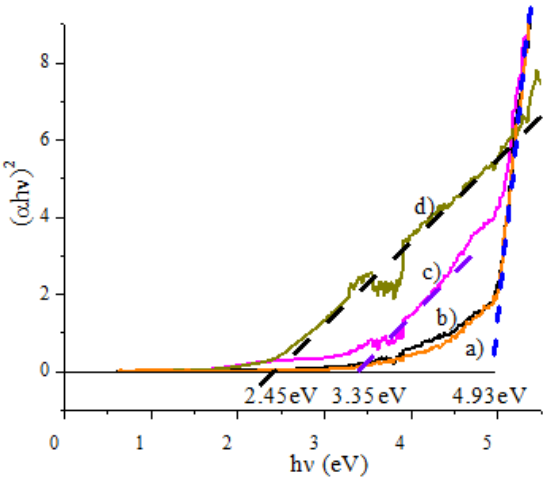

Fig. 29 Wood and Tauc plot for the diffuse reflectance in Kubelka – Munk (k/s) units. Estimation of band gaps energy of $BaZrO_3$: a) undoped; and doped with (b) 0.01 % Bi^{3+}, (c) 1% Bi^{3+} and (d) 10% Bi^{3+} at room temperature.

Hence, as the bismuth content increases, the band gap stretches monotonically allowing for less energetic wavelengths to excite these compounds, resulting in a better response to the visible light. As reported elsewhere [6], the band gap energy of pure $BaZrO_3$ is related to the energy differences between Zr 4*d* (conduction band) and O 2*p* (valance band) states. Generation of impurity levels inside the band gap as a result of doped ions substitution, and widening of the optical absorption edge into the visible region has been reported on different host like: $LnNbO_4$: Bi, (Ln = La, Gd, Y) and β-Bi_2O_3 [9,10]. Substitution of Bi ions into $LnNbO_4$, provided the system with 6*s* and 6*p* orbitals to the valance and conduction bands respectively, which further narrowed the optical band gap.

3.1.3 Enhancement of intrinsic photoluminescence of $BaZrO_3$.

Regarding to the influence of bismuth ions on the fluorescence properties of $BaZrO_3$, excitation and emission spectra are shown in **Fig. 30** and **Fig. 31** respectively, for pure and bismuth doped $BaZrO_3$. For all samples, excitation spectrum was acquired by fixing the detection at 430 nm, which is where is commonly found the $BaZrO_3$ intrinsic emission band [11]. For such an emission wavelength (430 nm) two excitation sites are found, one at 267 nm, and the other at 350 nm, in the case of pure $BaZrO_3$ sample. Both excitation sites have been related to charge transfer transitions between 2*p* and 4*d* orbitals of O^{2-} and Zr^{4+} ions respectively, in the bond they form in the octahedral site ZrO_6. Both excitation sites are mainly caused by oxygen vacancies, ZrO_5-(Vo), on the octahedral site due to broken bonds [12]. In the case of bismuth doped samples, the excitation sites changed to 300 nm and the excitation intensity is

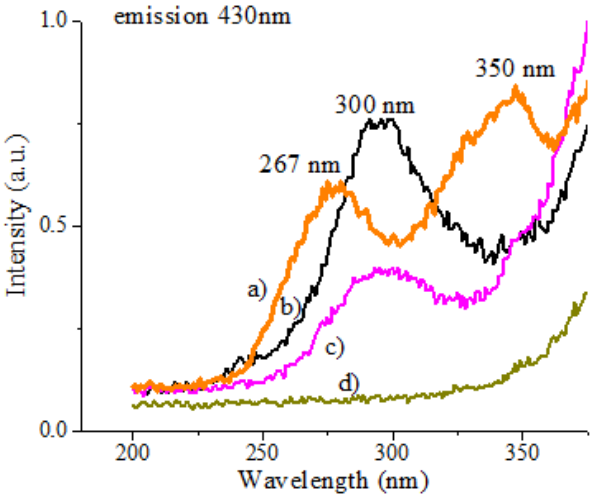

Fig. 30 Excitation spectra (λ_{em} = 430 nm) of $BaZrO_3$: a) undoped, and doped with b) 0.01 % Bi, c) 1% Bi and d) 10% Bi at room temperature.

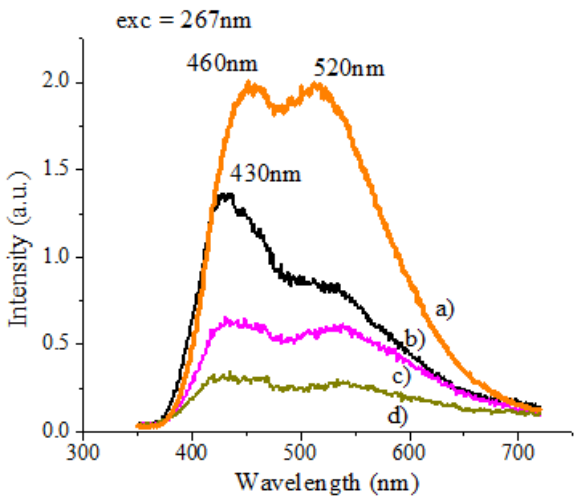

Fig. 31 Emission spectra (λ_{exc} = 267 nm) of $BaZrO_3$: a) undoped and doped with b) 0.01% Bi, c) 1% Bi and d) 10% Bi at room temperature.

more intense than at former site at 267 nm for low bismuth concentrations (0.01 mol%, see **Fig. 30**). Generation of the new site at 300 nm has been related to charge transfer from O 2*p* to Bi 6*p* orbitals in the system $LnNbO_4$ [10]. It can be seen how the intensity at 300 nm site diminishes as bismuth concentration increases until extinction of such site due to concentration quenching (10 mol% Bi). This phenomenon occurs when the distance between bismuth ions inside the crystalline structure reduces, and the interactions between them become stronger, releasing the excitation energy in a nonradiative way [10]. Photoluminescence (PL) emission of $BaZrO_3$ can be seen after excitation of the 267 nm site (see **Fig. 31**). Intrinsic PL emission of $BaZrO_3$ peaking at 460 and 520 nm has been related to localized states in the band gap and variations in the charge distribution of the unitary cell. Such a wide emission results after recombination of the electrons trapped in the energetically localized levels [12]. As expected from the excitation spectrum (**Fig. 30**), after 267 nm excitation, bismuth doped samples emission is less intense than that of pure $BaZrO_3$ under the same excitation site. This is a clear consequence of the changed excitation site from 267 to 300 nm after bismuth introduction. However, intrinsic PL emission of $BaZrO_3$ is improved under 300 nm excitation when doped with low concentration of bismuth ions, see **Fig. 32**. Low concentration of bismuth ions inside the crystalline structure of $BaZrO_3$ favors its intrinsic PL emission due to the fact that bismuth substitution into zirconium sites generates charge carriers from broken bonds. The strong quenching observed in the highly doped samples might be a consequence of charge stabilization by insertion of Bi^{3+} and Bi^{5+} pairs at first neighbor sites.

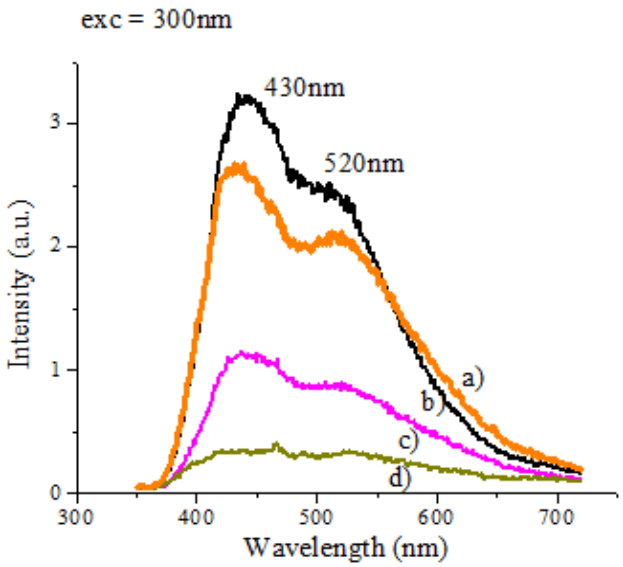

Fig. 32 Emission spectra (λ_{exc} = 300 nm) of $BaZrO_3$: a) undoped and doped with b) 0.01% Bi, c) 1% Bi and d) 10% Bi at room temperature.

Now that we have characterized $BaZrO_3$ when doped with bismuth ions, it is known that under the proper excitation it is possible to photoinduce electron-hole pairs in semiconductor $BaZrO_3$, which after recombination of e^--h^+ pairs its intrinsic PL emission is obtained. Under some restrictions, the same phenomenon is used to degrade environmental pollutants such as the organic dyes used in different industries like textile, plastic and dyeing. The process of dyeing the products generates a considerable amount of polluted water. Effluents from the textile industry have hazardous effects and have caused severe environmental problems [13]. Among a variety of techniques to revert this problem, heterogeneous photocatalysis is a viable alternative to decompose organic and no biodegradable pollution in wastewater [14]. The photocatalysis technology consist on the activation of a semiconductor compound under UV-visible light irradiation which induce the generation of photocarriers (e^--h^+ pairs) which in the context of catalysis are called oxidative species. These species react with the pollutants adsorbed on the semiconductor (photocatalyst) surface mineralizing them into CO_2, H_2O and other inorganic products [15]. The key to enhance the photocatalytic activity of semiconductors is combining effectively the photon absorption, bulk diffusion and surface transfer of photoinduced charge carriers in the photocatalyst [16]. In order to have a more efficient photocatalytic activity, recombination of the e^--h^+ pairs must be avoided so after charges separation and migration to the photocatalyst surface, photocatalytic activity takes place in a more efficient process [17].

In the following section, photocatalytic properties of rare earth and bismuth doped $BaZrO_3$ samples are evaluated in order to find out for the first time is $BaZrO_3$ could be use as a photocatalyst activated under UV-light or visible light to degrade organic dyes.

3.1.4 UV light – active photocatalytic property of $BaZrO_3$.

The performance test of $BaZrO_3$ to know if it is suitable to be used as a photocatalyst was evaluated in a homemade reactor (see **Fig. 33**), which has 3 UV lamps of 4 W each centered at 366 nm, and air circulation to keep inside temperature at 30 ˚C. Methylene blue (MB) was used as organic model substance. It is a cationic dye classified as a *heterocyclic aromatic compound* with molecular formula $C_{16}H_{18}N_3SCl$, chemical structure and absorption spectra as shown in **Fig. 34**. A 20 ml solution of distilled water and MB with a concentration of 46µM was used to test photodegradation properties of $Ba(Zr)_{1-x}Bi_xO_3$ milled powders, using 25 mg (1.25g/L) of each sample and dopant concentrations (x) of: 0.1, 1, and 10 mol % Bi. The colored solution was vigorously stirred by a magnetic stirrer. Pure $BaZrO_3$ was also tested.

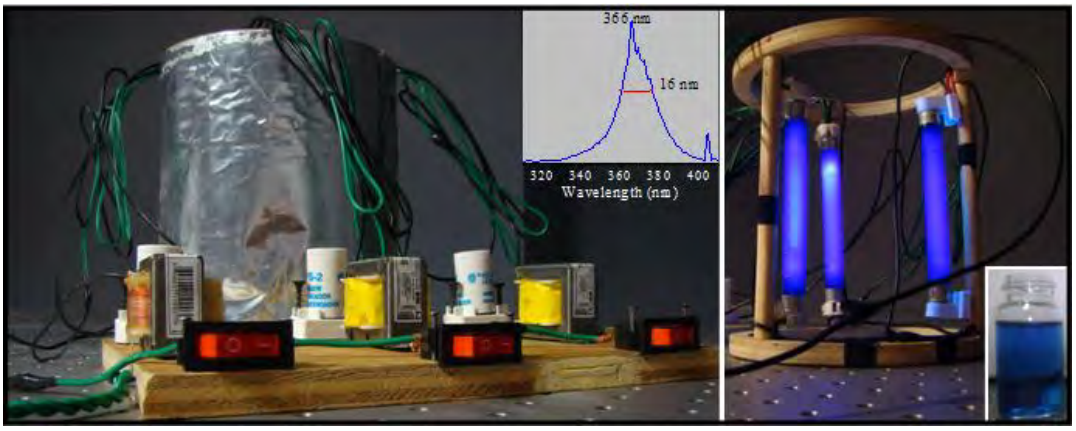

Fig. 33 Homemade reactor where photocatalytic activity of pure and dope $BaZrO_3$ samples were evaluated. From left to right: Reactor, spectral firm of the UV-light lamps centered at 366 nm and 16 nm of FWHM, distribution of lamps inside the reactor (120˚) and glass bottle with distilled water – MB solution (20ml).

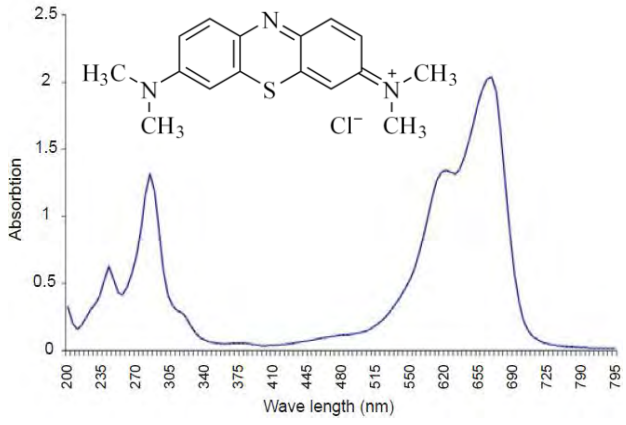

Fig. 34 Chemical structure of the heterocyclic aromatic compound Methylene blue, and its optical absorption spectrum when in aqueous phase.

By means of **Eq. 5,** the MB initial concentration (M) was estimated upon fixing the total volume (V) of the solution, limited by the container, and the desired volume (v) of MB in the solution, the latter was held one order of magnitude smaller than the former.

$$M = \frac{Cv}{V} \qquad \textbf{(Eq. 5)}$$

where C is the molar concentration of the MB source solution. **Fig. 35** shows the absorption of 664 nm light by the colored solution as a function of MB known concentrations. It is clearly seen that absorption of such light becomes stronger as the MB concentration in the solution increases. After this graph the initial concentration of MB in the solution was chosen around the middle of the concentration scale, considering having a good dynamic range on the absorption of the degraded solutions, so the spectrophotometer could work without falling out of the detection limits. The procedure followed during the experimental tests is depicted in **Fig 36**. The photocatalyst powder was added to the solution and kept in dark to allow the adsorption – desorption equilibrium process to take place. Once under UV irradiation, 400 µl were extracted off the solution at regular intervals and centrifuged at 14,000 rpm for 5 min to precipitate the photocatalyst, achieving physical separation of the powder and the solution to be analyzed. Then the absorption spectrum of the powder-free colored solution was obtained.

After 9 h under UV irradiation, MB degradation was monitored by means of UV-vis diffuse reflectance spectroscopy at the characteristic absorption band of MB around 664 nm, from a 200 µl solution extracted from the centrifuged solution. A reference solution of distilled water and MB with same concentration was used without photocatalyst in dark and under UV light irradiation during the degradation cycles (see **Fig. 37**), to have certainty on the degradation process and photocatalytic activity due to $BaZrO_3$ doped samples.

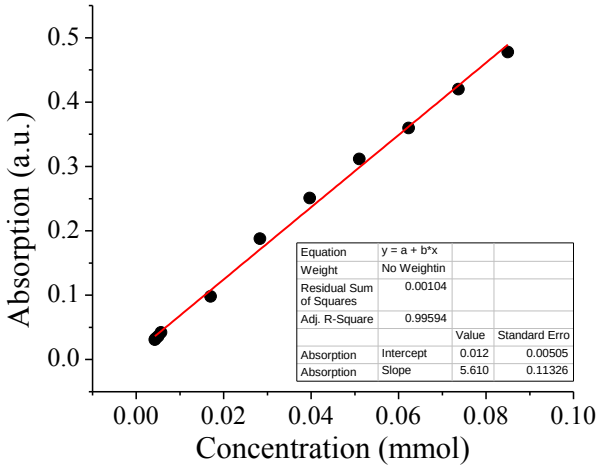

Fig. 35 Methylene blue calibration graph of Known MB concentrations in colored solution (dots) and linear adjustment (line).

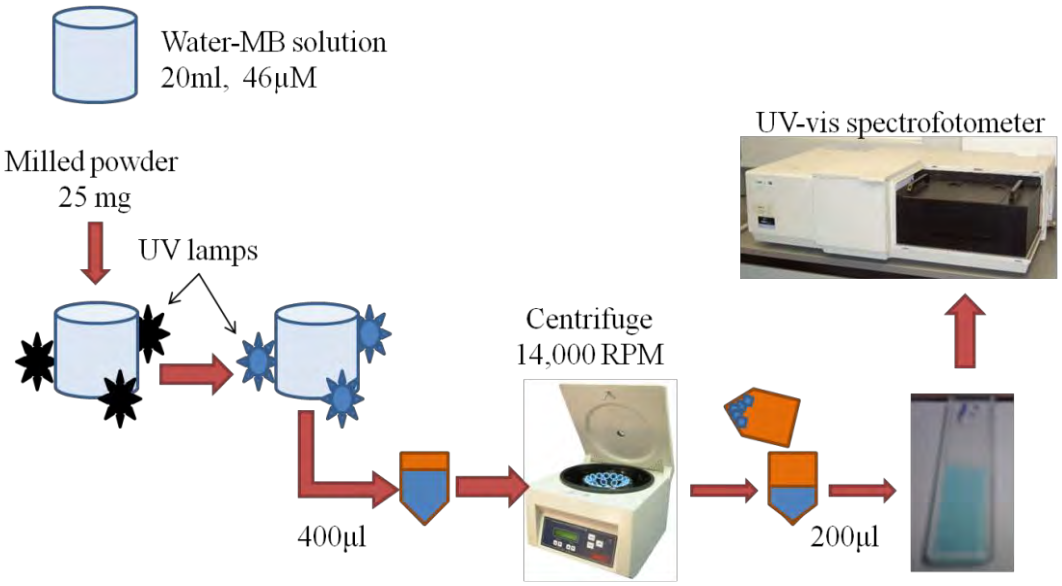

Fig. 36 Experimental procedure to test the photocatalysis properties of undoped and doped $BaZrO_3$ samples.

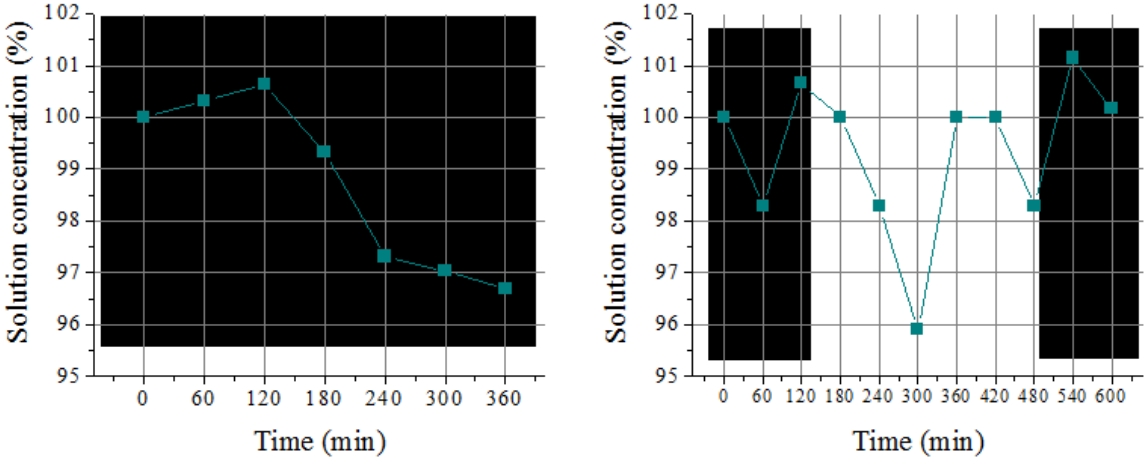

Fig. 37 Variations on the absorption spectra acquisition of the Methylene blue-water solution for 6 hours in dark (left), and irradiated by UV light (right) under continuous stirring in the homemade reactor. Variations were observed by monitoring the main absorption band of MB at 664 nm.

Once the colored solution with an initial concentration of 46µM was prepared, the experimental procedure shown in **Fig. 36** was evaluated. A metallic jacket was used to isolate the

bottle with the initial solution from spurious light. Every hour a 400 µl sample was extracted from the initial solution and its absorption spectra was obtained. It was found the absorption measurements varied along the process from one token sample to another, which reflected on concentration variations, by a maximum variation of 4% while the solution was kept in dark, see **Fig. 37** (left). It is necessary to point out that such variations do not correspond to changes on the MB concentration in the colored solution. A similar behavior occurred when the solution was exposed to UV light irradiation, shown in **Fig. 37** (right). No clear tendency on the variations could be observed as time elapsed, neither the absorption stabilized nor bleaching of the solution due to UV light irradiation took place. Precautions were taken during the set up and in the experiment process in order to avoid spurious light to interact with the solutions, and above all, to avoid sample contamination from one sample solution to another. To achieve this, laboratory lights were off, and new disposable pipet tips were use in every extraction. Absorption spectra were taken under same conditions for all samples. Despite these precautions, variations on the acquisition of the absorption spectra of MB-water solution continued. Thus it can be determine that the experimental error is around 4%.

Pure $BaZrO_3$ powder (25 mg) was introduced into a new MB-water solution in the dark in order to know how much the MB dye was adsorbed on the surface of $BaZrO_3$ powder. The adsorption-desorption process of MB on pure $BaZrO_3$ is shown in **Fig 38** (left). Once the powder was introduced, the solution remained under strong and continuous stirring in dark conditions for 6 h, the metal jacket was also used to cover the bottle. As can be seen in the figure after 120 minutes, the maximum adsorption of colorant on the $BaZrO_3$ surface took place and the concentration of the solution decreased 11%, however, after this point the concentration increased and presumably it tends to stabilize after 6 h, after which adsorption was only 9% of the initial MB concentration, indicating this that the compound surface was completely covered with MB.

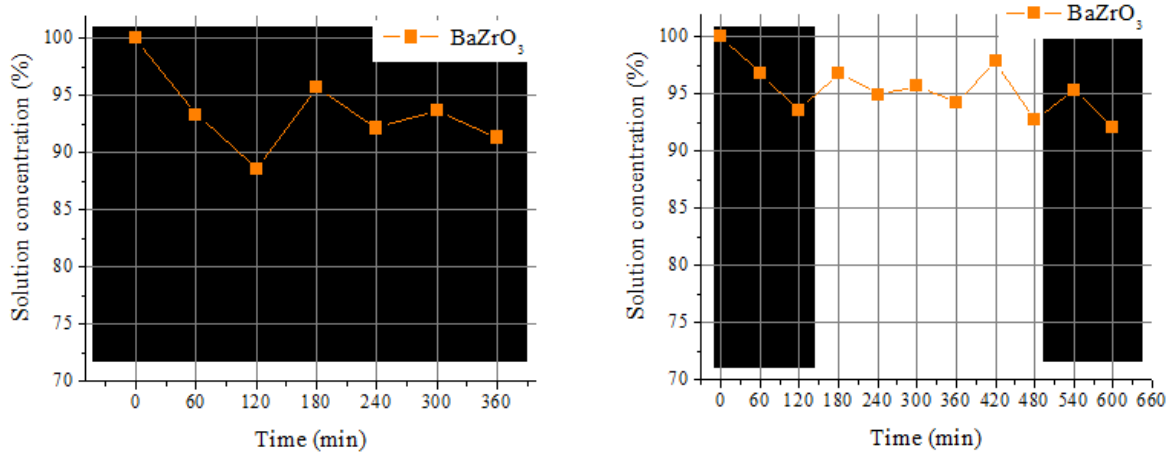

Fig. 38 Adsorption – desorption process of methylene blue on pure $BaZrO_3$ powder under constant stirring in dark (left) and photocatalytic performance of pure $BaZrO_3$ under UV light irradiation for 6 hours inside the homemade reactor (right).

After this, a new solution and another 25 mg sample of pure $BaZrO_3$ were used to study $BaZrO_3$ photocatalytic response under UV light irradiation (**Fig 38** right). The solution was left to stir for 120 min in dark, after this, the UV lamps were switched on for 6 h. Samples of the solution were extracted periodically and centrifuge to remove the catalyst powder and measure the MB concentration as a function of time under UV light irradiation. In this case after 120 min in dark, the adsorption of MB on $BaZrO_3$ surface is not as strong as it was in the previous experiment, adsorbing only 6% of MB initial concentration. In general, the figure shows there is no photocatalytic activity of pure $BaZrO_3$ under UV light, at least not enough to degrade the MB solution. The fluctuations observed on the MB concentration within 0.5 and 5% as time under UV light irradiation elapse, corresponds with the experimental error observed when the powder-free solution was kept in dark conditions.

Photocatalytic activity of pure and bismuth doped $BaZrO_3$ samples are shown in **Fig. 39**, where MB degradation is shown in percentage as a function of irradiation time. The first point in the figure stands for the initial concentration of MB dye (46µM) in the colored solution, the second point is the first measurement which accounts for both, 30 min in dark to allow the adsorption-desorption equilibrium process, and also for 15 min under UV-light irradiation. After the adsorption-desorption process, a strong fall on the MB concentration was observed up to 20%, due to the strong adsorption of MB on the compound surface, except for the 10 mol% Bi sample, which has the largest particle size hence its smaller surface area. Subsequent tested points correspond to MB degradation by the photocatalyst powder under UV-light irradiation.

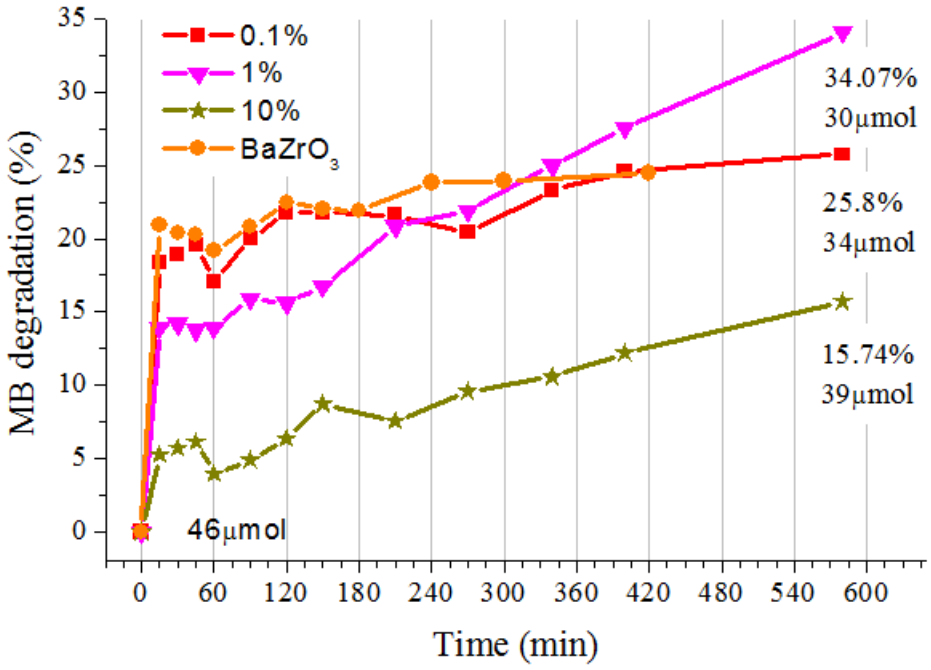

Fig. 39 Methylene blue degradation by $Ba(Zr)_{1-x}Bi_xO_3$ (x= 0, 0.1, 1 and 10) in function of time under UV–light irradiation (λ = 366 nm).

After 9 h the MB solutions were degraded by the 0.1, 1 and 10 mol% Bi samples up to 25.5%, 34.1% and 15.8% respectively. Meanwhile, pure $BaZrO_3$ sample degraded the MB solution up to 24.5%. However, it is now possible to see that after the strong adsorption of MB by $BaZrO_3$ which corresponded to a 21% of the solution degradation, the photocatalytic activity of pure $BaZrO_3$ sample was rather weak and it was found within the range of the experimental error (~ 4%) shown in **Fig 38**. The sample which had the best performance was the one doped with a bismuth concentration of 1 mol%, degrading 34.1% of the initial concentration. This is an improvement of 39.2% over the performance of the pure $BaZrO_3$ sample. Regarding to the structural and morphological properties, we might consider that such improvement is related to a smaller crystallite size of the doped sample, which implies a larger surface area of the photocatalyst interacting with the solution [18]. On the other side, despite of the smaller crystallite size of the sample with 0.1 mol% Bi (see **Table 3**) its overall photocatalytic activity is minor, 25.5%. This could be associated to the low content of bismuth in the compound. Moreover, the absorption spectra revealed a better absorption of light in the vicinity of 366 nm for the samples with a concentration of 1 mol% Bi, due to a larger red shift of the UV absorption edge (**Fig. 28**). In regard of the sample with a doping concentration of 10 mol% Bi, its photocatalytic activity is worse than that of pure $BaZrO_3$ at this excitation signal, its poor performance is associated to a mayor ZrO_2 monoclinic phase segregation (~31%), a bigger crystallite size, and more important, the absence of the excitation site at 300 nm due to concentration quenching (see **Fig. 32**), also, formation of Bi^{3+}-Bi^{5+} pairs at first neighbors that might provides recombination paths that in turn avoid the charge carriers to reach the nanocrystalline surface. On the other hand, due to the larger shift of the UV-edge into the visible region and its broad absorption band of this sample (10 mol% Bi), a more efficient excitation wavelength ought to be found out of the UV range and located anywhere inside the visible range.

3.1.5 Visible light – active photocatalytic property of $BaZrO_3$.

Photocatalytic activity of pure and bismuth dope $BaZrO_3$ activated with visible light, was evaluated by placing the distilled water – MB solutions outdoors under direct natural sunlight irradiation for a period of time of 6 hours. The experiment set up included only the magnetic stirrer, no control over temperature or air flow was implemented (see **Fig. 40**). The photocatalytic process started right after the compound (25 mg milled powder) was poured into the solution and placed outdoors under the sunlight applying vigorous stirring, without dark time for the adsorption – desorption equilibrium process to happen. The photocatalytic activity of $Ba(Zr)_{1-x}Bi_xO_3$ samples with dopant concentrations (x) of: 0, 0.1, 1, and 10 mol % Bi was evaluated every hour following the same procedure described in the last section.

Fig. 40 Set up for photodegradation of MB solution by $Ba(Zr)_{1-x}Bi_xO3$ (x= 0, 0.1, 1 and 10) photocatalyst activated by natural sunlight irradiation.

The plot of MB degradation as a function of time under natural sunlight irradiation is shown in **Fig. 42**. There, it can be seen a strong photocatalytic activity for all of the samples, degrading MB solution in 64.6% (pure $BaZrO_3$), 75.8% (0.1 mol% Bi), 77.3% (1 mol% Bi) and 87.5% (10 mol% Bi) from its original concentration. Hence, not only the photocatalytic properties of pure $BaZrO_3$ were enhance under UV light excitation after bismuth introduction, but also, bismuth doped $BaZrO_3$ compounds had a better response when excited by natural sunlight through a very simple and economic set up. The first study were the photocatalytic activity of pure $BaZrO_3$ was proved were conducted in year 2008 by Yuan et al. There pure $BaZrO_3$ produced hydrogen from water splitting under UV light. They concluded that the good photocatalytic activity of pure $BaZrO_3$ was due to its ideal perovskite structure, where the Zr-O-Zr bond angle of 180˚ allowed high carrier mobility, thus, allowing photocarriers to reach the nanocrystals surface to decompose water [8]. Essentially, in a typical redox reaction the oxidizing species (e^- - h^+) reduces and oxidizes the substrates in contact with the species. In a photocatalytic reaction the oxidative species are generated within the semiconductor by light absorption. If the incident light is sufficiently energetic (hν), electrons on the VB are promoted to the CB and at the same time, holes are generated in the VB. A possible interpretation for e^- - h^+ location is that there are sites trapping e^- or h^+ in the crystal lattice and that e^- and h^+ are trapped by these sites immediately after light absorption. Hence the phtocatalytic activity should be controlled by the density and spatial distribution of these traps in the photocatalyst [19]. Light emissions from the semiconductor must be avoided thus the oxidative species be able to interact with the substrates adsorbed on the particle surfaces. Once in the surface, the species react with adsorbed methylene blue – water solution, reducing O_2 from air and oxidizing H_2O molecules to superoxide (O_2^-) and hydroxyl (OH^-) radicals respectively, due to e^- transfer to O_2 molecules and to h^+ transfer to H_2O molecules (see **Fig. 41**). Superoxide and hydroxyl radicals further degrade the methylene blue C-H bonds and form CO_2 and H_2O as final products [20]. In the case of

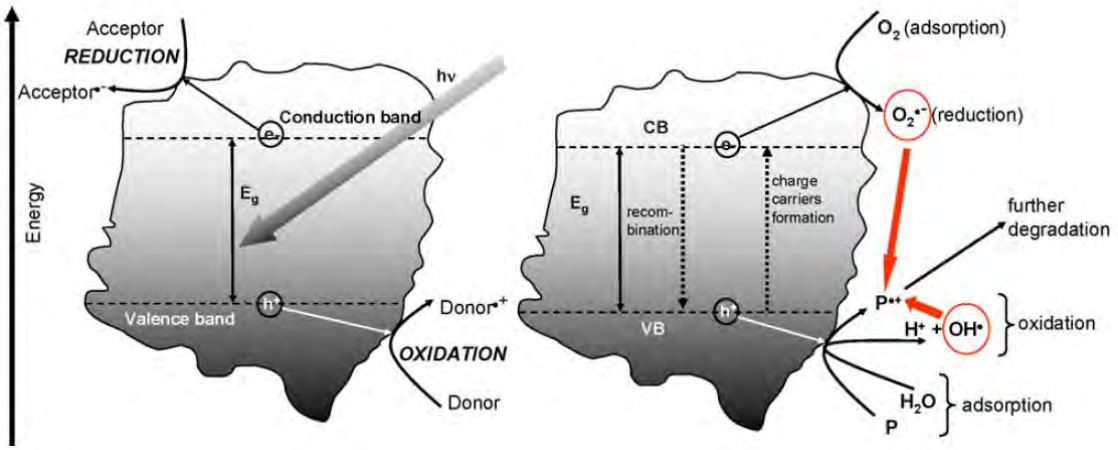

Fig. 41. Scheme of the photocatalytic reaction of semiconductor compounds, depicts the process on the surface of a nanoparticle and the interaction of the oxidizing species and the pollutant (P). [20]

aromatic compounds, the aromatic part is hydroxylated and successive steps in oxidation/ addition lead to ring opening. The resulting aldehydes and carboxylic acids are decarbonated and finally produce CO_2 [20].

As it is shown in **Fig 42**, the results of our experiments indicate that despite the bigger crystallite size of the 10 mol% Bi sample (see **Table 3**), the wider absorption band of this sample which comprehends part of the UV region and the visible region with strong absorption up to 500 nm and beyond (**Fig. 28**), provided this sample the best performance when evaluated its photocatalytic capability, degrading the MB solution up to 87.5%, improving in 35.5% the performance of pure $BaZrO_3$, under the same conditions. Visible light activation of bismuth base oxides has been related to the hybridized valance band by O 2*p* and Bi 6*s* orbitals [21]. Such hybridization widens the valance band increasing the mobility of the charge carriers, allowing them to easily reach the surface of the compound.

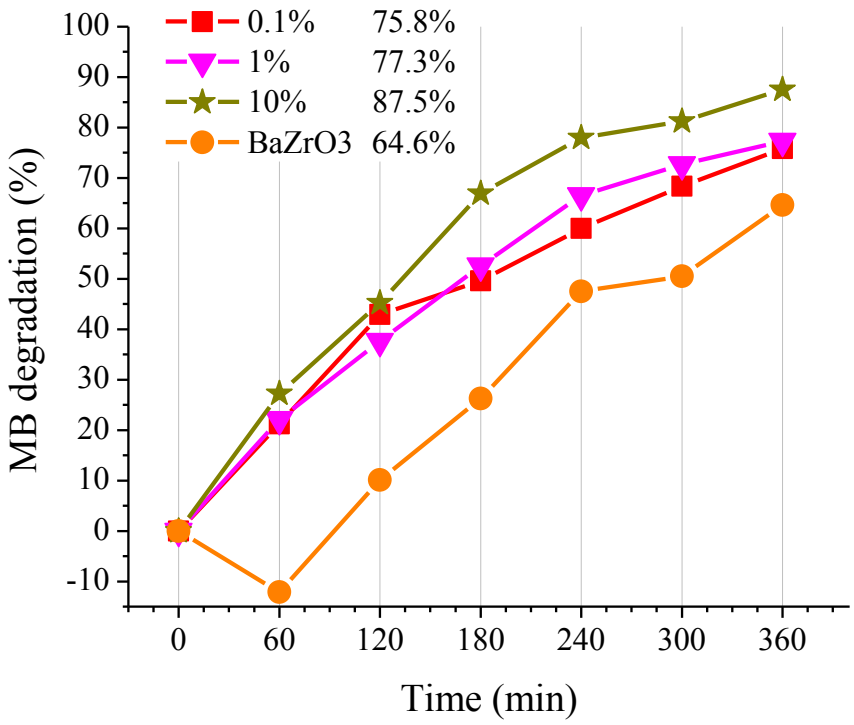

Fig. 42 Methylene blue degradation by $Ba(Zr)_{1-x}Bi_xO_3$ (x= 0, 0.1, 1 and 10) in function of time under natural sunlight irradiation (outdoors).

Conclusions to section 3.1

Nanocrystalline $Ba(Zr)_{1-x}Bi_xO_3$ (x = 0.01, 0.1 0.5, 1, 5 and 10 mol%) solid solutions were synthesized via hydrothermal method and annealing at a 1000 ˚C. Optical and spectroscopic characterization revealed how bismuth ions are substituted into the $BaZrO_3$ structure and change its native properties. After XRD analysis it was found the produced compounds preserved the typical perovskite cubic phase of pure $BaZrO_3$ and primitive cell parameter a in the order of 4.19 Å, for bismuth concentration as high as 10 mol%. Intrinsic differences between Zr^{4+} and Bi^{3+} ions as electronic charge difference and ionic radii difference were found to be the origin of induced changes in the native properties of $BaZrO_3$. With the increment of bismuth content into the $BaZrO_3$ structure, the cell parameter grew along with the crystallite size of $BaZrO_3$ cubic phase and ZrO_2 monoclinic phase segregation, due to bismuth ions substitution into the octahedral zirconium sites, bonding with oxygen atoms in the structure. The bigger ionic radius of bismuth ions promoted structural defects inducing oxygen vacancies after Zr-O broken bonds in the long range, and charge difference in the site. Introduction of bismuth ions favored the absorption capabilities of $BaZrO_3$ in the visible range of the electromagnetic spectrum. The UV absorption edge of pure $BaZrO_3$ shifted towards the visible range after bismuth substitution, adding the property for $BaZrO_3$ to absorb visible light, feature absent in the pure $BaZrO_3$.

Reduction of the band gap energy of the samples was related also to the induced disorder in the perovskite. Narrowing of the band gap is also due to additional 6*s* and 6*p* disperse orbitals of bismuth ions. Because of the disperse nature of bismuth orbitals, and charge transfer between bismuth and oxygen atoms, intrinsic photoluminescence of $BaZrO_3$ was improved when low concentrations of bismuth were used, and the samples were excited in the new excitation site at 300 nm. However, concentration quenching diminished and finally killed photoluminescence emissions as bismuth concentration was increased up to 10 mol%. These same properties aided the well performance of bismuth doped $BaZrO_3$ as a photocatalyst. The photocatalytic properties of $BaZrO_3$ were proven through an economic and easily implemented homemade reactor, for degradation of a methylene blue solution under UV light irradiation, to evaluate the photocatalytic activity of $BaZrO_3$ under UV light, and under direct natural sunlight when the photocatalytic activity was evaluated under visible light irradiation. In the case of UV light activation of the photocatalyst, the sample with the best photocatalytic activity was the one with 1 mol% Bi concentration, the best performance of this sample has been related to its small crystallite size and large surface area. In regard to visible light activation of the photocatalyst, the best photocatalytic activity was that of the 10 mol% Bi sample. Enhancement of the absorption spectral properties of $BaZrO_3$ into the visible region, turned out to be critical for the development of $BaZrO_3$ as a visible light-active photocatalyst.

3.2 Photocatalytic response of rare earth single dope $BaZrO_3$ to UV light.

In the present section the photocatalytic activity of two different sets of RE doped $BaZrO_3$ samples is presented. The first set was characterized on its structural and photoluminescent properties in *Chapter 2*, whereas the second set of samples were synthesized in a Teflon autoclaving bottle and only their photocatalytic response were characterized. The first set of samples was tested by degrading a methylene blue - water solution under UV light following the same procedure exposed in *section 3.1.4*. The second set was tested by degrading a Rhodamine B solution in a commercial UV reactor.

3.2.1 Photocatalytic characterization of $BaZrO_3$: RE under UV-light

In the homemade reactor under 366 nm excitation the photocatalytic properties of $BaZrO_3$: RE (RE = Ce^{3+}, Eu^{3+}, Dy^{3+} and Er^{3+}) samples were tested (**Fig. 33**). These already characterized compounds, *see chapter 2*, are crystalline nanophosphors with average size around 42 nm and quasi cubic morphology. The photoluminescence properties of RE dope $BaZrO_3$ are sustained by energy transfer from the host emission to the doped ion, and subsequent emission of the rare earth ion having composed emission spectra that superpose host and RE emissions. Intense PL emission suppose a considerable generation of electron – hole pairs, which are necessary for the photocatalytic processes. Taking this into account, the photocatalytic properties of $BaZrO_3$: RE samples were also evaluated. Shown in **Fig. 43** is the photocatalytic performance of $BaZrO_3$: RE samples. After 120 min of stirring the colored solutions with the compounds powders in dark conditions, MB was adsorbed on the compounds surface on different amounts without a discernible trend other than Dy^{3+} and Eu^{3+} doped samples with bigger crystallite size than Ce^{3+} and Er^{3+} adsorbed MB stronger. However this in not considered a definite fact since it is in contradiction with relationship of crystallite size and crystal surface area. After the UV lamps were switch on and the solutions remained under irradiation and constant stirring for 7 hours, and $BaZrO_3$: Er^{3+} samples showed no photocatalytic activity, since after the dark time these samples adsorbed 5% of MB and after 7 h irradiation, degradation of MB reach only 6% respectively. In regard of $BaZrO_3$:Eu^{3+}, $BaZrO_3$: Ce^{3+} and $BaZrO_3$: Dy^{3+} samples, a little improvement on the photocatalytic activity is perceived, since MB degradation, after 7 hours, augments from19% to 26%, from 9% to 18% and from 19% to 27%, respectively, beyond the experimental error (4%). Nevertheless, further work is necessary in order to thoroughly characterized and test the photocatalytic activity of RE doped $BaZrO_3$.

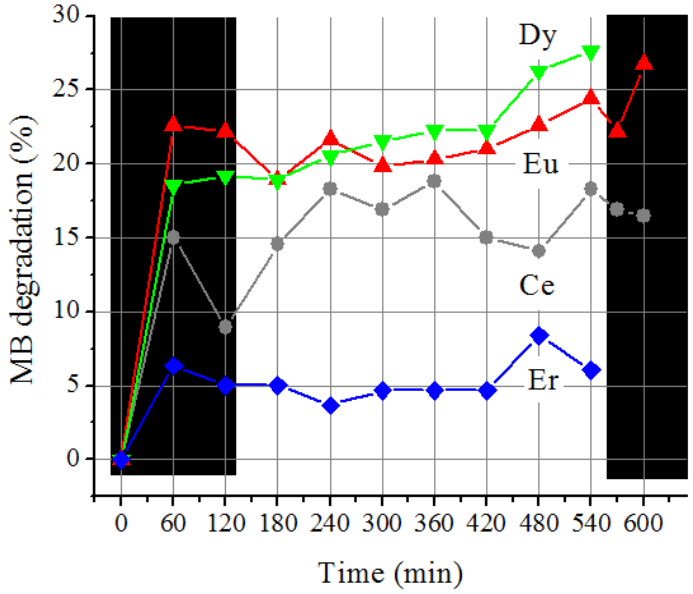

Fig. 43 Photoactivity of $BaZrO_3$: RE samples under UV light irradiation for 7 hours in the homemade reactor.

3.2.2 Photocatalytic activity of Teflon synthesized $BaZrO_3$: RE samples.

A new set of RE doped $BaZrO_3$ samples were synthesized in a Teflon autoclaving bottle and their photocatalytic activities were tested. The only difference between these samples and the characterized in the previous section is the autoclave. The reason to change the glass autoclave for a Teflon autoclaving bottle was to avoid the intrusion of silicon atoms into the $BaZrO_3$ structure. During the research process it was pointed out that when the glass autoclaves are under temperatures higher than 100˚C, and there is sodium compounds present (NaOH in our case) an exchange of silicon and sodium atoms happens due to glass corrosion [22]. According to the manufacturer, the glass autoclave composition is: 81% SiO_2, 13% B_2O_3, 4% $Na_2O + K_2O$, 2% Al_2O_3. The attack suffered on the glass autoclave surface at a temperature of 100 ˚C, is approximately 1.3 μm every hour. According to this information, an estimation of the silicon introduced from the glass autoclave to the compounds during the hydrothermal synthesis was computed. It was found that approximately 44.3 mmol of silicon (~1.2 g) could be introduced into the solution during the hydrothermal synthesis of the RE and bismuth doped $BaZrO_3$ samples characterized on the previous sections.

Initial research to establish the influence of silicon on the properties of the samples is here presented, however, a thoroughly study ought to be done in the future on this regard. On a different approach, rhodamine B (RB) was degraded by the silicon-free samples made in the Teflon autoclave. The characterization of the photocatalytic activity was first evaluated for the pure $BaZrO_3$ sample under visible, and UV light (365 and 254 nm) irradiation. As it is shown in **Fig. 44**, the photocatalytic response of pure $BaZrO_3$ (silicon-free) is almost null under visible light as well as under 365 nm irradiation, resembling the response of the $BaZrO_3$ sample synthesized in the glass autoclave. Variations of RB concentration after being irradiated by visible and 365 mn light for 180 and 100 min respectively were under 2% in both cases. In the present case, pure $BaZrO_3$ had a better photocatalytic response to light of much higher energy, 254 nm, which correspond to energy of 4.89 eV. Such energy corresponds well with the excitation site of $BaZrO_3$ (**Fig. 12 a)**). It is reasonable to expect for samples with wide band gap a better response to higher energy light. To this point it is of particular interest to note that the possible inclusion of silicon atoms to the $BaZrO_3$ structure do not detriment the crystalline structure neither the electron configuration of the compounds, contrary to this, silicon atoms inclusion seems to be favorable to the compounds properties, specially their PL emission properties (**Fig. 12**). As for the photocatalytic property of the silicon-free RE doped $BaZrO_3$ samples, it was tested under UV light of 254 nm and the results are shown in **Fig. 44 b)**. A clear tendency of RB degradation by all of the samples was observed due to a better response to the excitation light. Degradation of RB as a function of light irradiation time was consistent and no recovering of the RB concentration could be detected (experimental error). However, after 6 h of photocatalytic reaction most of the samples degraded RB up to 20%, except for the Dy^{3+} doped $BaZrO_3$ sample which had a better performance degrading up to 25%.

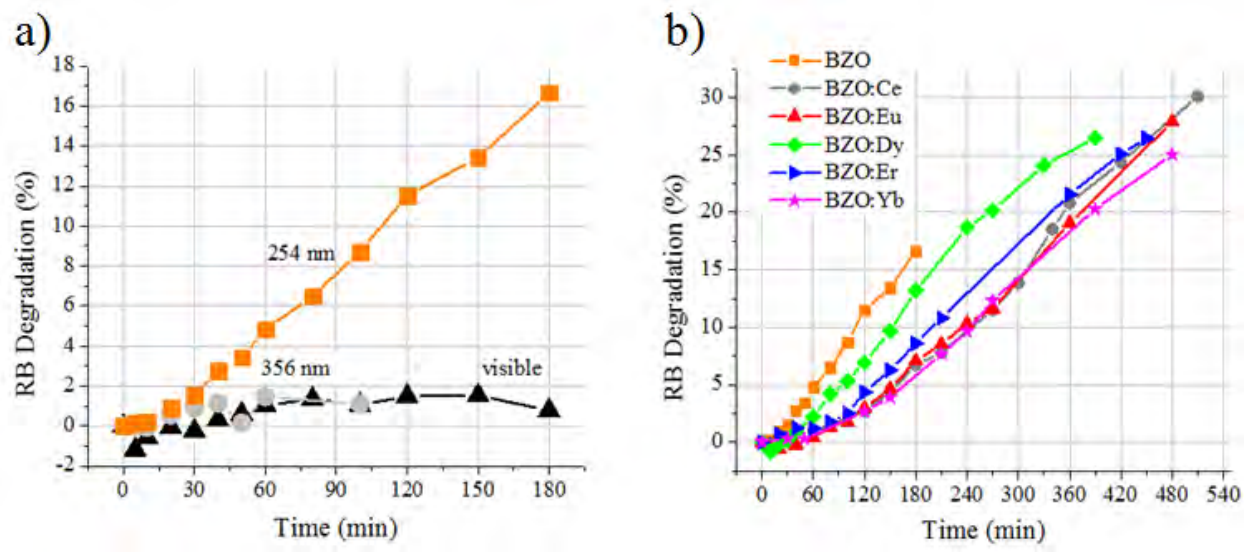

Fig. 44 Rhodamine B degradation performed by: a) Pure $BaZrO_3$ sample under light irradiation (visible, 365 and 254 nm) for 3 h and b) RE doped $BaZrO_3$ samples under 254 nm irradiation.

Even though the well performance of these samples, no clear advantage of one RE doped compound over another was observed. In fact, degradation of RB by the pure $BaZrO_3$ sample was higher than those of RE doped samples after 180 min. Out of these initial results it could be said that degradation of RB is apparently being done mostly by the host, $BaZrO_3$, due to its intrinsic properties. However, it remains to be proven if the highly energetic light of 255nm is involve on the Rhodamine B degradation.

Conclusions to section 3.2.

Initial studies of the photocatalytic activity of RE doped $BaZrO_3$ samples showed a weak reaction to degrade MB solution. The photocatalytic reaction was performed for two different sets of RE doped samples. One set of compounds were synthesized in a glass autoclave. Silicon atoms intrusion into the compounds structure could be expected, due to glass corrosion. After comparing the results of the photocatalytic activity of Bi^{3+} doped $BaZrO_3$ samples characterized in the previous section, with the results obtained after the RE doped $BaZrO_3$ samples, it can be said that the strong adsorption of MB by $BaZrO_3$ compounds stops when the excitation source is turn on, and the photocatalytic activity starts although it turned out to be very weak if not null in the case of the RE doped $BaZrO_3$ samples. In regard of the second set, the silicon-free RE doped $BaZrO_3$ samples, the results obtained showed the photocatalytic activity of $BaZrO_3$ compounds upon rhodamine B degradation under UV light, is mainly due to $BaZrO_3$ intrinsic properties. In both sets, the photocatalytic activity of Dy^{3+} doped $BaZrO_3$ was a little better than for the rest of the RE doped $BaZrO_3$ compounds. This sample had a reaction strong enough to degrade MB

solution beyond the experimental error. Hence, by doping $BaZrO_3$ with Dy^{3+} ions it is possible to achieve some improvement of the intrinsic properties of pure $BaZrO_3$.

References

1. On the development of high density barium metazirconate (BaZrO3) ceramics. Abdul-Majeed, Azad, Selvarajan, Subramaniam and Teng Wang, Dung. 2002, Journal of Alloys and Compounds, Vol. 334, pp. 118-130.
2. Nanocrystalline tetragonal zirconium oxide stabilization at low temperatures by using rare earth ions: Sm3+ and Tb3+. Cordova-Martinez, W., et al. 2002, Optical Materials, Vol. 20, pp. 263-271.
3. Rodriguez-Carvajal. 1993, Physica B: Condens. Matter, Vol. 192, pp. 55-69.
4. Formation mechanism of hydrous-zirconia particles produced by hydrolysis of ZrOCl2 solutions: II. Matsui, Koji and Ohgai, Michiharu. 6, 2000, J. Am. Ceram. Soc, Vol. 83, pp. 1386-1392.
5. A New Blue, Green and Red Upconversion Emission Nanophosphor: BaZrOEr,Yb. Diaz-Torres, L.A., et al. 2008, J. Nanosci. Nanotechnol., Vol. 8, pp. 6425-6430.
6. Polymerizable complex synthesis of BaZr-SnO3 photocatalysts:. Yuan, Yupeng, et al. 2010, J. Matter. Chem, Vol. 20, pp. 6772-6779.
7. Intense violet-blue photoluminescence in BaZrO3 powders A theoretical and experimental investigation of structural order-disorder. Cavalcante, L.S., et al. 2008, Optics Comunications, Vol. 281, pp. 3715-3720.
8. Synthesis and photocatalytic characterization of a new photocatalyst BaZrO3. Yuan, Yupeng, et al. 2008, Int. Hydrogen Energy, Vol. 33, pp. 5491-5946.
9. Improved structural stability of titanium doped Bi2O3 during visible hight activated photocatalityc processes. Wang, Yan, Wen, Yanyuan and Ding, Hanming. 2010, J. Mater. Sci., Vol. 45, pp. 1385-1392.
10. Hybrid precursors synthesis and optical properties of LnNbO4Bi3+ blue phosphors and Bi3+ sensitizing of on Dy3+'s luminescence in YNbO4 matrix. Xiao, Xiuzhen and Yan, Bing. 2006, J. Alloys Compd., Vol. 421, pp. 252-257.
11.Photoluminescence-property-of-Ba-(Zr0.25-Ti0.75)-O3-powders-prepared-by-solid-state-reaction-and-polymeric-precursor-method. Rout, S.K., et al. 2009, Physica B, Vol. 404, pp. 3341-3347.
12. Synthesis of Fine Micro-sized BaZrO3 Powders Based on a Decaoctahedron Shape. Moreira, Mario L., et al. 2, 2009, Crystal Growth & Design, Vol. 9, pp. 833-839.
13. Removal of microorganisms and their chemical metabolites from water using semiconductor photocatalysis. Peter K.J. Robertson et al., 2011, J. Hazard. Mat. doi: 10.1016/j.jhazmat.2011.11.058.
14. Photocatalytic degradation of organic dyes by a high efficient TiO2 based catalysts under solar light irradiation. Jun Wang et al., 2009, Catal. Lett., Vol.130, pp. 551-557.
15.Removal of methylene blue dye from textile simulated sample using tubular reactor and TiO2/UV-C photocatalytic process. M.H. Ehrampoush et al.,2011, Iran. J. Environ. Health. Sci. Eng.,Vol 8, pp. 35-40.
16. Studies of photo-induced charge transfer properties of ZnWO4 photocatalyst. Dongqing He et al., 2010, Appl. Surf. Scien., doi: 10.1016/j.apsusc.2010.09.097.
17.ZrW2O8 photocatalyst and its visible-light sensitization via sulfur anion doping for water splitting. Li Jiang et al., 2010, J. Hyd. Ene., doi: 10.1016/j.ijhydene.2009.12.187.
18. Comparison of zinc oxide nanoparticles and its nano crystalline particles on the photocatalytic degradation of methylen blue. Joon Jang, Young, Simer, Cynthia and Ohm, Taein. 2006, Mater. Res. Bull., Vol. 41, pp. 67-77.
19. Photocatalysis A to Z What we know and what we do not know in a scientic sense. B. Ohtani. 2010, J. Photochem. Photobio. C., Vol 11, pp. 157-178.
20. Decontamination and disinfection of water by solar photocatalysis: Recent overview and trends. S. Malato et al., 2009, Catalysis Today, Vol 147, pp. 1-59.
21. Efficient Photocatalysis on BaBiO3 Driven by Visible Light. Tang, Junwang, Zou, Zhigang and Ye, Jinhua. 2007, J. Phys. Chem. C, Vol. 111, pp. 12779-12785.
22. (R), Duran Group. Duran Group. Chemical properties of Duran. [Online] [Cited: 1 21, 2012.] http://www.duran-group.com/en/about-duran/duran-properties/chemical-properties.html.

Chapter 4

Summary

The present thesis report contributed on the study and characterization of the perovskite $BaZrO_3$. The study of this particular material is of relevant importance in diverse applied fields. It is a potential candidate to be used in many technologies of recent development such as: water splitting, light-active catalysis, luminescent devices, and it is already used in the production of crucibles for the synthesis of superconductor materials. The main reason to study the properties of $BaZrO_3$, either when it is pure or doped, is to gain insights over the nature and origin of its properties which will lead to develop new applications. Part of the present work started after the recent breakthrough done by Yupeng Yuan *et al* on achieving successful water cleavage using pure $BaZrO_3$ as a UV-active photocatalyst. Along with this, the increasing worldwide necessity of a more efficient use of natural resources has set the trend to research for new materials, or new applications for well known materials, which provide a more efficient use of energy and natural resources. The first proposal of the present work is to study how the intrinsic photoluminescent property of pure $BaZrO_3$ is affected by the substitution of different rare earth elements found in the lanthanide family. Through this, an improvement on the blue-green emission of $BaZrO_3$ is seek. It is also desirable to study the possibility of making of $BaZrO_3$ an option to be used as a blue-light phosphor. The second proposal is to give $BaZrO_3$ visible-light-active photocatalytic properties after doping it with bismuth ions. Such compound could be use in catalytic processes using visible daylight as the activating source.

Analytical grade raw materials were used as received to synthesize the samples of undoped and doped $BaZrO_3$ via the hydrothermal methodology. Doped in different mol concentrations $BaZrO_3$: RE (RE = Ce^{3+}, Eu^{3+}, Dy^{3+}, Er^{3+}, Yb^{3+}), $BaZrO_3$:Yb^{3+}-Tm^{3+}, $BaZrO_3$:Bi^{3+} were used on the conducted studies of the intrinsic emission, blue-light generation and photocatalytic activity of doped $BaZrO_3$ respectively. Induced changes to the crystalline structure, morphology, composition and optical properties of $BaZrO_3$ due to the substitution of the RE or bismuth ions were characterized by X-ray diffraction (XRD), Rietveld adjustment, scanning electron microscopy (SEM), energy dispersive X-ray spectroscopy (EDXS), optical absorption and fluorescence emissions. Such characterization techniques were necessary to comprehend the origin and nature of these compounds properties.

The broad band intrinsic emission of $BaZrO_3$ has been improved from blue-green emission to a more white emission. As a result of RE doping, the emission spectrum of $BaZrO_3$

has been balanced and the energy redistributed in the visible light range. It was found that the photoluminescent mechanism involves direct excitation of the host at excitation site 267 nm, followed by nonradiative energy transfer process, from the host to the dopant ions. Once excited, the host and the RE ions emit light after electron-hole recombination. Hence the emission spectra of the compound consisted of the superposition of the host intrinsic emission and the emissions from the RE electronic transitions. The final color emission of each compound depend on the substituted RE ion and on the nonradiative energy transfer process efficiency. $BaZrO_3:Ce^{3+}$ and $BaZrO_3:Yb^{3+}$ rendered blue-green light emissions due to energy mismatch between the host emission and the energetic levels of these RE ions. Relative to Ce^{3+} and Yb^{3+} doped samples, $BaZrO_3:Er^{3+}$ color emission was found closer to the white color coordinate according to CIE 1931 chromaticity diagram. The better the nonradiative energy transfer process the better the RE ions emissions contribution. This was the case of $BaZrO_3:Eu^{3+}$ and $BaZrO_3:Dy^{3+}$ samples which rendered red and white light emissions respectively. The final color emission also depends on the excitation wavelength source. These compounds had emissions resulting from either direct excitation of the host or direct excitation of the RE, which renders different color emissions.

Tunable blue-light phosphor based on Yb^{3+}-Tm^{3+} codoped $BaZrO_3$ depended on overall content of dopant inside the host crystalline structure. Upon increasing the content of Tm^{3+} into the compound, the light-color emission change from red to blue and back to red. Near infrared light emitted increased with the RE content increments. It was found that the dominant mechanisms from which the color tuning depended was the cross-relaxation process between thulium ions. The compound visible emission happened after 967 nm excitation resulting from the upconversion process. It was found that NIR light was emitted as a consequence of the cross-relaxation process due to the increment of thulium ions. Hence, these two parameters were critical in order to control the color emission. As thulium content in the compound increases, the electron–hole recombination rate changes due to the availability of unoccupied lower energetic states. When the final electronic state for red emission to happened were occupied, the excited electrons find their way out through cross-relaxation between thulium ions, then the recombination process happed and blue light was emitted along with a more intense NIR light. It was found that for the higher concentration of thulium ions, almost all of the emitted light was NIR light because cross-relaxation turned out to be the dominant process.

Photocatalytic properties of $BaZrO_3$ were enhanced by doping it with bismuth ions and visible-light-active photocatalysis was possible. Bismuth substitution into the $BaZrO_3$ lattice provided this compound the capacity to strongly absorb light deep into the visible-light region up to 600 nm. Incorporation of bismuth ions provided the compound with additional electron orbitals 6*s* and 6*p* which contributed to narrow the band gap. When doped in low bismuth concentrations, the intrinsic photoluminescence of $BaZrO_3$ was improved in intensity and a new

excitation site appeared at 300 nm. However, it required higher bismuth concentrations in order to the compound had a photocatalytic activity. Despites the high content of bismuth in the compounds, the crystalline structure remained cubic, which was a desired property of $BaZrO_3$ compound to preserve. The photocatalytic activity of bismuth doped $BaZrO_3$ was tested by degrading an organic dye in a homemade reactor under UV-light irradiation. Photocatalysis activity under UV irradiation was better for the 1 mol% Bi^{3+} doped sample, mainly due to its smaller size particles and less monoclinic ZrO_2 phase segregated. The visible-light-active photocatalysis was done outdoors under direct natural sunlight. Degradation of the organic dye was performed well by all samples. The better activity of the 10mol% Bi^{3+} doped sample was due to its stronger and broadest absorption of visible light. Degradation of the organic dye colorant was enhanced by 35.5% upon doping $BaZrO_3$ with 10mol% Bi^{3+}. The results showed a consistent photocatalysis activity and degradation of the dye up to 87% was achieved after 6 h of exposition to the sunlight.

During the course of this work, the photocatalytic activity of RE doped $BaZrO_3$ samples was also tested for UV-light-active catalysis. The obtained results were not as conclusive as in the previous studies. Two set of RE doped $BaZrO_3$ samples were synthesized and tested. The main difference on the synthesis process of each set was the use of a glass or a Teflon autoclave. On the hydrothermal synthesis of samples done on the glass autoclave, silicon atoms were exchanged for sodium atoms from the glass into the solution. Hence, a small concentration of silicon atoms, around 44 mmol were mixed with the compound. An initial comparative study between the two sets of RE doped $BaZrO_3$ samples suggested that silicon traces might help only to the photoluminescent properties of these samples. Regarding to their photocatalytic activity under UV-light irradiation, a weak activity was obtain in every case. An erratic behavior on the adsorption-desorption equilibrium process was observed every time, which made difficult to determine if there were a photocatalytic activity or not, beyond the experimental error. In the best case, Dy^{3+} doped $BaZrO_3$ degraded the organic dye by a slight percentage above the rest of the samples. On the other hand, silicon-free samples showed good photocatalytic activity upon degrading organic colorants MB and RB. However, a further and more compelling study ought to be done to establish if there is photocatalytic activity due to RE doped $BaZrO_3$ samples.

Future work

The author of this work and the research group EMANA lead by Professor Diaz-Torres at Centro de Investigaciones en Optica A. C. (CIO), are interested in participate on the existing effort which aims to solve the problem of recover the photocatalyst powder off the treated chemical specimen after the photocatalyst reaction has taken place.

Original work has been done in this direction with positive preliminary results so far. In the first attempts, perovskites $BaBiO_3$ and $BiFeO_3$ were synthesized by different routes, hydrothermal and co-precipitation methodologies respectively. Despites the unsuccessful efforts to obtain single phase crystalline perovskites (see **Fig. 45 a)**), the product obtain via the co-precipitation method did show a strong response to the magnetic field applied by a magnet. This places us in the right path to follow; the synthesized product is a fine powder which finds itself in the nanometer range, see **Fig. 45 b)**. Once suspended in water, the powder moves freely until a magnet is placed and the powder gathers on it due to its well response to the magnetic field at room temperature. Temperature dependent magnetization (**Fig. 46 a)**) and hysteresis measurements (**Fig. 46 b)**) of the BFO-1C sample have been done. Zero-field-cooled and field-cooled have been tested. Zero-field-cooled data show that after cooling the BFO-1C sample at zero-field, magnetic moments are oriented in all random directions. After applying 100 Oe field, moments start to align along the field and with increasing temperature magnetic moments will increase and eventually it merges with field-cooled data. The temperature where these two plots merge, the blocking temperature, is about 35 K. Hysteresis data showed that BFO-1C sample has finite coercive field at 5 K, but very low coercive field at 300 K. Hence, at 300 K, BFO-1C is a superparamagnetic material.

Further work on this compound is needed in order to prove its photocatalytic capability upon degradation of organic dyes and characterization of its chemical stability to be used as an UV or visible light active photocatalyst. It is desirable for this compound to be correctly identified and synthesized as a crystalline single phase perovskite. In regard of $BaBiO_3$ compound, the efforts will continue to accomplish a crystalline single phase perovskite as well.

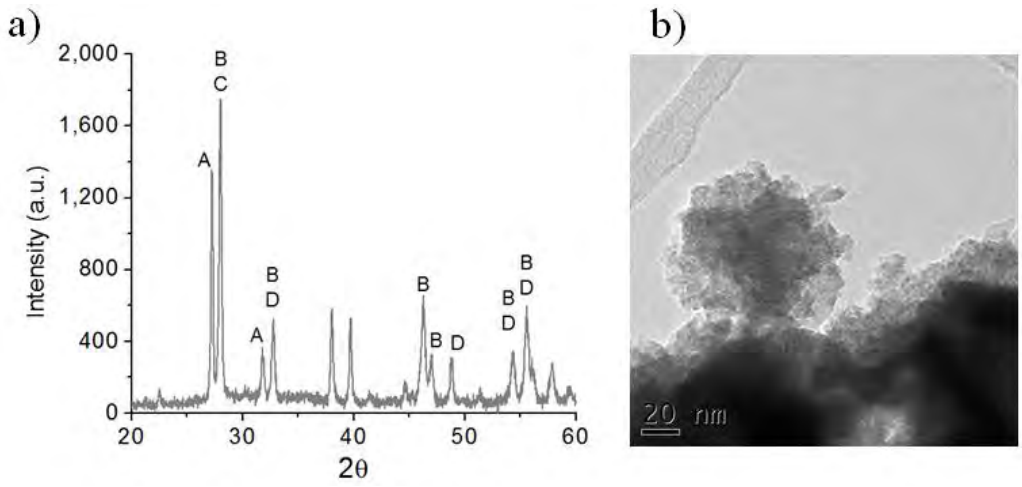

Fig. 45 a) XRD pattern of BFO-1C sample synthesized via co-precipitation process, identified segregated phases correspond to: cubic Bi_2O_3 JCPDS 77-2008 (A), tetragonal Bi_2O_3 JCPDS 78-1793 (B), orthorhombic $Bi_2Fe_4O_9$ JCPDS 74-1098 (C) and cubic $Bi_{25}FeO_{40}$ JCPDS 46-0416 (D). b) SEM image of BFO-1C sample.

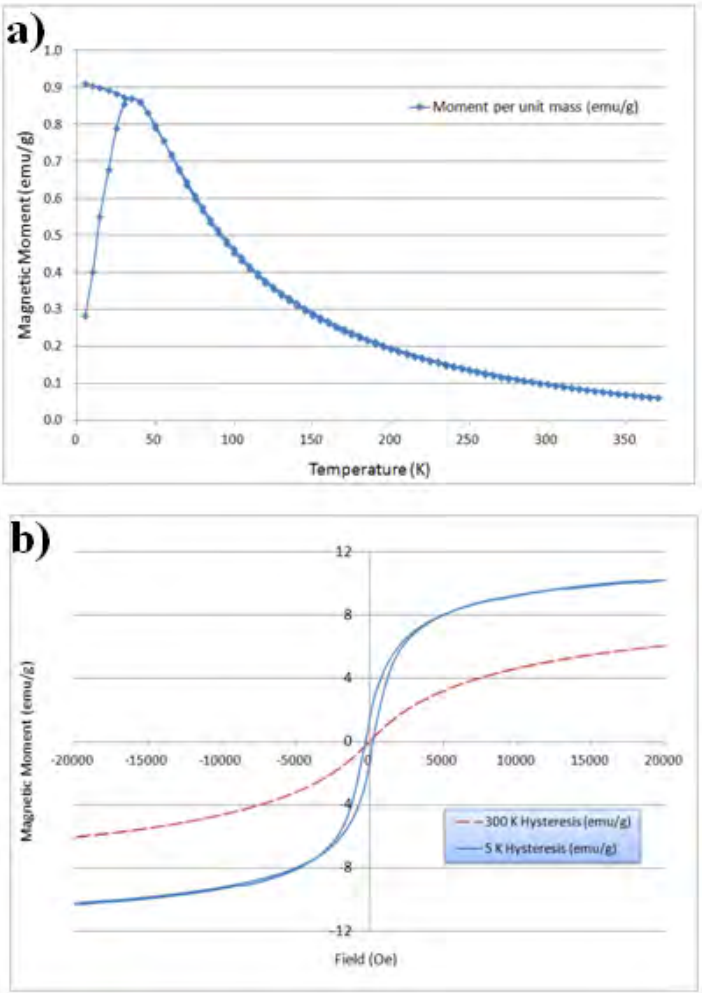

Fig. 46 a) Magnetic moment as a function of temperature with 100 Oe magnetic field applied, b) Magnetic hysteresis at 5 K (solid line) and 300 K (dash line).

Contributions derived from this thesis work.

1) Blue and red emission in wide band gap $BaZrO_3$: Yb^{3+}, Tm^{3+}
   Materials Science and Engineering B 174 (2010) 169-173.
   R. Borja-Urby, L.A. Díaz-Torres, P. Salas, M. Vega-Gonzalez, C. Angeles-Chavez.
   Cited by 4.

2) Strong broad green UV-excited photoluminescence in rare earth (RE = Ce, Eu, Dy, Er, Yb) doped barium zirconate.
   Material Science and Engineering B 176 (2011) 1388-1392.
   R. Borja-Urby, L.A. Díaz-Torres, P. Salas, C. Ángeles-Chávez, O. Meza.
   Cited by 3 (in revision).

3) Structural study, photoluminescence, and photocatalytic activity of semiconducting $BaZrO_3$: Bi nanocrystals.
   Material Science and Engineering B 176 (2011) 1382-1387.
   R. Borja-Urby, L.A. Díaz-Torres, P. Salas, E. Moctezuma, M. Vega, C. Ángeles-Chávez.

Contribution to other works.

1) Structural and photoluminescence study of Er-Yb codoped nanocrystalline ZrO_2-B_2O_3 solid solution.
   Materials Science and Engineering B
   doi: 10.1016/j.mseb.2012.01.009
   P. Salas, R. Borja-Urby, L.A. Diaz-Torres, G. Rodriguez, M. Vega, C. Angeles-Chavez.

This thesis work was supported by the National Council for Science and Technology (CONACyT) through the scholarship grant: 173046 for PhD studies at Centro de Investigaciones en Óptica A.C. (CIO) in the period: September 2009 – May 2012.